Experimental Studies of W-Band Accelerator Structures at High Field

Marc Edward Hill

Stanford Linear Accelerator Center
Stanford University
Stanford, CA 94309

SLAC-Report-560
November 2000

Prepared for the Department of Energy
under contract number DE-AC03-76SF00515

Printed in the United States of America. Available from the National Technical Information Service, U.S. Department of Commerce, 5285 Port Royal Road, Springfield, VA 22161.

Experimental Studies of W-Band Accelerator Structures at High Field

A thesis presented
by

Marc Edward Hill

to
The Department of Physics
in partial fulfillment of the requirements
for the degree of
Doctor of Philosophy
in the subject of

Physics

Harvard University
Cambridge, Massachusetts
November 2000

Thesis advisor | Author
John Huth | Marc Edward Hill

Thesis advisor

John Huth

Author

Marc Edward Hill

Experimental Studies of W-Band Accelerator Structures at High Field

Abstract

A high-gradient electron accelerator is desired for high-energy physics research, where frequency scalings of breakdown and trapping of itinerant beamline particles dictates operation of the accelerator at short wavelengths. The first results of design and test of a high-gradient mm-wave linac with an operating frequency at 91.392 GHz (W-band) are presented. A novel approach to particle acceleration is presented employing a planar, dielectric lined waveguide used for particle acceleration. The traveling wave fields in the planar dielectric accelerator (PDA) are analyzed for an idealized structure, along with a circuit equivalent model used for understanding the structure as a microwave circuit. Along with the W-band accelerator structures, other components designed and tested are high power rf windows, high power attenuators, and a high power squeeze-type phase shifter. The design of the accelerator and its components where eased with the aide of numerical simulations using a finite-difference electromagnetic field solver. Manufacturing considerations of the small, delicate mm-wave components and the steps taken to reach a robust fabrication process are detailed. These devices were characterized under low power using a two-port vector network analyzer to verify tune and match, including measurements of the structures' fields using a bead-pull. The measurements are compared with theory throughout.

Addition studies of the W-band structures were performed under high power utilizing a 11.424 GHz electron linac as a current source. Test results include W-band power levels of 200 kW, corresponding to fields in the PDA of over 20 MV/m, a higher gradient than any collider. Planar accelerator devices naturally have an rf quadrupole component of the accelerating field. Presented for the first time are the measurements of this effect.

Contents

List of Figures

Acknowledgments

Graduate school is an experience that is often tiring, confusing, overwhelming, humbling and at the same time intense, stimulating, enlightening, and empowering. The intellectual and emotional support I received during this time is appreciated and will not be forgotten.

I thank my advisors Profs. John Huth and David Whittum at the Universities of Harvard and Stanford, respectively. John for encouraging me to follow my interests, even when they took me across oceans and continents. David for testing my limits in every respect and always forcing me to follow my intuition with mathematical rigor. David would faithfully expose me to the real world while protecting me from its elements, as any good advisor should. I give sincere gratitude to Prof. Heino Henke at the Technische Universität in Berlin for hosting me in my early development and introducing me to those at Stanford.

The bulk of the thesis work was performed at the Stanford Linear Accelerator Center (SLAC) where the resources I found were crucial and invaluable for the thesis. Tapping the resources of a large institution such as SLAC is a worthwhile, yet sometimes delicate endeavor. More than 1000 man-years of accelerator experience can be a powerful foundation when performing high quality research.

One person who made much of this work possible was my aide-de-camp, Richard Callin. With his vast experience of 38 years at SLAC, Rich taught me many aspects of building a large accelerator including vacuum technology and mechanical engineering. He watched over every aspect of the experiment to guarantee its success. His vivid personality and openness made my time at SLAC fruitful and happy. Rich retired at the same time that I finished writing the thesis; he will be sorely missed at SLAC.

I received support from the National Science Foundation in the form of a Graduate Student Research Fellowship and the Accelerator Research Department B at SLAC supported me and my research under the SLAC Accelerator Graduate Student Program. I thank those from ARDB for their hospitality, including Eric Colby for reading and reviewing the thesis and Angie Seymour for her outstanding administrative support.

On a personal note, I thank my parents for their support throughout this process and my sister, Melissa, for her continued understanding of me. Thanks to Laura for her love and understanding during the final stage of writing the thesis. At last, I bow to the San Francisco crew: Parag, Turi, Ed, Vlatko, Damon, Eric, Mikey, Tim, Noel, Marian, Heather, and Jonathan. To keep me sane, they followed me down muddy cliffs, along dirty streets, and into spooky forests just to catch a glimpse of the moon.

Dedicated to my grandparents
Howard and Georgia Hill
and my departed grandfather
Floyd Chandler

Chapter 1

Introduction

J. J. Thomson's discovery of the electron in 1897 using a cathode ray tube marks the beginning of high energy physics (although the electrons in his study were moving only one-tenth the speed of light). The cathode ray tube was the first "accelerator" though it would be more precisely termed "liberator" for emitting electrons from the cathode's hot surface, giving the first precision measurement of the electron — its charge to mass ratio. A next major step came in 1910 when H. Geiger and E. Marsden performed experiments scattering α-particles off of a gold foil which led to Rutherford's presumption that atoms are mostly void with dense centers. In 1932, in another experiment using polonium as an α-particle source, Chadwick discovered the neutron. Particle physics began to take shape in 1931 when looking at cosmic rays, C. Anderson discovered the positron.

Experimental particle physics is based on the use of three types of sources: radioactive elements, comic rays and particle accelerators. The years following 1931 flourished using these sources and today, with a few notable exceptions, high energy physics relies exclusively on particle accelerators. High energy physics requires a high-energy accelerator and the trend toward the exponential growth of the size of these machines is prohibitive. Looking forward, the Large Hadron Collider at CERN is the one machine being built that will push the energy frontier beyond the 2 TeV proton machine at Fermi Lab. There are studies looking at future machines for electrons such as the Next Linear Collider (NLC) and the Compact Linear Collider (CLIC). Both electron machines hope to reach the TeV-scale, but their size of tens of kilometers and subsequent cost is daunting. The NLC has another problem of note. The NLC hopes to run at a gradient of 100 MV/m, however, up to the time of writing, the collaboration has not been able to sustain field levels of more than

70 MV/m without damage [1].

A compact machine for reaching the TeV-scale and beyond requires high electric field gradient and hence a new type of accelerator. Breakdown, trapping and pulsed heating dictate that such a high field requires a high-frequency structure. Looking for a practical program of research in this area, we first investigated scaling laws for RF accelerators by R. Palmer and his discussions of open structures for use in laser acceleration of particles [2]. This reading sparked an interest in using very small closed RF cavities at laser wavelength scales. We considered the use of planar substrates to fashion laser-driven accelerator structures. This interest in planar devices led to the work of H. Henke at the Technische Universität in Berlin on planar rf cavities at 100 GHz. At the same time, the Accelerator Research Division B (ARDB) had formed at the Stanford Linear Accelerator Center (SLAC) and was pursuing the design of a high-gradient linac at 91.392 GHz (W-band). Discussions with Henke and with SLAC led to the impetus of this work, the design, fabrication and test of components needed for a charged particle accelerator at W-band.

In this work we report development and test of components necessary for building a high-gradient linear accelerator. These components include vacuum and high-power compatible flanged waveguide (WR10), alumina ceramic windows [3], squeeze-type phase-shifters [4], a single cell accelerator structure [5] and a W-band accelerator, based on a traveling-wave planar dielectric structure [6].

Previous attempts have been made to fashion reliable and robust multi-cell traveling-wave structures at mm-wave frequencies [7]; however these have proved difficult to assemble accurately, prone to failure of thin coupling irises, and difficult to bond at current-carrying joints [8]. In the meantime we have chosen to pursue an alternate approach to fashion a structure amenable to high-gradient acceleration employing dielectric loaded waveguide in a slab geometry.

D. Palmer reported problems in manufacture of 91 GHz coupled cavity structures [9]. Significant damage to the coupling irises during diffusion bonding as well as poorly bonded joints, were two problems of note. N. Kroll suggested the “zipper” structure as an alternative to the more conventional design that does not require diffusion bonding. E. Lin suggested the planar dielectric accelerator (PDA) structure, made from a featureless dielectric strip brazed to copper, as another alternative that does not require the many small features of the disk loaded structure. The “zipper” and PDA structures were designed and manufactured in parallel, where we present results for the PDA in this thesis.

We successfully designed, fabricated, and characterized 91 GHz devices using EM simulations, circuit equivalent models, electro-discharge machining (EDM), and a home built W-band vector network analyzer (VNA). Successful tests under low power conditions led us to study these structures under high fields. High power W-band sources are also being studied in parallel; however rather than wait for the development of these devices, we opted to utilize an X-band bunched electron beam to power the W-band structures.

There is a history of beam-powered accelerator devices, starting with J. Rosenzweig's observations of plasma wake-field acceleration at Argonne National Lab (ANL) [10]. J. Wang studied wake-fields in X-band structures at ANL [11], followed by Westenskow, *et al.* , powering a relativistic klystron at X-band with an induction linac [12]. C. Adolphsen made further studies of wake-fields in X-band structures at the ASSET facility at SLAC [13]. S. Lidia continued relativistic klystron studies at CESTA in France [14]. Here we present W-band studies of accelerator structures sub-harmonically driven by the NLCTA; the first work of its kind at 91.392 GHz [15].

The organization of this thesis is as follows. In Ch. 2 we introduce the concepts of RF acceleration and limitations of currently proposed accelerators. These limitations motivate this work at W-band and the development of novel structures. Ch. 3 presents the theory of the planar dielectric accelerator including a circuit analysis useful for understanding the results of bench measurements described in Ch. 4 where we design and cold test devices necessary for a W-band linac. The work includes W-band accelerator structures and high power components including attenuators, an rf window and phase shifter. In Ch. 5, we go on to describe the facility developed for test of these components at the NLCTA and the results of these tests. In Ch. 6, we provide conclusions from this work and propose experiments for future development of W-band and higher frequency accelerators.

Chapter 2

RF Linacs

In this chapter we introduce ideas and concepts for accelerators and give the motivation for W-band. We also introduce the NLCTA and its beam diagnostics.

The design of the RF linac is virtually unchanged since its development in the years 1947 to 1955. Alternatives to RF linacs such as circular machines (SPEAR, LEP, CESR) have produced a wealth of physics and particle discoveries. Linear machines have generally lagged in technology and in making measurements in the energy frontier, however this will change because of the limit of circular machines by synchrotron radiation. For this reason, fixed target experiments at linear machines have been used mostly for precision measurements. One notable exception is the work of R.Taylor, *et al.* , finding the first evidence of sub-structure of the proton, now known as quarks. When considering a linear collider, the rates of e^+e^- reactions is equal to the luminosity times the cross-section. The cross-section scales inversely with the square of the center of mass energy, assuming the absence of any particle production resonances. This fact, drives the requirement for a high energy machine, say in the TeV range, to provide very high luminosity in the range of 10^{33} to 10^{34} $\text{cm}^{-2}\text{s}^{-1}$.

Reaching luminosity of this scale requires very small bunch sizes and high charge per bunch. Achieving these small bunch sizes requires a very low emittance beam. Low emittance and high charge are typically competing characteristics because high bunch charge creates correspondingly large wake fields that in turn increase bunch emittance.

2.1 Principles of RF acceleration

Acceleration of charged particles is accomplished by subjecting these particles to electric and magnetic fields. The force felt by a particle is

$$\vec{F} = q(\vec{E} + \vec{v} \times \vec{B}), \tag{2.1}$$

known as the Lorentz force. The cathode ray tube (CRT) was the first accelerator; a form of which is in nearly every home. In the CRT, a static electric potential accelerates electrons from the cathode to the anode. Electric plates and magnetic coils along the vacuum tube control the direction of the electrons. DC electric fields can be used for acceleration, however they are limited to a potential of a few MV.

When a particle is accelerated its velocity, $\vec{\mathrm{v}}$, increases, but more importantly its inertia increases according to the relativistic formula

$$E = \gamma m c^2 \tag{2.2}$$

$$\gamma = \left(1 - \frac{\vec{\mathrm{v}}^2}{c^2}\right)^{-1/2} \tag{2.3}$$

where m is the particle's rest energy and c the speed of light in a vacuum.

The kinetic energy of a particle is then the total energy minus the rest mass

$$\varepsilon = mc^2\left(\gamma - 1\right) = \left(m^2 c^4 + c^2 \vec{p}^2\right)^{1/2} - mc^2. \tag{2.4}$$

where $\vec{p}$ is the particle's momentum. Looking at Eq. (2.1) and

$$\frac{d\vec{p}}{dt} = \vec{F} \tag{2.5}$$

we see that a particle's kinetic energy cannot be increased by a magnetic field, only by an electric field. When considering deflection, however, for a highly relativistic particle, a 1 Telsa field is equivalent to a 300 MV/m field making bending magnetics much more effective for beam steering.

The electric and magnetic fields of Eq. (2.1) must obey the following Maxwell's equations

$$\vec{\nabla} \bullet \vec{D} = \rho, \tag{2.6}$$

$$\vec{\nabla} \bullet \vec{B} = 0, \tag{2.7}$$

$$\vec{\nabla} \times \vec{E} = -\frac{\partial \vec{B}}{\partial t}, \tag{2.8}$$

$$\vec{\nabla} \times \vec{H} = \frac{\partial \vec{D}}{\partial t} + \vec{J}. \tag{2.9}$$

A particle is accelerated along a trajectory according to

$$\frac{d\varepsilon}{dt} = q\vec{v} \bullet \vec{E}, \tag{2.10}$$

where to get past the MV limit, one could use time varying electric fields, or microwaves. Two important characteristics for a linear accelerator is that the electric field is parallel to the particle's motion and in time with the particle to give a net acceleration

$$\Delta\varepsilon = \int ds\ E_{||}\ \cos\left(\omega t - ks\right). \tag{2.11}$$

where we define $\psi \equiv \omega t - ks$ and we require the condition

$$\frac{d\psi}{ds} = \frac{\omega}{|\vec{v}|} - k > 0. \tag{2.12}$$

However, in free space $\frac{\omega}{k} = c$ and the particles velocity, $|\vec{v}|$, is less than the speed of light. The consequence is that the propagating wave front moves past the particle continually accelerating and decelerating the particle for $|\Delta\varepsilon = 0$.

There are two solutions to this problem. The first is to shield the electron from the field at times when the wave would decelerate it. The second is to spatially confine electromagnetic fields using conductive or dielectric material and boundaries in a way that slows the phase velocity of the wave to less than the speed of light. Consider the classic example of the pillbox type cavity. There are many resonances inside a pillbox cavity; take the lowest resonance, the fundamental mode. A charge moving through the field contained inside the cavity is timed so that while it is inside the cavity, it will experience an accelerating potential.

The simplest accelerating structure is a single cavity and can be described as an externally coupled RLC circuit

$$\left(\frac{d^2}{dt^2} + \omega_0^2\right) V_c = -\frac{\omega_0}{Q_w}\frac{dV_c}{dt} + \frac{\omega_0}{Q_e}\frac{d}{dt}\left(V_L^+ - V_L^-\right) + \frac{\omega_0}{Q_e}\frac{d}{dt}\left(V_R^+ - V_R^-\right) - 2k_l\frac{dI_b}{dt} \tag{2.13}$$

where V_c is the cavity voltage and V_L^+ and V_R^+ are the voltages coming into the cavity from the left and right side. Similarly, V_L^- and V_R^- are the voltages coming out of the cavity. Analysis of this circuit is a subject of the next chapter.

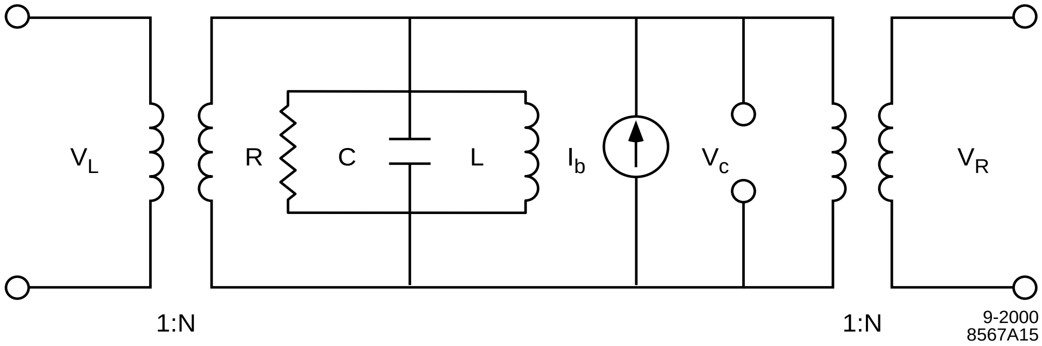

Figure 2.1: An equivalent circuit for a cavity coupled to a beam and to another circuit to the right and left where $V_L = V_L^+ + V_L^-$.

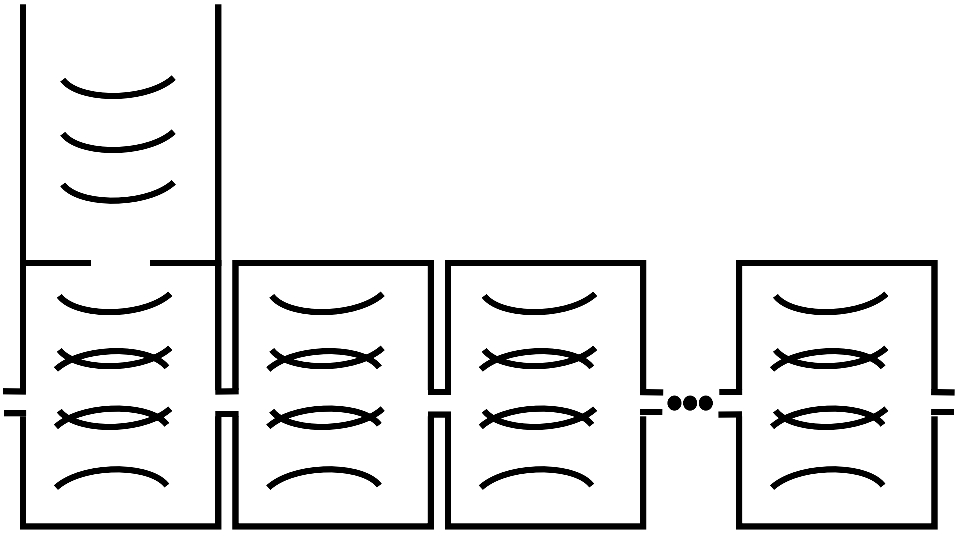

Figure 2.2: A string of cavities are coupled to a waveguide from the top and coupled to each other through the beam passing iris.

One way to picture a more realistic RF accelerator is to imagine a string of these cavities coupled together as in Fig. 2.2. By choosing dimensions properly, this string of coupled oscillators can be made to give continuous acceleration along the particles path.

To accelerate a particle to high energy over a long distance, one must maintain RF phase synchronization with the bunch pulse. Microwave power in free space cannot accelerate particles, in first order, because there is no longitudinal electric field. As shown in Fig. 2.3, microwaves in a smooth waveguide can have a longitudinal electric field, but one must introduce material to reduce the phase velocity to the speed of light. This can be

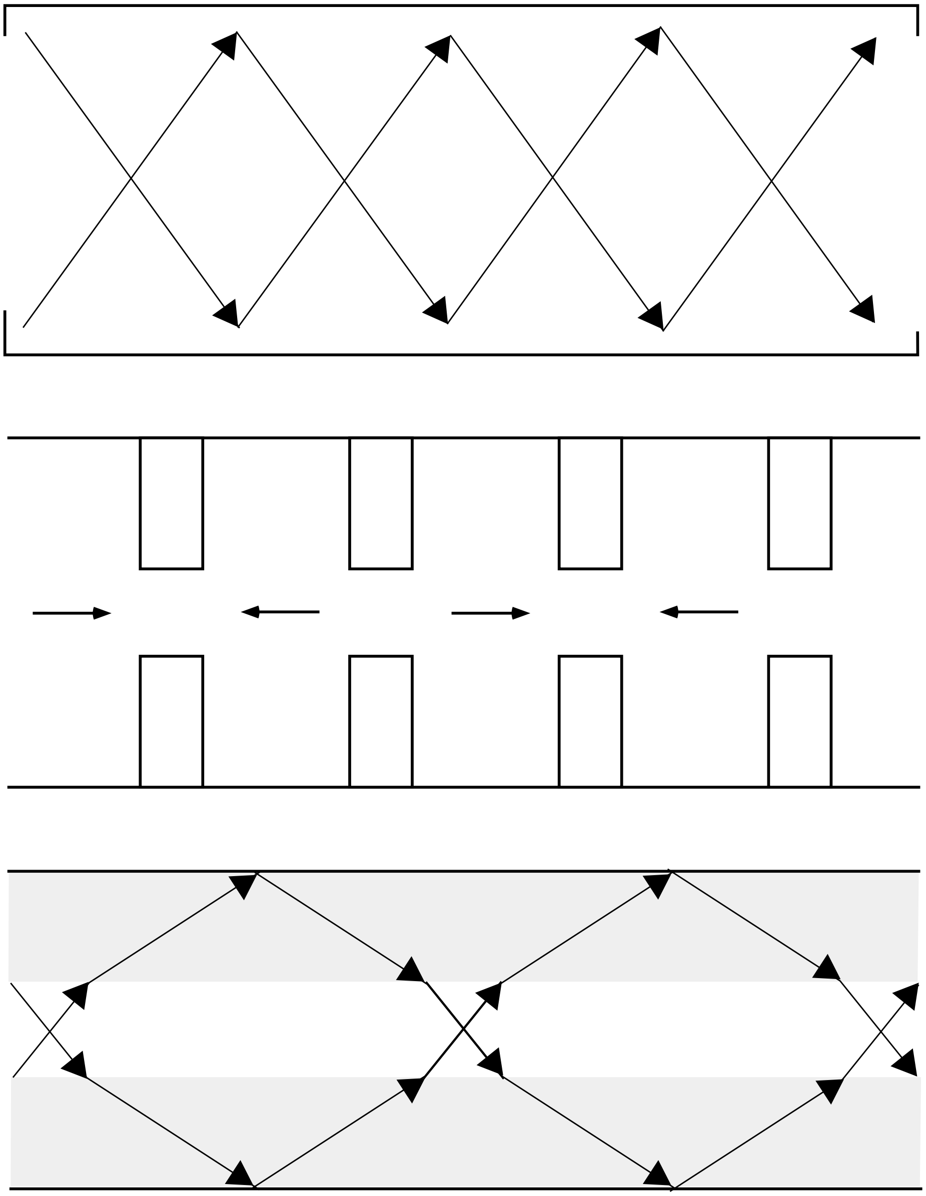

Figure 2.3: Smooth waveguide with phase velocity greater than the speed of light is pictured on top. A disk-loaded waveguide (middle) has irises that impede the wave propagation to slow the phase velocity. The bottom picture is of a dielectric-loaded waveguide where the dielectric slows the wave.

accomplished in many ways. The most common is to periodically add an iris to form what is called a disk loaded waveguide. A more interesting approach is to slow the phase velocity by introducing a dielectric material, to be described in Ch. 3.

2.2 Beam Dynamics

Not only is acceleration of the beam important, but maintaining beam emittance is equally necessary. Keeping the beam near the center of the accelerator structure also helps to reduce wake fields. A well designed linac would have a growth factor < 1, meaning that an offset at the beginning of the linac is not amplified at the end. From this point of view, maintaining control of the beam position through the linac until the IP is highly desirable.

The bunch size through the linac is an important consideration. The beam size in a drift depends on the beam phase space, or emittance, as

$$\sigma_x^2\left(s\right) = \frac{\varepsilon^2}{\sigma_{x'}^2} + \sigma_{x'}^2\left(s - s_*\right)^2$$

where the beam emittance is

$$\varepsilon^2 = \sigma_x^2 \sigma_{x'}^2 - \sigma_{xx'}^2. \tag{2.14}$$

The transverse motion of a particle through a linac can be described by

$$\vec{P}_\perp\left(\vec{r}_\perp, t\right) = \int\limits_{-\infty}^{+\infty} ds \left\{ \frac{1}{V}\vec{E}_\perp + \hat{s} \times \vec{B}_\perp \right\}_{\left(\vec{r}_\perp, s, t + \frac{s}{V}\right)}. \tag{2.15}$$

where we arrive at the Panofsky-Wenzel theorem [16],

$$\frac{\partial \vec{P}_\perp}{\partial t} = -\vec{\nabla}_\perp V_c, \tag{2.16}$$

As shown previously, controlling the transverse motion of the beam is desirable with magnetic fields. The magnetic field through the linac can be describe with a magnetic potential such that

$$\vec{B} = \vec{\nabla}\varphi. \tag{2.17}$$

so giving the momentum change

$$\Delta\vec{p} = -e\hat{s} \times \vec{\nabla}_\perp \psi, \tag{2.18}$$

where

$$\psi\left(\vec{r}_\perp\right) = \int\limits_{-\infty}^{+\infty} ds\ \varphi\left(s, \vec{r}_\perp\right). \tag{2.19}$$

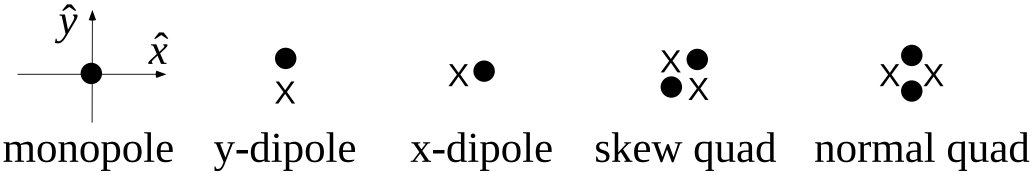

Figure 2.4: Electromagnetic multipoles depicted according to the symmetry of the characteristic voltage witnessed by a relativistic beam, traveling into the page.

and we have that ψ satisfies Laplace's equation in the transverse coordinates

$$\psi\left(\vec{r}_{\perp}\right)=\sum_{m=0}^{\infty} r^{m}\left\{a_{m} \cos (m \phi)+b_{m} \sin (m \phi)\right\}. \tag{2.20}$$

Written in Cartesian coordinates

$$\psi=a_{0}+a_{1} x+b_{1} y+a_{2}(x^{2}-y^{2})+2 b_{2} x y+a_{3}(x^{3}-3 x y^{2})+b_{3}(3 x^{2} y-y^{3})+\ldots \tag{2.21}$$

ψ is described in terms of its n-pole components seen in Fig. 2.4

2.3 Limitations

Particle accelerators have certain properties that ultimately limit the achievable energy gain. Some of these limitations are fundamental, *e.g.* breakdown and trapping, while other limitations are more practical. For example, the accelerators length is limited by real estate and power consumption.

An electron bunch traveling through an unpowered accelerator structure will radiate power into the structure, losing some energy. The beam induced longitudinal wake fields are described with the help of a wake field formalism,

$$\frac{d}{ds} mc^{2}\gamma = e \int_{-\infty}^{\tau} d\tau' W_{||}\left(\tau-\tau'\right) I_{b}\left(\tau'\right), \tag{2.22}$$

that describes the loss of energy and consequent bunch energy spread. The transverse dynamics cause by beam induced magnetic fields is described by

$$\frac{dp_{x}}{ds} = e \int_{-\infty}^{\tau} d\tau'\, W_{x}\left(\tau-\tau'\right) I_{b}\left(\tau'\right) x_{b}\left(\tau'\right). \tag{2.23}$$

Limits on current are therefore given by beam loading and transverse deflection.

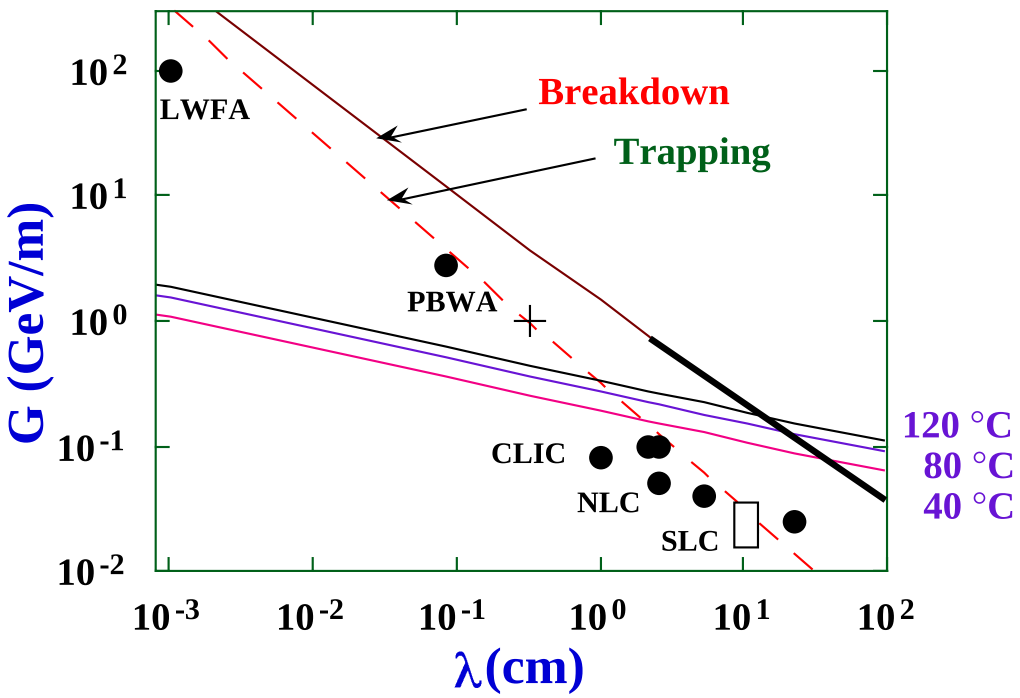

Figure 2.5: Gradient limits determined by scaling laws of breakdown, trapping, and pulsed heating [20].

The SLAC Linear Collider (SLC) was designed for a bunch charge of $5{\times}10^{10}$ e^- and due to wake fields, never reached that goal although with much effort over ten years reached 80% of that value. If it were not for Eq. (2.23), Burt Richter might have fulfilled his promise in December 1984 that "[the] cross section for the production of Z°'s will be so large at the SLC that it will only take a few percent of the design luminosity over a period of a few months to produce ten thousand Z°'s..." [17]. Of course, Burt already knew about wake-fields in the SLC structures and calculated a growth factor of 6, giving restrictions on the alignment tolerances to be less than 100 μm and an injection angle tolerance of less than 1 μrad [18], but did not anticipate the many issues involved with alignment of the structures. Using tedious, time consuming methods, they tried introducing wake-fields in one region to cancel the wakes caused in another region with some success [19].

In addition to the limits on current, there are limitations to the ultimate achievable gradient as seen in Fig. 2.5. At traditional frequencies in the X-band range (labelled in Fig. 2.5 as NLC) and longer wavelength, the limitation on gradient has been from breakdown and trapping. As seen in Fig. 2.5, when moving to shorter wavelengths a new consideration comes into play, called pulsed heating. With pulsed heating the temperature rise on the metal surface during the RF cycle creates cyclic stress on the metal that will eventually lead to fatigue. It is thought that stress created from pulsed heating will lead to micro-cracks in the metal surface that will eventually degrade the Q of the structure. The operating frequency of 91.392 GHz was chosen because it is 2^5 times the SLAC operating frequency and that it is the longest wavelength where we would hope to reach the GV/m gradient regime.

2.4 TESLA (CLIC, NLC), Plasma, Laser, W-Band

The SLAC Two Mile Accelerator (TMA) is the highest energy linac, the flagship of linear colliders; the only ship for that matter. A tremendous effort has produced the TMA and SLC with equally monumental results, *e.g.* substructure of the proton, and as an injector for SPEAR in the 1970's where B. Richter discovered the charm quark and M. Perl the τ lepton. The 1980's promised to be an exciting era, but turned into a desert for research. Fermilab was building the Tevatron and CERN was building LEP. West coast physicists, decided to convert the TMA into the SLAC Linear Collider (SLC) designed to produce the Z_0 particle in copious numbers (we'll be swimming in Z's, was one phrase heard around SLAC in the early 80's) and hoped to scoop their colleagues at CERN as they had done to Ting, *et al.* at Brookhaven. Unfortunately for the SLACers, the aforementioned wakefields, reeked havoc at the SLC preventing them from acquiring the luminosity necessary for interesting studies of the Z_0, until long after CERN had already finished them. The SLC run ended, having produced a million Z_0's and where able to measure the left-right asymmetry parameter A_{LR}. The next step for a linear collider is to reach the TeV energy scale. The problems arising from reaching this goal are formidable, not the smallest problem being funding. Despite the wealth of physics postulated to surface at this level, including the ever elusive Higgs boson, an alphabet soup of supersymmetric particles and possible destruction of the universe, physicists have not put their efforts into creating the next generation of tools for studying the fundamental questions about matter.

The ultimate challenge for a linear collider is luminosity. For two bunches of charge eN_1 and eN_2, with Gaussian charge distributions of rms widths σ_{x_1}, σ_{x_2}, σ_{y_1}, and σ_{y_2} and centroid orbits (x_1, y_1) and (x_2, y_2) the luminosity is

$$L = \frac{N_1 N_2 f_{rep}}{2\pi \Sigma_x \Sigma_y} \exp\left\{ -\frac{(x_1 - x_2)^2}{2\Sigma_x^2} - \frac{(y_1 - y_2)^2}{2\Sigma_y^2} \right\} \tag{2.24}$$

$$\Sigma_x^2 = \sigma_{x1}^2 + \sigma_{x2}^2, \quad \Sigma_y^2 = \sigma_{y1}^2 + \sigma_{y2}^2. \tag{2.25}$$

In the traditional work horse of high energy measurements, circular machines, the bunches are recycled so that the luminosity benefits from a high collision rate. Another problem with small bunches in linear machines is that they have only one opportunity to meet, the bunches are not guaranteed to collide.

There are several "next generation" machines proposed to reach the TeV scale: TESLA, the NLC and CLIC. Each of these machines has its own set of challenges and limitations. Their common limitation is their size because they are very long (20-50 miles) causing decreased tolerance for stablization, failure, and beam offsets.

Plasma accelerators are a promising technology, howeverare still in their infancy having many practical and fundamental limitations. Maintaining synchronism over any significant distance is a key factor limiting their effectiveness. Laser acceleration has yet to be shown over any moderate length; again, the key factor is synchronism. Another problem with laser acceleration schemes is that the stored energy is low meaning that the charge perbunch must be kept low. Low charge decreases the luminosity, but a high repetition rate may recover it.

Accelerators running at a higher microwave frequency in W-band may realize high gradient and high luminosity with an efficient implimentation of the rf power system and maintaining a low bunch energy spread [21]. This work is a first look into this part of the accelerator "phase-space."

2.5 NLCTA as a current source

Let us briefly describe some of the features of the NLCTA that make it suitable for W-band testing. The following discussion also serves to illustrate the particulars of the principles of Secs. 2.1 and 2.2 as well as beamline instrumentation such as BPMs, fast toroids, and profile monitors.

By design, the NLCTA operates with heavy beam loading and must employ beam loading compensation to achieve a low bunch energy spread of $\delta E/E = 0.3\%$. This requires

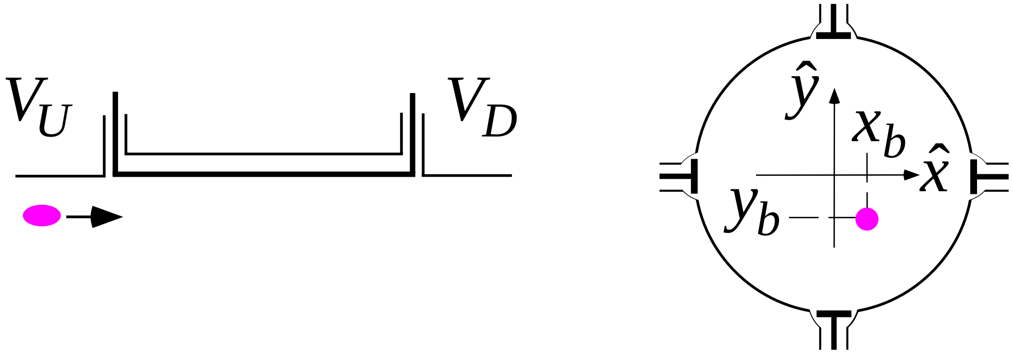

Figure 2.6: A stripline BPM, side-view of one stripline, and assembly endview.

knowledge of the beam current waveform using a fast toroid [22]. A conventional toroid can be describe as an RL circuit,

$$\frac{di}{dt} + \frac{R}{L} i = \frac{1}{N} \frac{dI_b}{dt}, \tag{2.26}$$

where the inductance $L = \mu \, A N^2 / 2\pi \, r$ should be low to achieve the small time constant.

To monitor the beam position, the NLCTA uses striplines as illustrated schematically in Fig. 2.6. BPM operation may be understood in terms of V_U the voltage on the upstream cable, determined by geometry and the wall current, $i(t)$, induced by the beam.

$$V_U\,(t) = \frac{1}{2} Z \left[i\,(t) - i \left(t - \frac{2l}{c} \right) \right], \tag{2.27}$$

where l is the stripline length. The image current depends on the beam position $(\rho \cos\theta, \rho \sin\theta)$ and the stripline position $(r\cos\phi, r\sin\phi)$

$$i = \frac{w}{2\pi \, r} I_b \left[1 + 2 \sum_{n=1}^{\infty} \left(\frac{\rho}{r} \right)^n \cos n(\phi - \theta) \right].$$

The beam dynamics through the linac is described by transfer matrices, σ, for the beam and verified by means of a quad scan. A quad scan is accomplished by measuring the transverse bunch shape on a profile monitor [23] for different quad focal lengths. With knowledge of the magnetic elements in the beamline one can calculate the transfer matrices that describe the particle path through the lattice. Once convinced that one understands the beamline and the beam one may infer the emittance of the beam from the scan.

Stripline diagnostics for single bunches can provide 10 μm-scale position resolution, however the BPM electronics only “see” the beginning 10 ns of the bunch train, therefore they cannot give a time resolved output of the position along a bunch train. For this reason, one can be misled about the position of the bunch train as a whole, particularly when conditions deviate from an ideally compensated beam.

In addition, the NLCTA aperture is a small 0.25 inch diameter and because of this scraping occurs throughout the linac. During preparation of W-band work, in fact we observed 10-15% current loss localized at the end of the chicane. Since the commissioning of the machine in 1995, there had been a mismatch between the beginning and end of the chicane that was blamed on optics. Analysis with the help of a Monte Carlo tracking model showed that this mismatch could be explained by scraping.

Chapter 3

Theory of the PDA

The planar dielectric accelerator structure is based on a dielectric transmission line consisting of two smooth dielectric slabs forming the transmission line as seen in Fig. 3.1. The dimensions are chosen to provide a phase velocity equal to the speed of light and thus synchronism with a relativistic particle beam. The ends of the transmission line are coupled to WR10 waveguide through coupling cavities designed to match to a traveling wave at 91.392 GHz. A great virtue of such a longitudinally invariant structure is that small features such as disks are eliminated. At the same time an adjustable gap ($2a$ in Fig. 3.1) allows for tuning to relax machining tolerances significantly. In addition, the field configuration is such that the surface electric field at the copper is smaller than the on-axis field. In contrast, disk loaded waveguide typically has a surface field *twice* the accelerating gradient. Another virtue is that the side opening affords high vacuum conductance and wakefield damping.

As mentioned previously, a smooth conducting waveguide cannot provide acceleration due to a phase velocity in excess of the speed of light. Addition of a dielectric liner can however slow down the wave and permit synchronous interaction with a charged particle beam. The earliest – and ongoing – studies of such structures concentrated on a cylindrical geometry operating at X-band [24]. At W-band (8× smaller), a cylindrical geometry is difficult to fabricate, and it is for this reason that we have pursued the slab geometry of Fig. 3.1.

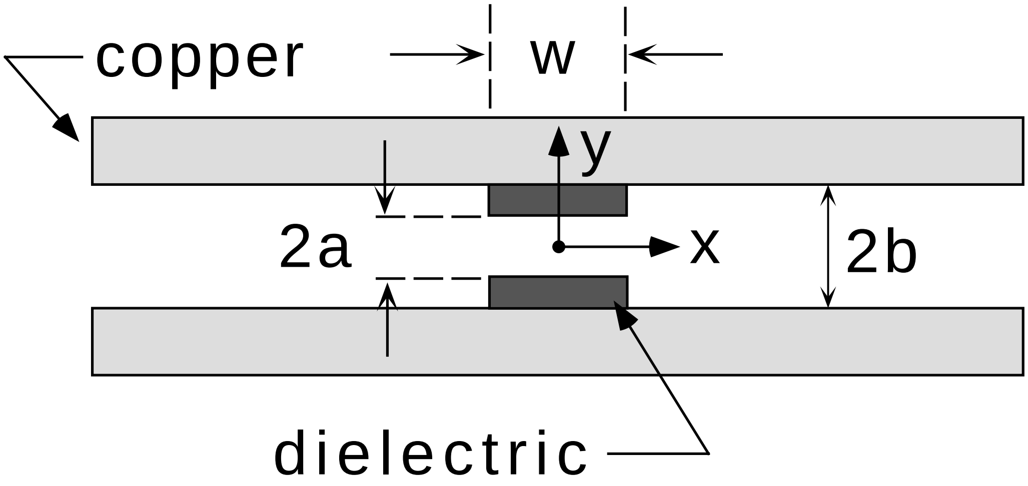

Figure 3.1: A cross-section of the planar dielectric accelerator. The particle beam travels in the z direction, out of the page.

3.1 Fields in the PDA

To illustrate the principles of the planar dielectric accelerator, let us examine the fields in a parallel plate configuration. The plates are lined with dielectric material of relative permittivity ε_r, separated with a vacuum gap of distance $2a$, as seen in Fig. 3.1. For illustration we analyze the fields in the limit $w/b \gg 1$. The solution of the Helmholtz equation for the fields are symmetric in y and for $y > 0$ given by the real parts of

$$E_z = Ge^{ik_z z - i\omega t} \begin{cases} \cos(k_1 y) & y < a \\ \cos(k_1 a)\dfrac{\sin[k_2(b-y)]}{\sin[k_2(b-a)]} & a < y < b \end{cases} \tag{3.1}$$

$$E_y = -ik_z Ge^{ik_z z - i\omega t} \begin{cases} y\ \mathrm{sinc}(k_1 y) & y < a \\ \dfrac{\cos(k_1 a)}{k_2}\dfrac{\cos[k_2(b-y)]}{\sin[k_2(b-a)]} & a < y < b \end{cases} \tag{3.2}$$

$$B_x = i\frac{\omega}{c^2}Ge^{ik_z z - i\omega t} \begin{cases} y\ \mathrm{sinc}(k_1 y) & y < a \\ \varepsilon_r\dfrac{\cos(k_1 a)}{k_2}\dfrac{\cos[k_2(b-y)]}{\sin[k_2(b-a)]} & a < y < b \end{cases} \tag{3.3}$$

where G is the on-axis gradient, k_z is the longitudinal wave number, ω is the angular frequency, and k_1 and k_2 are the transverse wave numbers in the vacuum and dielectric respectively, and satisfy

$$k_1^2 = \frac{\omega^2}{c^2} - k_z^2, \tag{3.4}$$

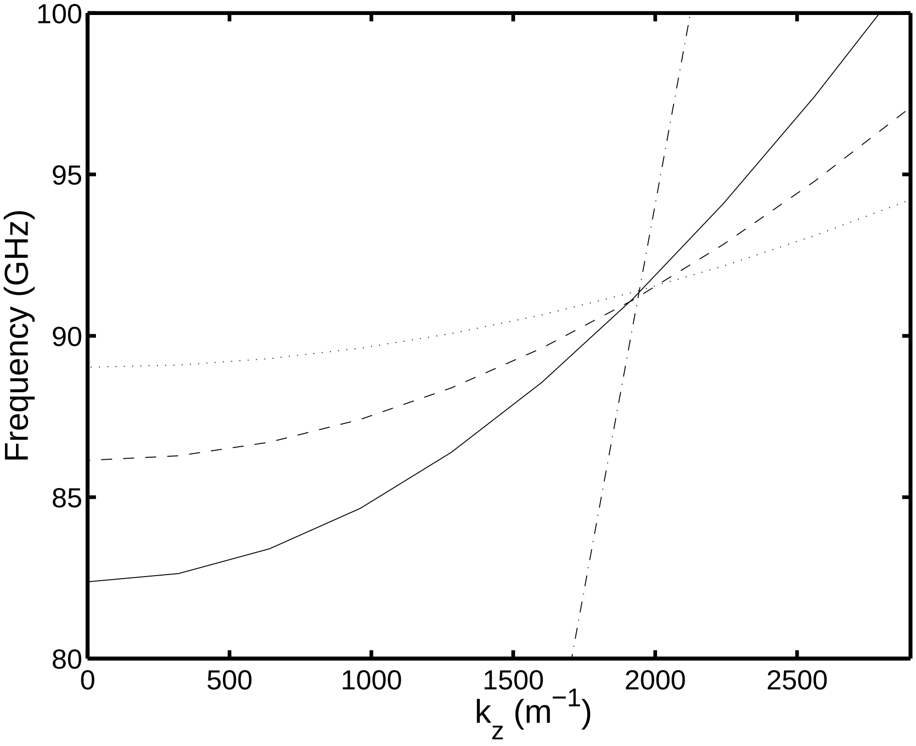

Figure 3.2: The dispersion relation according to Eq. (3.6) for three example structures listed in Table 3.1 for ε =5.5 (solid), 9.5 (dashed), and 20 (dotted) and including the speed of light line (dot-dashed).

$$k_2^2 = \varepsilon_r \frac{\omega^2}{c^2} - k_z^2. \tag{3.5}$$

Enforcing the boundary condition that E_z be continuous across the dielectric boundary gives the dispersion relation

$$\tan(k_1 a)\tan[k_2(b-a)] = \varepsilon_r \frac{k_1}{k_2}. \tag{3.6}$$

As a check, one can see that using this dispersion relation, imposes the other boundary conditions, namely

$$E_y(a^-) = \frac{E_y(a^+)}{\varepsilon_r} \quad \text{and} \quad B_x(a^-) = B_x(a^+). \tag{3.7}$$

The dispersion relation for the three example structures listed in Table 3.1 is shown in Fig. 3.2.

For acceleration we also have the requirement that the wave be synchronous with a speed of light particle $\omega/k_z = c$, thus implying

$$k_1 = 0 \tag{3.8}$$

$$k_2 = \frac{\omega}{c}\sqrt{\varepsilon_r - 1}. \tag{3.9}$$

At synchronism, the accelerating field has the nice property that it is uniform across the gap, while decaying sinusoidally to zero in the dielectric. The field components for $k_1 = 0$ are

$$E_z = Ge^{ik_z z - i\omega t}\begin{cases} 1 \\ \dfrac{\sin[k_2(b-y)]}{\sin[k_2(b-a)]} \end{cases} \tag{3.10}$$

$$E_y = -ik_z Ge^{ik_z z - i\omega t}\begin{cases} y \\ \dfrac{1}{k_2}\dfrac{\cos[k_2(b-y)]}{\sin[k_2(b-a)]} \end{cases} \tag{3.11}$$

$$B_x = \frac{ik_z}{c}Ge^{ik_z z - i\omega t}\begin{cases} y \\ \dfrac{\varepsilon_r}{k_2}\dfrac{\cos[k_2(b-y)]}{\sin[k_2(b-a)]} \end{cases} \tag{3.12}$$

where the dispersion condition at synchronism is

$$\tan[k_2(b-a)] = \frac{\varepsilon_r}{k_2 a}. \tag{3.13}$$

From this analysis a number of practical formulas emerge. One may show that the ratio of surface field to accelerating field at the conductor is

$$\frac{|E_y(b)|}{G} = \sqrt{\left(\frac{a\omega}{\varepsilon_r c}\right)^2 + \frac{1}{\varepsilon_r - 1}} \tag{3.14}$$

which is a fraction smaller than 1 for our geometry. In principle, the field ratio at the dielectric

$$\frac{|E_y(a)|}{G} = \frac{a\omega}{c} \tag{3.15}$$

is also a concern for breakdown, however is also less than 1.

To illustrate the field profile, consider the geometries with the parameters listed in Table 3.1. The E_z field profile in units of the structure dimension are shown in Fig. 3.3, where one can see that E_z/G is almost identical, but the surface normal field E_y/G is much less than 1 depending on the dielectric constant — a great advantage for high-gradient operation when concerned about breakdown.

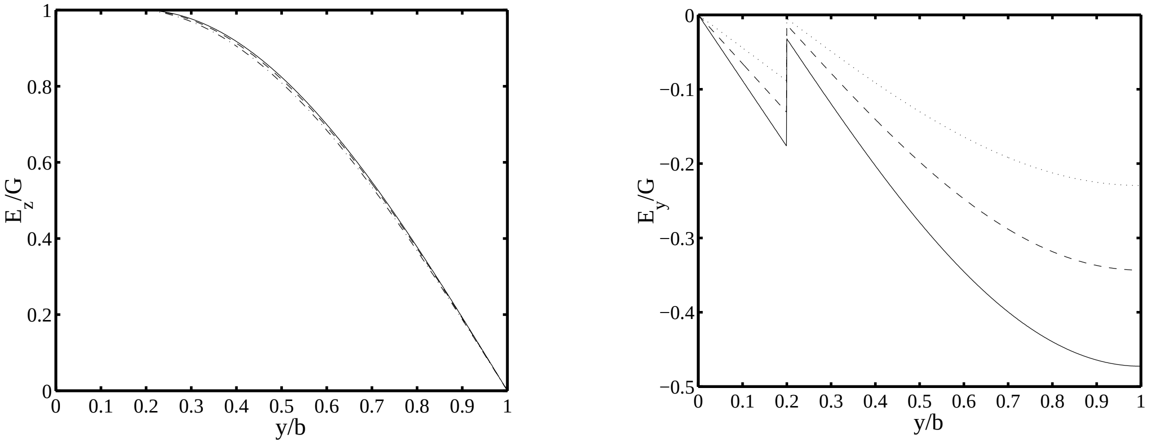

Figure 3.3: Plots of the normalized electric fields versus the structure dimension b for the three geometries listed in Table 3.1. They have almost identical E_z profiles (left), but have different surface fields E_y (right) for $\varepsilon = 20$ (dotted), 9.5 (dashed), and 5.5 (solid). The vacuum/dielectric interface is at $y/b = 0.2$.

3.2 Energy Considerations

The stored energy in the structure can be calculated with knowledge of the fields from Eqs. (3.1)-(3.3)

$$U = \frac{1}{4}\iiint (B \cdot D^* + B \cdot H^*) dV \tag{3.16}$$

$$= \frac{Wz\omega^2}{\mu c^4} G^2 \left\{ \frac{1}{k_1^2}\left[a - \frac{\sin 2k_1 a}{2k_1}\right] + \frac{\varepsilon_r \cos^2 k_1 a}{k_2^2 \sin^2 k_2(b-a)}\left[b - a - \frac{\sin 2k_2(a-b)}{2k_2}\right]\right\} \tag{3.17}$$

Table 3.1: Geometrical parameters for three structures with different dielectric materials and resonance at 91.4 GHz. The ratio $a/b = 0.2$ is held constant.

	MgCaTi	Alumina	Diamond
ε_r	20	9.5	5.5
a (μm)	46.4	68.6	92.5
b (μm)	232	343	463
a/b	0.2	0.2	0.2
v_g/c	0.05	0.1	0.2
α (m^{-1})	23.0	6.8	3.0
Q	800	1200	1600
E_y/G ($y = a$)	0.1	0.1	0.2
E_y/G ($y = b$)	0.2	0.3	0.5

and the power flowing through the structure is is calculated using the Poynting vector

$$P = \frac{1}{2}\iint E \times H^* dA \tag{3.18}$$

$$= \frac{\omega^2}{c^2}\frac{G^2}{Z_0}W\left[\frac{2a^3}{3} + \frac{b-a}{a}\left(\frac{a^3}{\varepsilon_r} + \frac{\varepsilon_r a}{k_2^2}\right) + \frac{a}{k_2^2}\right] \tag{3.19}$$

where W is the width of the structure.

The group velocity is found by

$$v_g = \frac{P}{(dU/dz)} \tag{3.20}$$

and at synchronism is

$$\frac{v_g}{c} = \frac{1 + A/\varepsilon_r}{1 + A}, \tag{3.21}$$

where we abbreviate

$$A = \left(\frac{b}{a} - 1\right)\left[1 + \frac{\varepsilon_r}{k_2^2 a(b-a)} + \left(\frac{\varepsilon_r}{k_2 a}\right)^2\right] \tag{3.22}$$

A useful approximate solution to the dispersion relation corresponds to the limit $\varepsilon_r\left(\frac{b-a}{a}\right) \gg 1$ and is given by

$$k_2 \approx \frac{\pi/2}{b-a}. \tag{3.23}$$

An illustrative design would take $G = 1$ GV/m, in a structure with resonance at $\omega/2\pi \approx 91.4$ GHz, dimensions $a = 300\ \mu$m, $b = 550\ \mu$m, and $\varepsilon_r = 9.5$. The group velocity is given by $v_g/c \approx 1/\varepsilon_r \approx 0.1$ and taking $W \approx b$ the power required is 500 MW. This structure scaled down from a free-space wavelength of 3.3 mm to 1.5 μm would require 100 W for the same gradient.

3.3 Circuit Model

In the foregoing, the traveling wave structure of Fig. 3.1 is discussed; however, this is only part of the millimeter wave circuit. The complete structure must facilitate power flow by means of input and output waveguide and coupling cavities. Logically, the circuit consists of connecting waveguide, an input coupling cavity, the dielectric transmission line, an output coupling cavity, and another connecting waveguide. As an accelerator, and an rf circuit, this system may be modeled as two coupled cavities connected by a transmission line. We will build this model first considering a single cavity coupled to waveguide, then advance to a cavity coupled to two waveguides and at last arriving to the completed circuit of Fig 3.8, the planar dielectric accelerator.

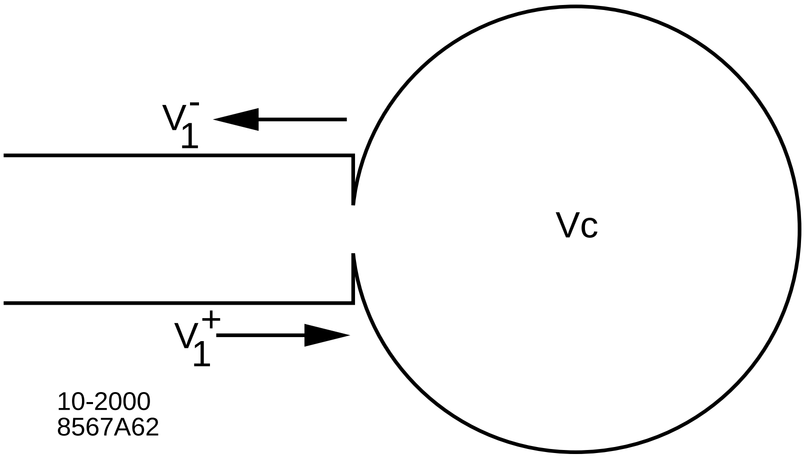

Figure 3.4: Cavity with input waveguide.

3.3.1 Single Cavity

Beginning with the conceptually simple problem of a cavity resonator coupled to a waveguide, revisiting the *RLC* equivalent circuit of Fig. 2.1 and Eq. (2.13),

$$\left(\frac{d^2}{dt^2}+\omega_o^2\right)V_c=-\frac{\omega_o}{Q_w}\frac{d}{dt}V_c+\frac{\omega_o}{Q_{e_1}}\frac{d}{dt}\left(V_1^+-V_1^-\right) \tag{3.24}$$

where V_1^+ is voltage into the cavity from the waveguide and V_1^- is the outgoing voltage. Again, Q_w is the quality factor describing power loss into the cavity walls and Q_{e_1} describes the coupling of the cavity to the waveguide. A continuity condition at the coupling iris is

$$V_c=V_1^++V_1^-. \tag{3.25}$$

We will make use of the definition of "loaded" quality factor

$$\frac{1}{Q_L}=\frac{1}{Q_w}+\frac{1}{Q_{e_1}}, \tag{3.26}$$

to rewrite Eq. (3.24) in the form

$$\left(\frac{d^2}{dt^2}+\frac{\omega_o}{Q_L}\frac{d}{dt}+\omega_o^2\right)V_c=2\frac{\omega_o}{Q_{e_1}}\frac{d}{dt}V_1^+. \tag{3.27}$$

We are interested in the steady-state solution, and assume the solution has the form $e^{-i\omega t}$,

$$\left(-\omega^2-\frac{i\omega\omega_o}{Q_L}+\omega_o^2\right)V_c=-2i\omega\omega_o\left(\frac{V_1^+}{Q_{e_1}}\right) \tag{3.28}$$

and we define the tuning angle

$$\tan\psi = Q_L\left(\frac{\omega_o}{\omega} - \frac{\omega}{\omega_o}\right) \tag{3.29}$$

to yield the voltage in an externally powered resonator cavity

$$V_c = 2Q_L e^{-i\psi}\cos\psi\left(\frac{V_1^+}{Q_{e_1}}\right). \tag{3.30}$$

The cavity can be characterized on the bench by application of a voltage through the waveguide and measuring the reflected signal. The ratio of the reflected signal to the input signal gives the scattering matrix parameter,

$$S_{11} = \frac{V_1^-}{V_1^+} = \frac{V_c - V_1^+}{V_1^+} = 2\frac{Q_L}{Q_{e_1}}e^{-i\psi}\cos\psi - 1. \tag{3.31}$$

In Ch. 4 contains discussion of the design and fabrication of microwave cavities where the cavity is required to be "matched" and "tuned" and to have a high Q. It is illustrative at this point to understand what this means in terms of S_{11}. A tuned cavity means it has a desired resonance frequency, or S_{11} is a minimum at the desired frequency. That the cavity be matched means that there is no reflected signal from the cavity, namely $S_{11} = 0$ on resonance. This match condition is

$$\beta \equiv \frac{Q_w}{Q_{e_1}} = 1. \tag{3.32}$$

The answer is obvious at match, but when the minimum of $|S_{11}| \neq 0$, it is not possible to know whether a cavity is over- or under-coupled without knowing the relative phase of the forward and reflected signals, as illustrated in the left-hand plot of Fig. 3.5 where $|S_{11}|$ is plotted for three cavities, where $\beta = 1$ (matched case), 2 (over-coupled case) and 0.5 (under-coupled case). From the plot of $|S_{11}|$, Q_L can be inferred from the width, but the over- and under-coupled cases look identical. A convenient tool for this analysis is called a Smith chart, as in the right hand plot of Fig. 3.5, where the complex S_{11} is plotted directly, revealing the couplings β read from the horizontal axis. We do not wish to delve into the intricacies of Smith charts, but only would like to point out their usefulness for this case.

3.3.2 Two Port Cavity

Understanding of the previous case of a single-port cavity is necessary for understanding the more important problem of a two-port cavity. This cavity, depicted in Fig. 3.6,

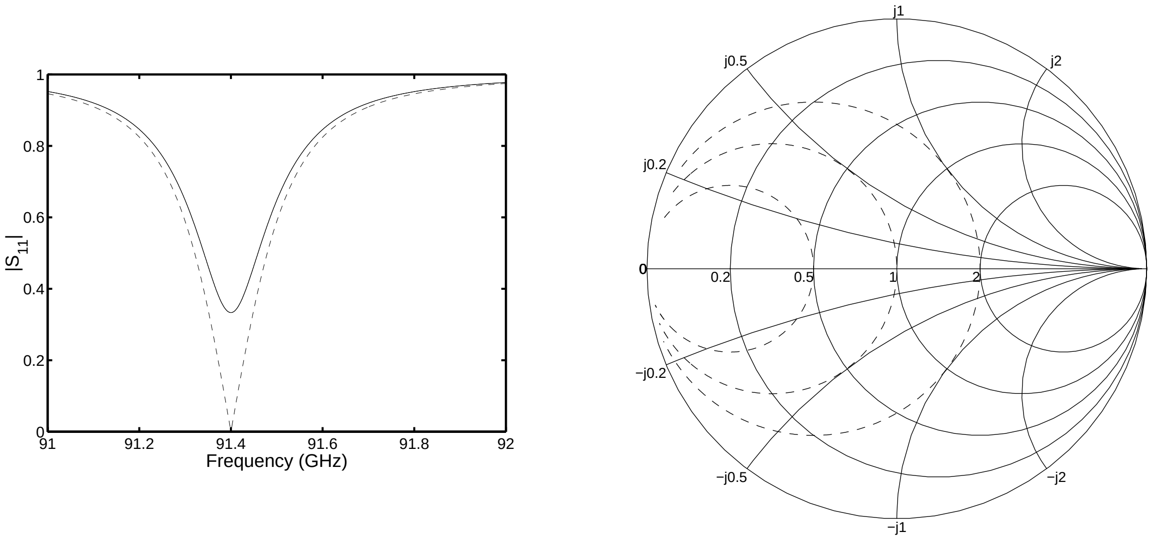

Figure 3.5: S_{11} for three cavities with the same Q_L, one is matched, one is over-coupled and the other under-coupled. The left hand plot of $|S_{11}|$ shows the matched case (dashed) and the over- and under-coupled cases (solid) are indistiguishable. The Smith chart, however not only distinguishes the three (dashed), but readily reveals their coupling $\beta = 0.5$, 1, and 2 read off of the horizontal axis.

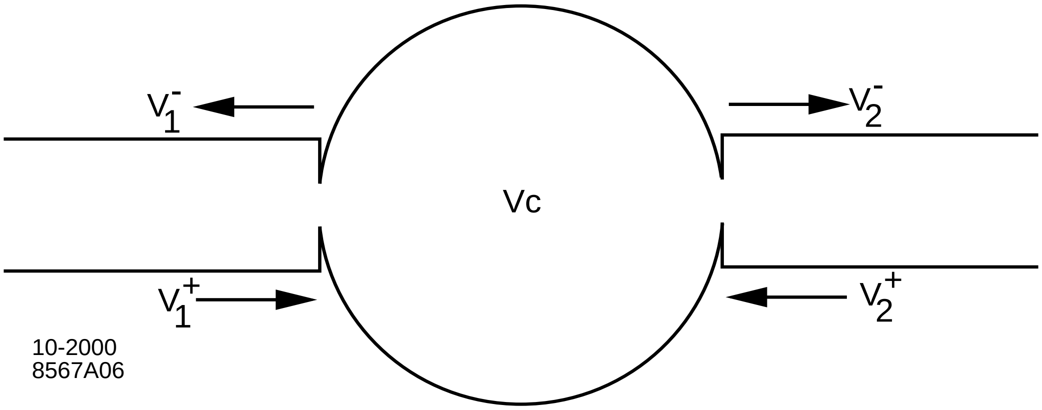

Figure 3.6: Cavity with 2 ports.

is coupled to waveguide through two irises. The problem takes the form in the time domain,

$$\left(\frac{d^2}{dt^2}+\omega_o^2\right)V_c=-\frac{\omega_o}{Q_w}\frac{d}{dt}V_c+\frac{\omega_o}{Q_{e_1}}\frac{d}{dt}\left(V_1^+-V_1^-\right)+\frac{\omega_o}{Q_{e_2}}\frac{d}{dt}\left(V_2^+-V_2^-\right) \tag{3.33}$$

where we denote voltage into the cavity with a plus (+) and voltage coming out with a minus (-). The external coupling Q_{e_1} refers to the coupling to the waveguide on the left side in Fig. 3.6 and Q_{e_2}, the right. Similar to the previous case, the loaded Q is

$$\frac{1}{Q_L}=\frac{1}{Q_w}+\frac{1}{Q_{e_1}}+\frac{1}{Q_{e_2}}. \tag{3.34}$$

and again we have the condition that the voltage sum at the irises are equal to the cavity voltage

$$V_1^+ + V_1^- = V_c = V_2^+ + V_2^-. \tag{3.35}$$

Substituting the previous equations, we find

$$\left(\frac{d^2}{dt^2}+\frac{\omega_o}{Q_L}\frac{d}{dt}+\omega_o^2\right)V_c=2\frac{\omega_o}{Q_{e_1}}\frac{d}{dt}V_1^+ + 2\frac{\omega_o}{Q_{e_2}}\frac{d}{dt}V_2^+ \tag{3.36}$$

and we assume a solution with the form $e^{-i\omega t}$ to find a similar form to the single-port case

$$V_c=2Q_L e^{-i\psi}\cos\psi\left(\frac{V_1^+}{Q_{e_1}}+\frac{V_2^+}{Q_{e_2}}\right). \tag{3.37}$$

where the tuning angle ψ is defined by Eq. (3.29).

In the case of two-ports, there are four S-matrix elements,

$$S_{11}=\frac{V_1^-}{V_1^+}=\frac{V_c-V_1^+}{V_1^+}=2\frac{Q_L}{Q_{e_1}}e^{-i\psi}\cos\psi-1 \tag{3.38}$$

$$S_{12}=S_{21}=n\frac{V_2^-}{V_1^+}=n\frac{V_c-V_2^+}{V_1^+}=\frac{2Q_L e^{-i\psi}\cos\psi}{\sqrt{Q_{e_1}Q_{e_2}}} \tag{3.39}$$

$$S_{22}=\frac{V_2^-}{V_2^+}=\frac{V_c-V_2^+}{V_2^+}=2\frac{Q_L}{Q_{e_2}}e^{-i\psi}\cos\psi-1 \tag{3.40}$$

where $n=\sqrt{Q_{e_1}/Q_{e_2}}$ is a normalization factor. These equations can be compared to Eq. (3.31) in the limit that $Q_{e_2}\to\infty$. A consequence of finite wall losses is that one cannot match a cavity from both ports, as illustrated in Fig. 3.7.

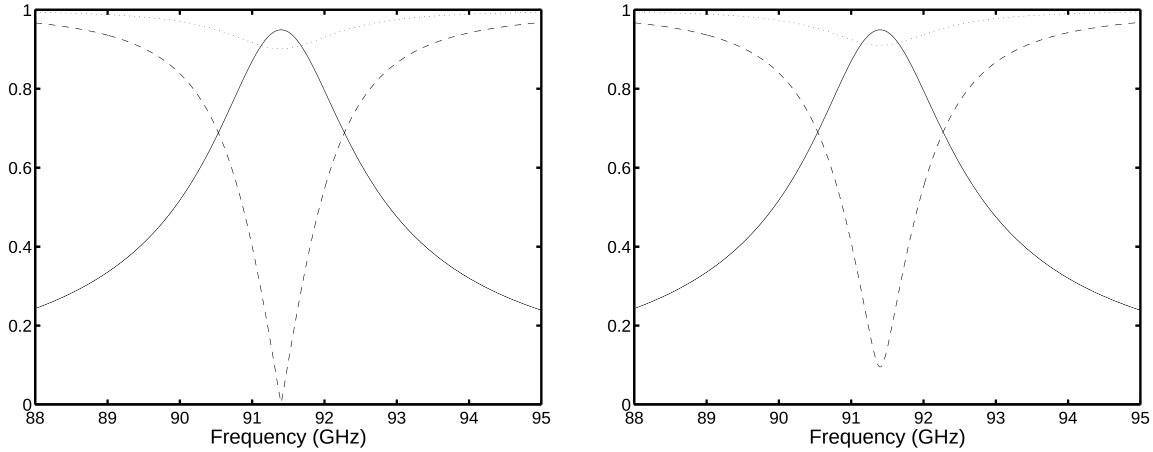

Figure 3.7: Reflection — S_{11} (left, dashed) and S_{22} (right, dashed) — and transmission — S_{21} (left, solid) and S_{12} (right, solid) — characteristics for a cavity with 2 ports having finite wall losses, $Q_w = 1000$, where $Q_{e_1} = 100$ and $Q_{e_2} = 110$. The cavity cannot be matched from both ports if there are wall losses.

3.3.3 Combined Circuit Elements

Before moving to the PDA as a completed circuit, it is useful to develop a tool for combining circuit elements. Often we have components with an input and an output and the corresponding scattering matrices for them. When we connect these elements together, we might want to know how the new input and output will behave.

Denoting + for wave moving to the right and - for waves moving to the left (note the slight difference from the previous case for the cavity), we have for element #1

$$V_1^- = A_{11}V_1^+ + A_{12}V_2^- \tag{3.41}$$

$$V_2^+ = A_{21}V_1^+ + A_{22}V_2^- \tag{3.42}$$

and for element #2,

$$V_3^- = B_{11}V_3^+ + B_{12}V_4^- \tag{3.43}$$

$$V_4^+ = B_{21}V_3^+ + B_{22}V_4^- \tag{3.44}$$

Next, connect the elements A and B together with length L of waveguide having phase length, kL, and attenuation, αL, according to $\Gamma \equiv e^{-ikL-\alpha L}$ giving the propagated voltages

$$V_3^+ = \Gamma V_2^+ \tag{3.45}$$

$$V_2^- = \Gamma V_3^- \tag{3.46}$$

Solving for V_1^- and V_4^+ in terms of V_1^+ and V_4^-, the resulting S-matrix is

$$S = \begin{pmatrix} A_{11} + \frac{\Gamma^2 A_{12} B_{11} A_{21}}{1-\Gamma^2 B_{11} A_{22}} & \frac{\Gamma A_{12} B_{12}}{1-\Gamma^2 B_{11} A_{22}} \\ \frac{\Gamma B_{21} A_{21}}{1-\Gamma^2 B_{11} A_{22}} & B_{22} + \frac{\Gamma^2 B_{21} A_{22} B_{12}}{1-\Gamma^2 B_{11} A_{22}} \end{pmatrix} \tag{3.47}$$

where the combined element can now be described by the incoming and outgoing voltages according to

$$\begin{pmatrix} V_1^- \\ V_4^+ \end{pmatrix} = S \begin{pmatrix} V_1^+ \\ V_4^- \end{pmatrix}. \tag{3.48}$$

This formula is helpful for concatenating a series of elements such as windows, structures, phase-shifters, as well as the immediate case for two cavities coupled by a transmission line. We also note that this result can be applied to a series of coupled cavities, to electrically model a disk loaded waveguide structure.

3.3.4 The PDA Circuit

The PDA circuit of Fig. 3.8 has an input cavity characterized by the parameters: Q_{e_1}, the external quality factor quantifying the coupling between the cavity and waveguide, Q_{e_2}, characterizing coupling between cavity and dielectric line, ω_1, the cavity resonance frequency, and Q_{w_1}, the cavity wall quality factor. Likewise for the output cavity, we have Q_{e_4}, Q_{e_3}, ω_2 and Q_{w_2}.

From Eqs. (3.38)-(3.40) we get the scattering matrix elements for the input cavity viewed as a two-port cavity

$$A_{11} = \frac{V_1^-}{V_1^+} = \frac{V_{c_1} - V_1^+}{V_1^+} = 2\frac{Q_{L_1}}{Q_{e_1}} e^{-i\psi_1} \cos\psi_1 - 1 \tag{3.49}$$

$$A_{12} = A_{21} = n\frac{V_{c_1} - V_2^+}{V_1^+} = \frac{2Q_{L_1} e^{-i\psi_1} \cos\psi_1}{\sqrt{Q_{e_1} Q_{e_2}}} \tag{3.50}$$

$$A_{22} = \frac{V_2^-}{V_2^+} = \frac{V_{c_1} - V_2^+}{V_2^+} = 2\frac{Q_{L_1}}{Q_{e_2}} e^{-i\psi_1} \cos\psi_1 - 1 \tag{3.51}$$

where $n_1 = \sqrt{Q_{e_1}/Q_{e_2}}$. In the same way we arrive at the scattering matrix elements for the output cavity

$$B_{11} = \frac{V_3^-}{V_3^+} = \frac{V_{c_2} - V_3^+}{V_3^+} = 2\frac{Q_{L_2}}{Q_{e_3}} e^{-i\psi_2} \cos\psi_2 - 1 \tag{3.52}$$

$$B_{12} = B_{21} = n_2\frac{V_{c_2} - V_4^+}{V_3^+} = \frac{2Q_{L_2} e^{-i\psi_2} \cos\psi_2}{\sqrt{Q_{e_3} Q_{e_4}}} \tag{3.53}$$

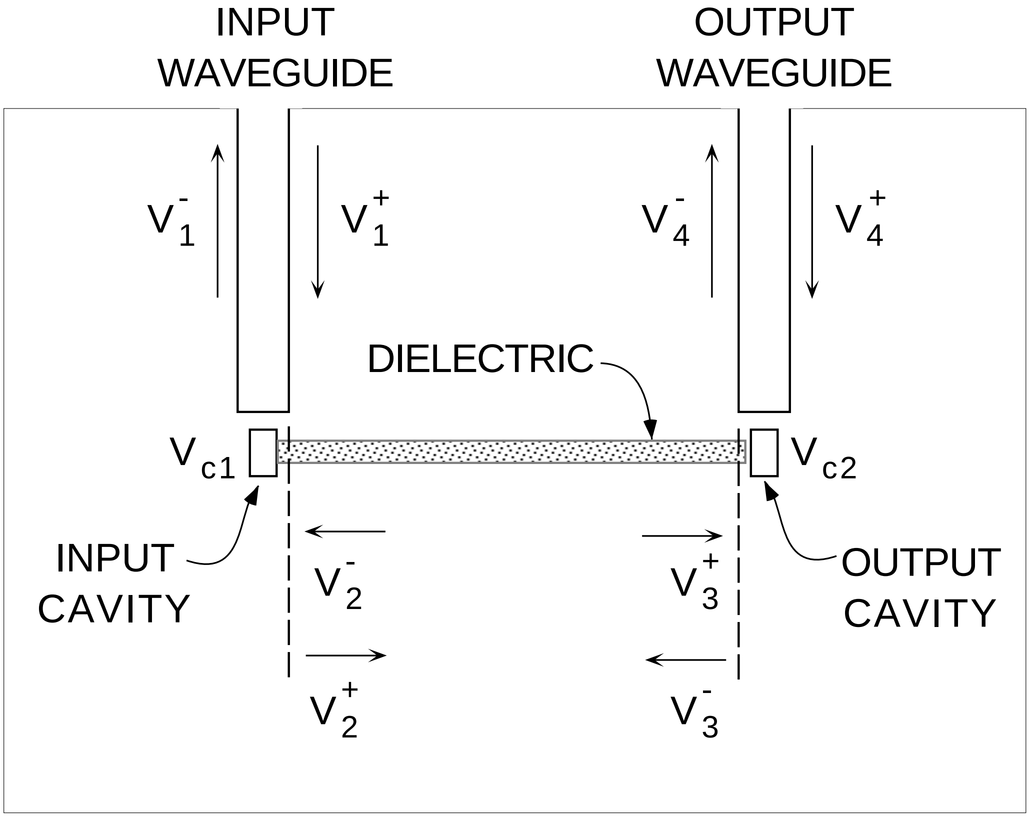

Figure 3.8: Sketch of dielectric structure indicating input, output, and transmission line voltages.

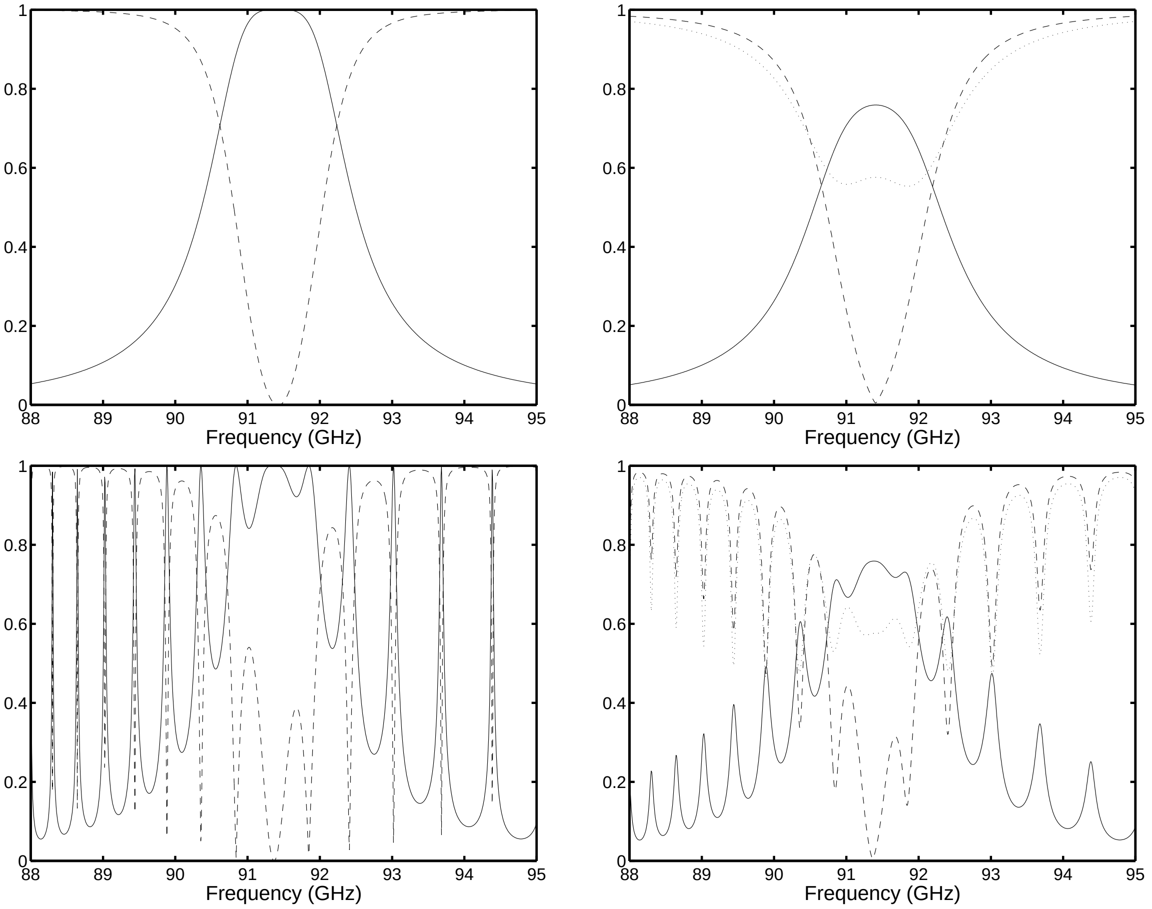

Figure 3.9: Transmission, S_{21} (solid), reflection S_{11} (dashed) and the power sum $S_{11}^2 + S_{21}^2$ (dotted) for a coupled cavities without losses (left) and with realistic losses (right). The top two plots correspond to zero dispersion in the dielectric line; the bottom two include dispersion. Notice the frequency spacing of the peaks (proportional to the group velocity) decreasing as the frequency approaches cut-off, $f_c = 87$ GHz.

$$B_{22} = \frac{V_4^-}{V_4^+} = \frac{V_{c_2} - V_4^+}{V_4^+} = 2\frac{Q_{L_2}}{Q_{e_4}} e^{-i\psi_2} \cos\psi_2 - 1 \tag{3.54}$$

where $n_2 = \sqrt{Q_{e_3}/Q_{e_4}}$. From the results of the previous section, Eq. (3.47), one can concatenate the input and output cavity S-matrices using the transmission line characteristics: length L, phase length, $k_z L$, and attenuation, αL, described by $\Gamma = e^{-(ik_z+\alpha)L}$, where the dispersion relation for the dielectric line is given implicitly by Eq. (3.6). To illustrate the effect of dispersion on the circuit, the top two plots of Fig. 3.9 are are for a line with zero dispersion and the bottom two include realistic dispersion where the left hand plots have zero loss and the right ones have include loss with $Q_w = 1000$, and $\alpha = 7.7\mathrm{m}^{-1}$.

Here we must also consider that the propagation constant through the transmission line varies with the frequency. The dispersion in the dielectric waveguide is

$$k = \sqrt{\varepsilon}\sqrt{\left(\frac{\omega}{c}\right)^2 - \left(\frac{2\pi f_c}{c}\right)^2} \tag{3.55}$$

where f_c is the cut-off frequency of the dielectric line. Figs. 4.16 & 4.17 show the inclusion of this dispersion through the line.

Chapter 4

RF Design and Bench Test

To assess the feasibility of building a W-band accelerator, one could make a miniature accelerator modeled after the SLC 3-m structures scaled down by a factor of 32 to give a structure length of only a few inches. In fact, what we have done is illustrated in Fig. 4.1. This series of tests of increasing complexity allowed us to develop the essential components necessary for a working W-band accelerator. In Test #1 we studied the simple circuit of a single cell cavity and rf window. In Test #2, we tested a 1 inch long dielectric structure, employing two rf windows. Finally, in Test #3 we studied the same dielectric structure at high fields employing a phase-shifting power recirculation arm. These four components are described in this chapter.

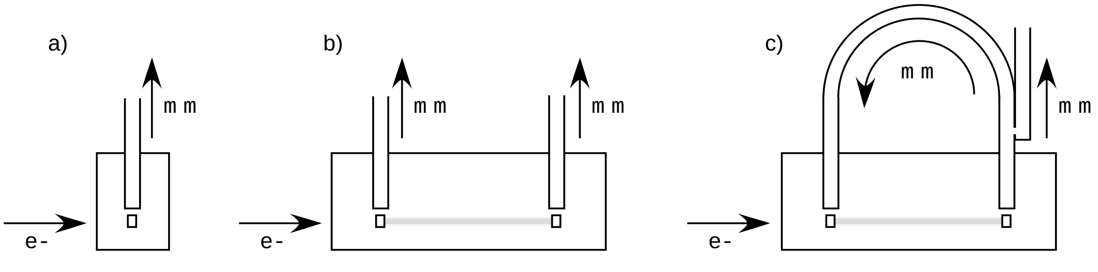

Figure 4.1: Series of tests of increasing complexity performed to prove the feasibility of building a W-band linac: a) Test #1 studied a single cavity resonator and rf window, b) Test #2 was a study of a planar dielectric accelerator structure utilizing two more rf windows and two high power attenuators, and c) Test #3 studied the same PDA under even higher field levels in a traveling-wave resonator circuit.

4.1 Manufacturing Considerations

The frequency of interest is 91.392 GHz having a free space wavelength of 3.28 mm. Many accelerator components, especially the accelerator structure itself, are single moded devices, meaning that for a given frequency only one mode is excited. The dimensional scale is therefore set by the wavelength and the tolerance determined by the quality factor Q. Much of the effort at W-band concentrates on the manufacture of these millimeter-scale components with μm-scale tolerances. Thus the design of W-band components must take into consideration the technology used for manufacturing.

4.1.1 Electro-discharge Machining

The technology chosen for most of this W-band work is electro-discharge machining (EDM), thanks to its ready availability. EDM is a "non-contact" machining process that vaporizes material near its electrode made of a wire or conductive mandrel. Intense pulses of DC voltage (50-100 V) are applied to the wire that creates an electrical spark at very high temperature between the electrode and the cut metal. The temperature is between 5000 and 10,000°C, enough to vaporize most metals. The wire is continuously fed during the cutting process to replace used wire. EDM has proven to be an effective means of machining structures to tight tolerances of 3 μm, or better, over a 1 inch length. Intrinsic to the EDM process, the wire electrode leaves a "rough" machined surface. One must be careful to avoid pitting or redeposition of material on the cut walls. It was our experience that machining to a class 20 (20×10^-6" or 0.5 μm rms) surface was regularly achieved. Generally one aims for a roughness average $R_a \ll \delta \approx 0.2$ μm, the RF skin depth, to avoid a geometric increase in the effective wall area, and therefore a diminution in the wall Q,

$$\frac{1}{Q} \approx \frac{\delta}{2} \frac{\int H^2 dA}{\int H^2 dV}. \tag{4.1}$$

Often, another chemical or abrasive process is required to achieve the desired surface finish. We have investigated both methods using chemical polishing and "sand blasting" to be discussed presently.

4.1.2 Brazing

Induced RF currents are not only impeded by a rough surface, but also by a poor conducting joint between materials. Considering that most components must be cut from more than one piece of metal, a process must be used to bond the parts together to provide a current carrying joint. For this purpose, we often choose high temperature oven brazing for bonding parts together. High temperature brazing also provides a sterile environment for parts that will be used in ultra high vacuum (10^{-9}–10^{-7} torr). For this bonding we use two techniques: high temperature brazing and diffusion bonding. High temperature oven brazing requires a thin layer of braze material that forms a eutectic between the two layers of metal to be bonded. One chooses a braze material that has a melting point lower than that of the metals to be bonded. A series of brazing steps can be made by using brazing materials of different melting points. Choosing the highest temperature braze first and lower temperature brazes in succession is a logical approach when several braze steps are required. Diffusion bonding on the other hand, does not require a "catalyst" material but two metals (of the same material) to be bonded are raised to very near their melting points where mechanical pressure imposed near the joint facilitates diffusion between the two layers forming a solid joint. The advantage of diffusion bonding is that there are no fillets formed by a brazing material near the joint.

Dielectrics generally do not readily bond to metals, therefore a metalization layer must be formed for brazing the dielectric to a copper substrate. Using an active braze alloy (CuSilABA), we have reliably brazed copper and dielectric materials, e.g. alumina ceramic and diamond. The braze alloy contains a small amount of titanium, which is a highly reactive metal, that "hooks" into the dielectric that provides the metalization layer for bonding the dielectric to the metal and brazes in a single step.

4.1.3 Quality Assurance

To assess the quality of manufacture via EDM and bonding we employ RF measurements to determine the resonance frequency and quality factor. These measurements are made using a W-band vector network analyzer (VNA). The analyzer can measure s-cattering parameters of the components under test from which we can infer the resonance frequency, Q and insertion loss. Our VNA measurements assume, as is typical with these measurements, single mode propagation in the connecting waveguide. The waveguide used for these measurements at W-band is called "waveguide, rectangular 10/100ths of an inch wide", or WR10. WR10 with a height to width aspect ratio of 1:2 gives single mode propagation in the range of the TE_{10} and the TE_{20} mode cutoffs at 59 and 118 GHz, respectively.

As in Ch. 3, knowledge of the fields in the waveguide allows for calculation of the dispersion relation

$$\left(\frac{\omega}{c}\right)^2 = \left(\frac{\pi}{a}\right)^2 + k_z^2 \tag{4.2}$$

and attenuation

$$\alpha = \frac{R_s}{Z_0}\left[\frac{\omega^2}{c^2}\frac{1}{b} + \frac{2\pi^2}{a^3}\right]\frac{c}{\omega}\frac{1}{k_z}. \tag{4.3}$$

Meanwhile the VNA itself operates in the range of 75 to 110 GHz, limited by the frequency range of the harmonic mixer, a Hewlett Packard model 11970W. This model is an 18× harmonic mixer with a 48 dB conversion loss, a sensitivity of $1\text{mV}/1\mu\text{W}$, and a dynamic range of -40 to 20 dBm. The VNA has a dynamic range of 40 dB limited by a W-band power source of 0 dBm.

4.1.4 Waveguide Attenuation Example

Prior to discussion of various network elements, we will describe the most basic example, that of a 2" long piece of WR10 waveguide. We consider commercial waveguide for comparison with a custom waveguide made from oxygen-free electron (OFE) grade copper cut using wire EDM.

To understand the effect of surface roughness on wall loss associated with the EDM process, we performed a series of measurements on two-2" lengths of WR10 waveguide. In these measurements, a "fine" cut and a "rough" cut waveguide were made with wire EDM. The rough cut waveguide was cut using wire EDM in a single pass with the cutting wire. The fine cut piece was cut in three passes of the EDM wire, each pass removing substantially less material than the previous, meant to give a smooth surface finish. This set of measurements, initiated by P. Chou, revealed that the fine cut waveguide had significantly less attenuation than the rough cut guide [25], results listed in Table 4.1.

Taking the rough cut waveguide, we performed a study of the effect from chemical cleaning (CC) and chemical polishing (CP) on surface losses. The CC process was intended to remove any contaminates and should not have caused any etching of the metal, step listed in Table 4.2. The CP process was intended to remove several microns of copper from the surface, listed in Table 4.3. Data for transmitted power were taken for three scenarios: (1) no waveguide, (2) a 2" piece of Aerowave waveguide and (3) the 2" EDM'd rough cut waveguide. The attenuation was then calculated by subtracting the power transmitted through the waveguides from the power transmitted with no waveguide, (1)-(2) and (1)-(3).

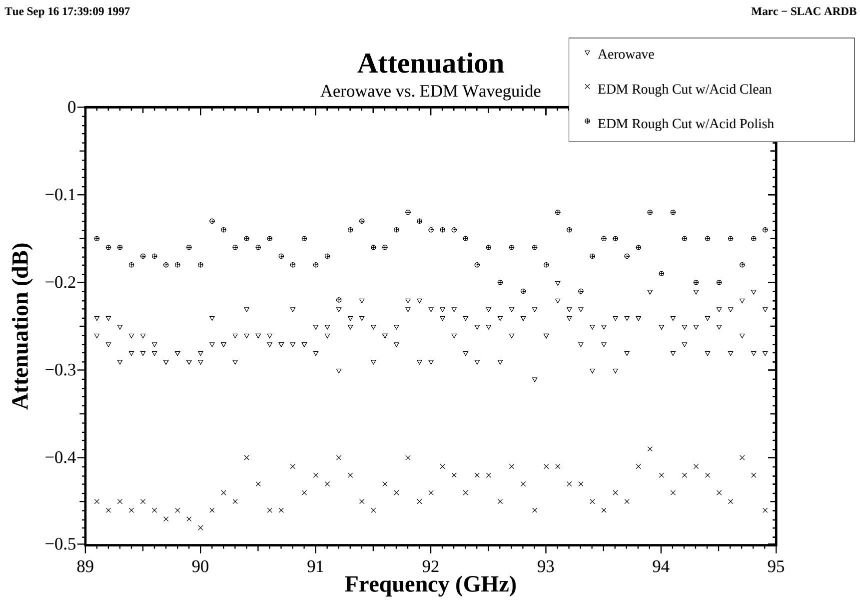

Figure 4.2: Waveguide attenuation for two sets of waveguide described in the text.

These results are plotted in Fig. 4.2 and summarized in Table 4.1, including the theoretical value from Eq. (4.3).

The CC process showed negligible difference, however the CP process gave a surprisingly large improvement. Comparison of the CP'd rough cut waveguide with the fine cut waveguide one can see that the CP'd waveguide has lower attenuation, within 20% of the theoretical ideal. Whether similar improvements can be obtained in a more complicated structure, *i.e.* a disk-loaded structure, is not clear. While the W-band structure

Table 4.1: Average attenuation at 90 GHz for a 2" long section of OFE copper WR10.

Waveguide	Attenuation
OFE Cu (theoretical)	0.13 dB
CP EDM WG	0.16 dB
Fine Cut WG (16 jun 97)	0.20 dB
Aerowave WG (5 aug 97)	0.26 dB
Aerowave WG (12 sep 97)	0.25 dB
Rough Cut WG (16 jun 97)	0.42 dB
CC EDM WG	0.44 dB

Table 4.2: Series of step use for Chemical Cleaning of OFE copper. There are no chemicals in the sequence that will etch copper.

- Step 1 Vapor degrease in **1,1,1 Trichloroethane** for five minutes.
- Step 2 Alkaline soak clean using **Enbond Q527** for five minutes at a temperature of 180°F.
- Step 3 Cold tap water rinse for two minutes
- Step 4 Immerse in 10% by volume **Metex 9268** acid solution at room temperature for five minutes.
- Step 5 Cold tap water rinse for two minutes.
- Step 6 Immerse in **Metex 629** acid solution for 30 seconds.
- Step 7 Tap water rinse for one minute.
- Step 8 Deionized water rinse for one minute.
- Step 9 Cold tap water rinse for one minute.
- Step 10 Cold deionized water rinse for one minute (minimum resistivity of 1,000,000 ohms-cm).
- Step 11 Hot deionized water rinse for thirty seconds (minimum resistivity of 1,000,000 ohms-cm).
- Step 12 Immerse in analytical reagent grade **Isopropyl Alcohol** at 115°F for thirty seconds.
- Step 13 Blow dry with a dry nitrogen blast.
- Step 14 Dry in air oven at 150°F.
- Step 15 Wrap in lint-free paper and aluminum foil.

Table 4.3: Series of steps used in the Chemical Polishing of OFE copper. Chemical etching of the copper is performed in Step 6.

- Step 1 Vapor degrease in **1,1,1 Trichloroethane** for five minutes.
- Step 2 Alkaline soak clean in **Enbond Q527** for 5 minutes at 180°F.
- Step 3 Cold tap water rinse for two minutes.
- Step 4 Immerse in 50% **Hydrochloric Acid** at room temperature for one minute.
- Step 5 Cold tap water rinse for two minutes.
- Step 6 Immerse in the following solution for maximum of one minute depending on the surface finish required.

Phosphoric Acid, 75%	21 gallons
Nitric Acid, 42° Baumè	7 gallons
Acetic Acid, glacial	2 gallons
Hydrochloric Acid, analytical grade	19.2 fluid ounces
Temperature	Room

- Step 7 Cold tap water rinse for minimum of two minutes until the film on part disappears.
- Step 8 Cold tap water rinse for minimum of two minutes until the film on part disappears.
- Step 9 Cold deionized water rinse for one minute (minimum resistivity of 1,000,000 ohms-cm).
- Step 10 Cold tap water rinse for one minute.
- Step 11 Cold deionized water rinse for one minute (minimum resistivity of 1,000,000 ohms-cm).
- Step 12 Cold deionized water rinse for one minute (minimum resistivity of 1,000,000 ohms-cm).
- Step 13 Hot deionized water rinse for thirty seconds (minimum resistivity of 1,000,000 ohms-cm).
- Step 14 Immerse in analytical reagent grade **Isopropyl Alcohol** at 115°F for thirty seconds.
- Step 15 Blow dry with a dry nitrogen blast.
- Step 16 Dry in air oven at 150°F.
- Step 17 Wrap in lint-free paper and aluminum foil.

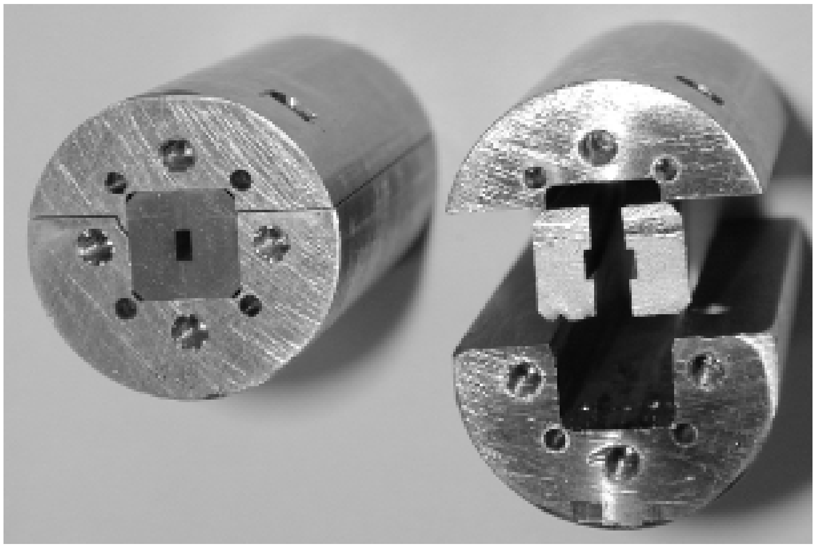

Figure 4.3: Picture of two high-power attenuators assembled (left) and un-assembled (right). The waveguide has high attenuation due to a rough surface finish and a cut along its narrow current-carrying wall.

might tolerate uniform etching of up to 1 μm of copper, the CP process would more likely preferentially etch corners and other sharp features.

4.2 High Power Attenuators

To perform high-power beam-driven experiments, we required a high-power, vacuum compatible attenuator to avoid taking multi-kW signals into air. The attenuators are pictured in Fig. 4.3, made by machining two halves of WR10 waveguide from stainless steel (304L for vacuum compatibility) and combining them with a jig that aligns the waveguide and provides for the WR10 flange pattern on each face when bolted together. As discussed, a clamped structure is ill advised in general due to poor conductivity near RF current carrying joints, causing poor match and high losses. In this case, we were taking advantage of the poor contact to increase attenuation. Repeatability of the interconnect was maintained in consecutive RF transmission measurements after assembly and disassembly. Fig. 4.4 shows the attenuation of two such attenuators having attenuation of 6.5 dB and 3.5 dB and VSWR < 1.1 at 91.4 GHz. The difference in attenuation was because one set of waveguide was "green-fired" in a wet hydrogen brazing furnace where a chrome-oxide layer is formed on the surface. The result was that the "greened" waveguide had less attenuation than the

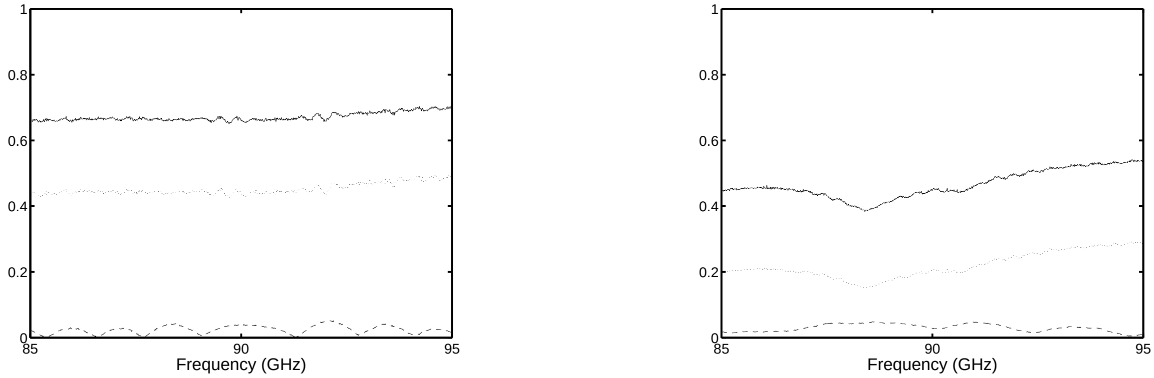

Figure 4.4: Transmission, S_{21} (solid), reflection, S_{11} (dashed) and insertion loss, $S^2 = S_{21}^2 + S_{11}^2$ (dotted) for the two attenuators used in Test #2. The insertion losses for the input (left) and the output (right) attenuators are 3.5 dB and 6.4 dB, respectively, at 91.4 GHz.

untreated set.

4.3 Single Cell

In Ch. 3 we discussed the theory of a single cavity resonator coupled to waveguide. In this section we discuss measurements for such a miniature cavity with WR10 output, and 680-μm diameter beam tube, prepared for excitation by the relativistic electron beam of the NLCTA. We establish that the 3.3-mm wavelength (91.4 GHz) scale is accessible to modern machining (EDM, diffusion bonding) and measurement techniques, and provides the basis for understanding of cavity performance as a transfer structure.

4.3.1 Tolerances

To appreciate the machining and tuning tolerances involved it is helpful to consult the circuit-equivalent picture of the application, as seen in Fig. 4.5. A beam bunched at 11.424 GHz passes through the beam tube, exciting the cavity resonance at the 8th beam harmonic, 91.392 GHz. The beam pulse length of 100 ns is much longer than the loaded fill time of the cavity ($T_f \approx$1.5 ns), so that steady-state is reached early in the pulse. In steady-state, the cavity voltage $\tilde{V}_c$ may be may be expressed in terms of the beam current $\tilde{I}_b$ from Eq. (2.13),

$$\tilde{V}_c = -\frac{1}{2}\cos\psi\, e^{j\psi}\, Q_L \left[\frac{R}{Q}\right] \tilde{I}_b, \tag{4.4}$$

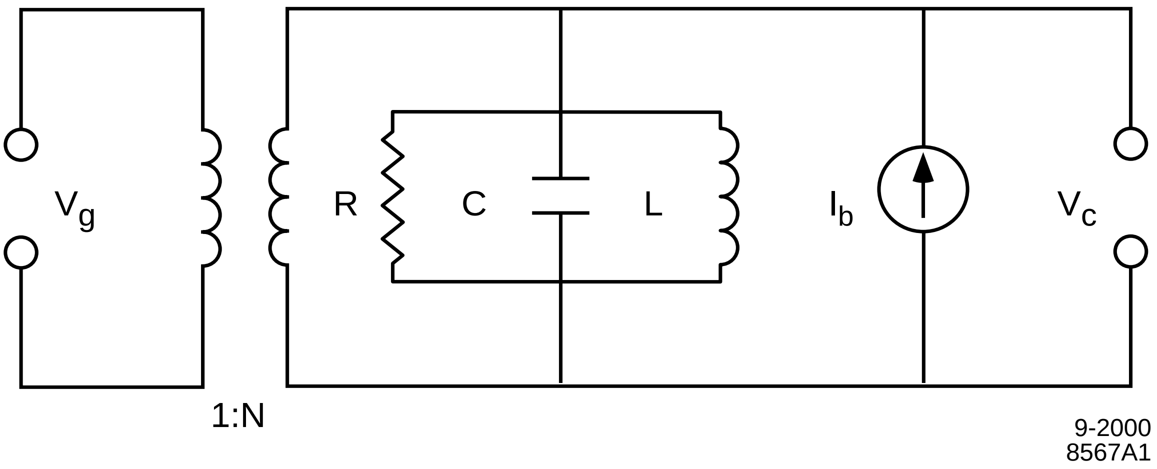

Figure 4.5: Circuit equivalent for beam interaction with a single cavity with a waveguide output.

where the beam-coupling parameter “R-over Q” is defined according to

$$\left[\frac{R}{Q}\right] = \frac{\left|\tilde{V}_c\right|^2}{\omega_0 U}, \tag{4.5}$$

in terms of stored energy U and resonance angular frequency ω_0. The tuning angle ψ is defined in terms of the loaded quality factor, Q_L, and the drive angular frequency ω, as usual

$$\tan\psi = Q_L \left(\frac{\omega_0}{\omega} - \frac{\omega}{\omega_0}\right). \tag{4.6}$$

Power radiated by the cavity into the guide may then be determined according to

$$P_{out} = \frac{\left|\tilde{V}_c\right|^2}{Q_e\left[R/Q\right]}, \tag{4.7}$$

where Q_e is the external quality factor. From this one may show, for example, that a 10% reduction in power corresponds to a tuning angle of $\tan\psi = 1/3$, or cell detuning of $\delta\omega/\omega \approx 1/6Q_L$. For a loaded quality factor $Q_L \approx 415$, this is a detuning of 0.04% or 37 MHz. This translates to 1 μm tolerances in machining and we will show in Ch. 5 that a de-tuning can also be caused by network elements with large reflections (VSWR $\gg$ 1).

4.3.2 Fabrication and Assembly

The completed geometry is indicated in Fig. 4.6. We describe next how this geometry was accomplished, with a set of four nominally identical cavities.

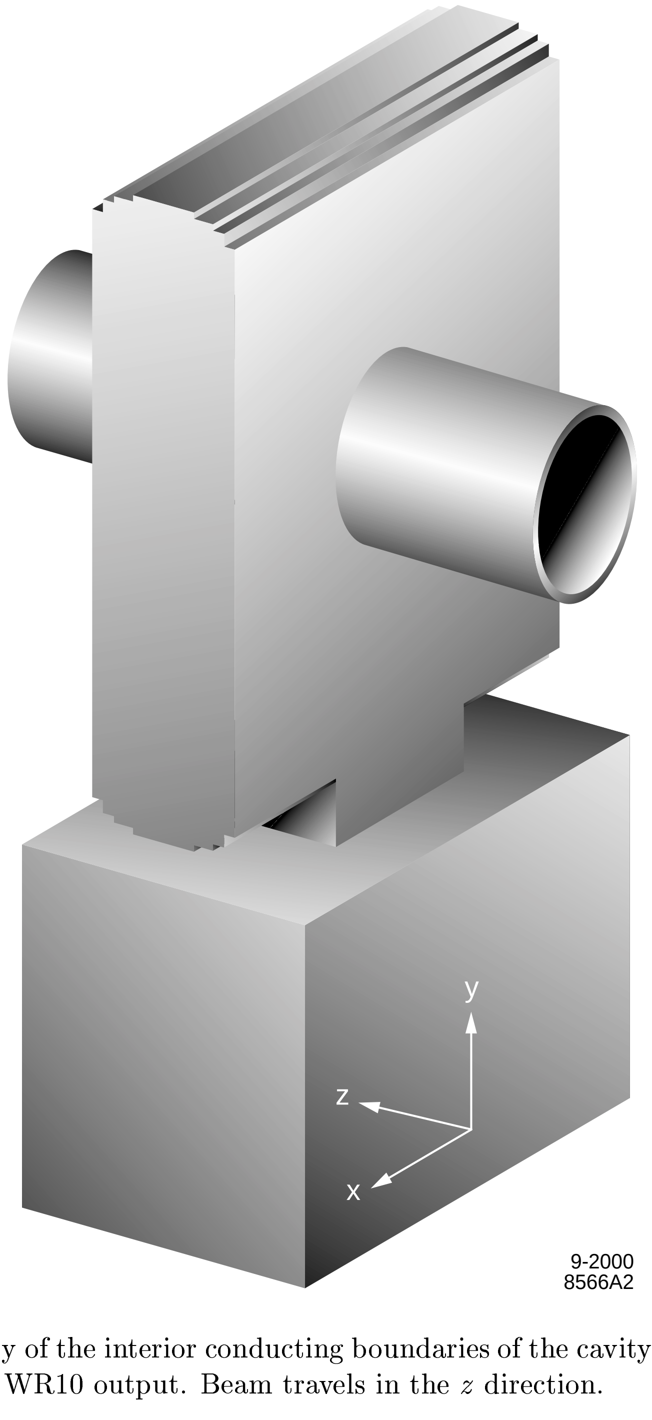

Figure 4.6: Geometry of the interior conducting boundaries of the cavity, including coupling iris, beam-tube and WR10 output. Beam travels in the z direction.

The oxygen-free electronic grade (OFE) copper cavity consists of three layers: a 2.44-mm thick plate with the cavity wire-EDM'd and two featureless plates comprising the cavity top and bottom. (The orientation of the cavity "top" is at positive x in Fig. 4.6 and bottom is at negative x.) The three layers were diffusion bonded together employing a 1024°C heat cycle at 25 psi for 10 minutes. The input waveguide coupling iris was then cut using sinker EDM. Ultrasonic acetone rinse had no measurable effect on wall quality factor, and the cavity was subjected to chemical cleaning. This raised the wall Q (prior to cutting of the beam tube) from 1029 to 1252.

To facilitate connecting waveguide, a threaded bolt circle conforming to WR10 0.75" flange was machined into the waveguide opening for each cavity. The width ("a" dimension) of the waveguide openings were intended to match the 0.1" wide dimension of WR10 guide, but were accidentally machined 0.1 mm narrower, resulting in a step on each side of the connecting waveguide. Analysis via *GdfidL* indicated that this would have negligible effect on the measurements.

To cut the beam-tubes, we used sinker EDM for the first, rough cut of the cavity. We then made a final cut of the 340 μm radius using wire EDM. To remove any debris created by the EDM process on the surfaces of the cavity walls, we etched the cavity by pumping an acid solution through the coupling port of the cavity. As mentioned, the acid solution can preferentially etch corners and features such as irises as we discovered during bench measurements in the next section.

4.3.3 VNA Measurements

To determine the state of the cavity, and as an aid in tuning, we again employed the VNA, permitting measurement of the steady-state complex reflection coefficient S_{11} over a range of angular frequencies ω. This may be compared with the theoretical result for single-mode excitation of a resonator from Eq. (3.31),

$$S_{11} = \frac{2\beta}{1+\beta} \cos\psi \, e^{j\psi} - 1. \tag{4.8}$$

where the coupling parameter $\beta = Q_w/Q_e$ is the ratio of wall quality factor to external (or "diffractive") quality factor. In this way have assessed the tune, and Q_e, Q_w, and β, as listed in Table 4.4.

Also seen in Table 4.4 are the analytic results for a closed pill-box, and the numerical (GdfidL) results for the cavity with beam ports. For the analytic comparison, we employed a rectangular pill-box of interior transverse dimensions $a \times b \approx 2.30$ mm$\times$2.44 mm and transit length $L \approx 0.50$ mm. The corresponding resonant angular frequency is given by $\omega_0 = kc$, where

$$k = \sqrt{\frac{\pi^2}{a^2} + \frac{\pi^2}{b^2}}, \tag{4.9}$$

with $c \approx 2.9979 \times 10^8$ m/s the speed of light. This gives a frequency of 89.6 GHz; accounting for the volume change due to the fillets from an 8-mil diameter EDM wire (about 0.8%), we calculate the resonant frequency to be 90.1 GHz. The measured frequency of the four cavities varied between 90.1 and 90.8 GHz, variation attributable to wire machining errors. Theoretical wall quality factor for the closed rectangular pill-box geometry may be expressed as

$$\frac{1}{Q_w} = 2\frac{R_s}{Z_0}\frac{1}{kL}\left\{1 + \frac{2\pi^2 L}{k^2}\left(\frac{1}{a^3} + \frac{1}{b^3}\right)\right\}, \tag{4.10}$$

with $Z_0 \approx 377\Omega$ the impedance of free-space, and $R_s \approx 79$ mΩ the theoretical surface resistance of a smooth OFE copper surface at the operating frequency. This corresponds to wall quality factor of 1570.

The external quality factor, Q_e, may be calculated by two methods. One is a simple estimation from power transmission between two waveguides, through a coupling iris, obtained from HFSS[1] simulation. In this geometry, the external Q is given by

$$Q_e = \frac{4\pi}{|S_{21}|^2}. \tag{4.11}$$

With a rectangular iris of width 0.83 mm, height 0.5 mm and thickness 0.25 mm, we find $Q_e = 1400$. A second method utilizes the frequency domain result of the closed cavity-waveguide system to find the complex resonant frequency of the waveguide loaded cavity

---

[1] A product of ANSOFT, Corp.

Table 4.4: Measured and theoretical parameters for the single cell cavity with and without beam port.

	No Port	Beam Port
Q_w (analytic)	1574	—
Q_w (simulation)	1533	1540
Q_w (measured)	1252	1305
Q_e (simulation)	1400/1370	583
Q_e (measured)	1048	571
β	1.19	2.29
$[R/Q]$ (simulation)	134 Ω	110 Ω

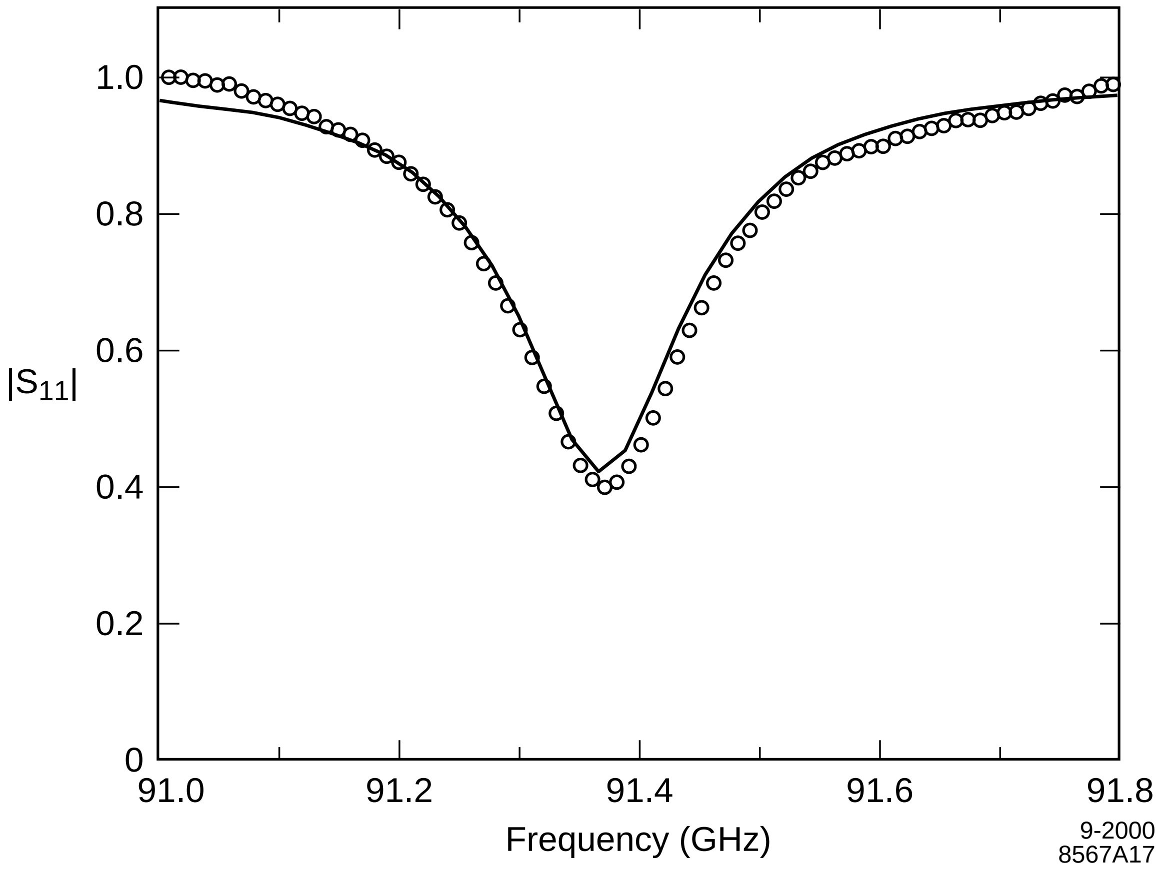

Figure 4.7: Reflection coefficient versus frequency, from measurement, and numerical simulation.

[26]. This gives a Q_e of 1370 with no beam port. These dimensions correspond to the geometry prior to cutting of the beam tube and the second acid rinse.

The finished assembly, with beam port, had a wider iris opening, of 0.92 mm caused by chemical polishing of the cavity. For this aperture the frequency-domain approach gives $Q_e \approx 583$, lowered due to the resulting stronger external coupling. The sensitivity of Q_e to the coupling iris width is noteworthy. A 20-μm wider iris lowers the Q_e by 200, while a 20-μm thinner iris reduces Q_e by 170.

The result for the scattering parameter S_{11} is indicated in Fig. 4.7, overlaid with the result computed with the time-domain module of the code *GdfidL* [29]. The simulation employs a damping decrement based on the theoretical wall quality factor $Q_w \approx 1540$. The complex S_{11} is seen in Smith chart form in Fig. 4.8. There one can also observe the effect of the chemical cleaning in decreasing the external quality factor. The original iris width

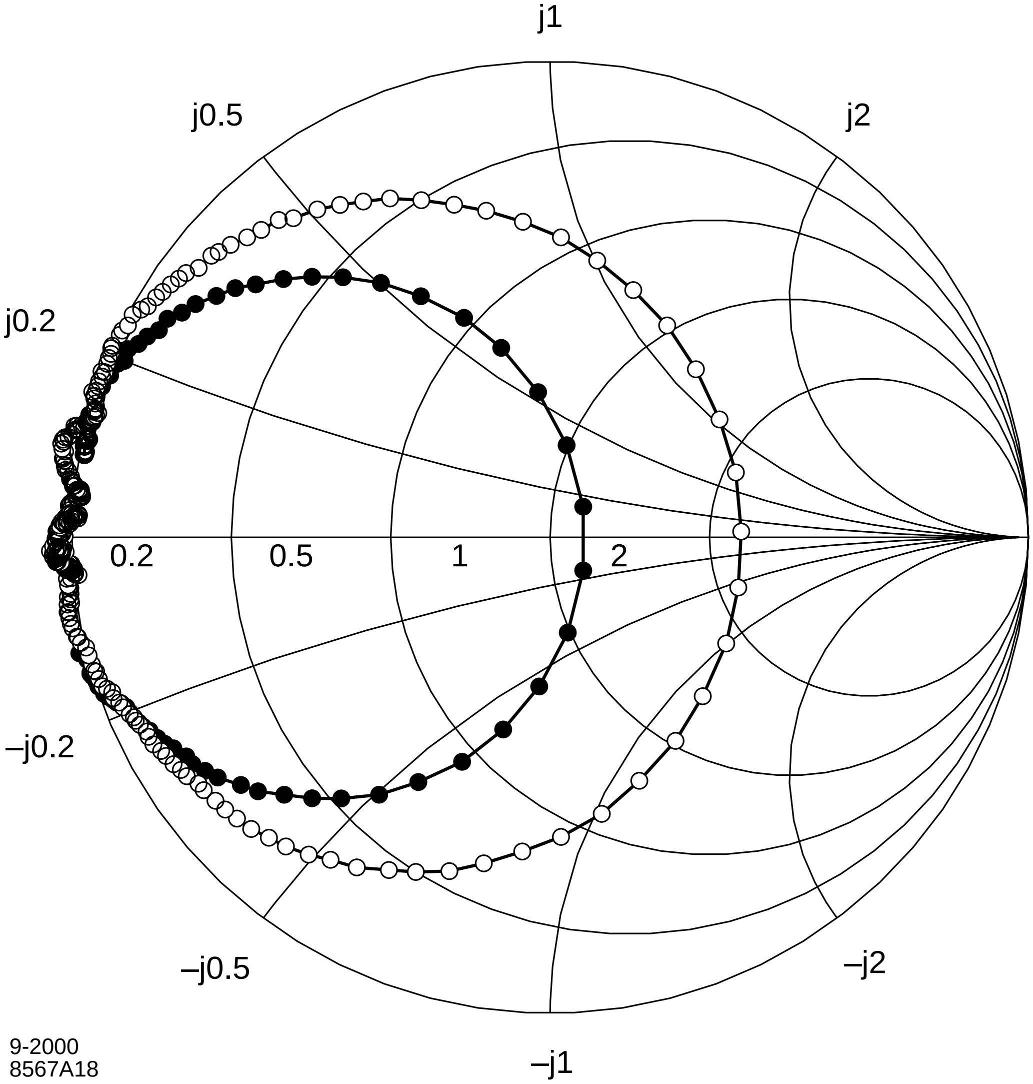

Figure 4.8: Smith chart of S_{11} for the case of no beam port (solid) and with a 680 μm beam port (open). For both cases, we see that the cavity is over-coupled.

was 0.87 mm, and this was widened to 0.92 mm in the course of chemical cleaning.

4.3.4 Bead Pull

We may infer the electric field profile by means of a bead-pull by combining Eq. (4.8) with Slater's theorem [27] that states the fractional change in frequency is proportional to the fractional change in stored energy which in turn is proportional to the square

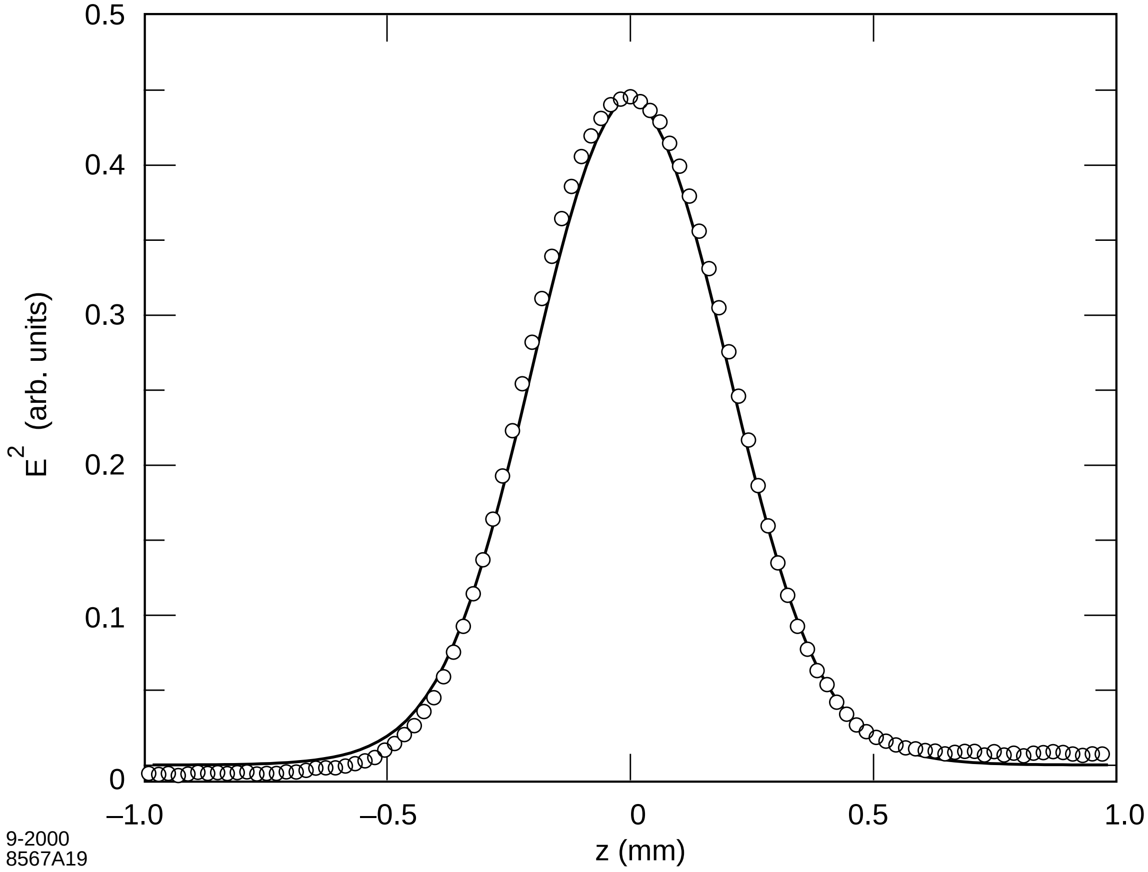

Figure 4.9: Result for inferred axial electric field E_z from bead-pull measurement, overlaid with theory.

of the field times the polarizability of the perturbation

$$\frac{\Delta\omega}{\omega_0} = \frac{\Delta U}{U_0} = \frac{1}{4U_0}\left(\epsilon\alpha_e E^2 - \mu\alpha_m H^2\right) \tag{4.12}$$

where E and H are the unperturbed field values and α_e and α_m are the electric and magnetic polarizabilities of the perturbing object. A bead pull was also performed, with the measurement seen in Fig. 4.9, overlaid with the result computed with the frequency-domain module of the code *GdfidL*. The perturbation was a dielectric bead formed by tying a knot in a length of 30 μm diameter tulle of nylon fiber.

The field profile data seen in Fig. 4.9 permit one to go on to infer peak electric field from cavity voltage, with the result $V_c/E_{pk} \approx .614$ mm. Using Eq. (4.7) one may then infer peak accelerating field from the power radiated. With $[R/Q] \approx 110\ \Omega$ from numerical simulation (*GdfidL*), and $Q_e \approx 571$ from measurement, a figure of $P_{out} \approx$1 kW corresponds

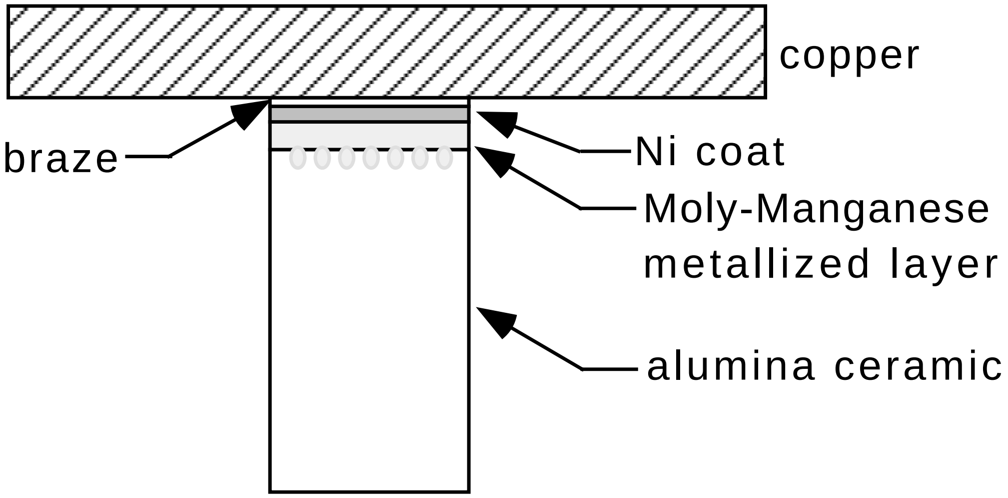

Figure 4.10: Window coatings.

to a cavity voltage of 7.9 kV, and a peak field of $E_{pk} \approx 12.9$ MV/m. Peak surface field is seen from *GdfidL* simulation to be a factor of 2 higher than the peak longitudinal field, namely 26 MV/m.

Power levels in a beam-driven experiment are facilitated by an RF window allowing signals to be read with a commercial RF mixer.

4.4 RF Window

Tests of W-band structures (e.g. the cavity from the previous section) powered with beam require the use of RF circuitry outside the beamline vacuum. We have developed RF windows to allow the interface of the vacuum and non-vacuum components.

Preliminary considerations for the design of the window were: VSWR<1.1, vacuum integrity, and vacuum compatibility. We wished to pump the window assembly down below 10^{-8} torr, and handle 100mW average power, 10 kW peak power. Typically, failure of windows are caused by breakdown, multipactor, fracture, puncture, etc. We did not expect to contend with these issues, however we realized that such phenomena are part of the experiment, and part of the utility of the apparatus in the first place.

As to window fabrication, alumina ceramic was chosen due to familiarity with its use at X-band. Experimental measurements implied a dielectric constant for alumina ceramic at 91.4 GHz of 9.5. The usual window fabrication procedure at X-band, and the one we pursued, was to have an alumina disk ground with a diamond tool to the requisite dimensions. The edges to be bonded are metalized with 1 mil of a Moly-Manganese paste (80% moly). The MgO penetrates the ceramic, forming a glassy matrix. On the exterior surface, the MgO bonds to the Moly powder. The outer surface is coated with a thin layer of Nickel, to inhibit oxidation. The result is then brazed to copper. The picture is that of Fig. 4.10. Copper has twice the temperature coefficient of expansion of the alumina ceramic (10^{-5} versus 2×10^{-5} for copper). Thus some measure must be taken to insure that the joint remains tight during brazing. A jig was bound with molybdenum wire to constrict the copper around the ceramic.

A number of papers on high-power windows can be found, particularly sintered alumina ceramic (Coors AD-99.5). TiN coating of 60 Å on either side permits charge to bleed off. Impurities (such as MgO of the sintering binder), micro-dust, micro-voids and the like can be correlated with window failure (fracture or puncture). Of the samples presented by, for example, Matsumoto, those with 99.9% purity (MgO at the 0% to 0.06% level) did not fail, up to 300 MW at X-band. In windows studied, where temperature did not rise above 10°C, the window did not fail. For our work, a window temperature monitor was considered; however our average power is low (duty cycle 10^{-6}) and it was decided not to be practical.

For reasons of simplicity, and expediency, we pursued a window assembly as depicted in Fig. 4.11. Let us review briefly the considerations for such a window. Table 4.5 shows a comparison of fields inside WR10 and WR90 for different power levels. In terms of peak field, studies at 100 kW in WR10 correspond to 10 MW studies at X-band in WR90.

Table 4.5: Field levels in WR10 and WR90.

E(MV/m)	P(W) - WR10
0.8	1.00E+03
2.5	1.00E+04
7.8	1.00E+05
24.7	1.00E+06

E(MV/m)	P(W) - WR90
0.9	1.00E+05
2.8	1.00E+06
8.9	1.00E+07
28.1	1.00E+08

As to the problem of matching for this window-like geometry, we may view it as transmission line (WR10, vacuum), joined to another transmission line (WR10, dielectric), and a third (WR10, vacuum). That is to say, we may consider the case of dielectric-filled waveguide dimension the same as WR10. We match fields at the boundaries according to conditions on voltages (transverse electric field),

To illustrate let us consider some particulars for WR10 at 91.392 GHz, and a dielectric constant of 9.5. In vacuum WR10 at this frequency we have a guide wavelength of 0.4296 cm or 169.13 mil. Characteristic impedance is 493.34 Ω. In the dielectric guide, with the same a dimension, we have a guide wavelength of 0.108841 cm, or 42.85 mil. Characteristic impedance is 124.99 Ω. Thus normalized impedance is 0.2534. Possible window thicknesses corresponding to different N values are:

N	L (cm)	L (mil)	
0	0.05442	21.43	1/2 λ window
1	0.10884	42.86	2/2 λ window
2	0.16326	64.28	3/2 λ window

The thinnest windows made are typically 31 mil or so, thus the $N = 0$ (single half-wavelength window) case is too thin. An $N = 1$ or 2 window appears more practical, and we settled on a 1-λ window.

For a 1-λ window one needs a block of ceramic with dimensions (modulo metallizing, coating, brazing) 42.85 mil × 100.00 mil × 50.00 mil. Our estimate of ε was somewhat uncertain, and a table for the 1-λ window serves to illustrate the sensitivity:

$\varepsilon/\varepsilon_0$	9.0	9.5	9.7	10.0	10.5	11.0
L(mil)	44.08	42.85	42.39	41.72	40.67	39.7

Final design settled on was conceptually WR10 waveguide, operated in fundamental TE_{10}-mode, and a slab of dielectric filling a length of the guide. Wave transmission through a length L of lossless dielectric is described by

$$|S_{21}|^2 = \left[\cos^2 k'_z L + \frac{1}{4}\left(\frac{k_z}{k'_z} + \frac{k'_z}{k_z}\right)^2 \sin^2 k'_z L\right]^{-1} \tag{4.13}$$

where k_z and k'_z are the guide wavenumbers in the vacuum and dielectric portions of the guide,

$$k_z = \frac{2\pi}{\lambda}\sqrt{\mu_r \varepsilon_r - \left(\frac{\lambda}{2a}\right)^2}, \tag{4.14}$$

λ is the free-space wavelength, a is the waveguide width (0.10"), and μ_r and ε_r are the relative permeability and permittivity of the dielectric. For a good match, the window length should be a multiple of half the dielectric guide wavelength, or $k'_z L = n\pi$, with n an integer. In addition, Eq. (4.13) implies that highest bandwidth is attained with the shortest

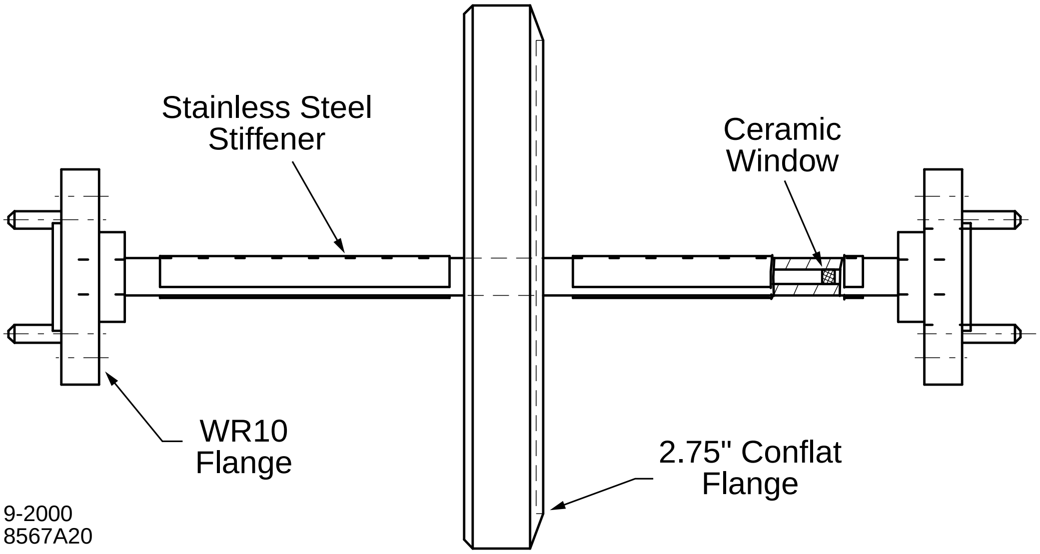

Figure 4.11: Mechanical drawing of the first W-band RF window with WR10 and Conflat flange.

window length. We selected an $n = 2$ or "1-λ" window design as a compromise between bandwidth and ease of assembly.

As to assembly, the 0.100"×0.050" oxygen-free high-conductivity (OFE) copper WR10 rectangular waveguide is obtained without flanges from commercial extruded stock and chemically cleaned. The dielectric consists of Wesgo AL-995 alumina ceramic, sliced and ground from a 3" disk, into rods of dimension .098"×.048"×2". The rods are coated with a 1-mil layer of molybdenum-manganese and fired at 1500°C forming a metallized layer for brazing. The windows are then cut to their final length of .0428" and brazed into the OFE waveguide. The waveguide flanges are attached in a separate step. They consist of 304L stainless steel, machined to a 3/4" circular WR10 waveguide flange geometry. These are attached with a second, lower-temperature braze. Figure 4.11 shows a mechanical drawing of the window and vacuum flange. We kept the vacuum flange separate from the RF flange to ease the design of the window. The window is made in two braze steps. Thus the braze steps consisted first of the window braze into the waveguide, then the window and waveguide assembly is brazed into the vacuum flange. After each braze step, the window is leak-checked with helium to ensure vacuum integrity.

One concern with this process is the difference in the thermal expansion coefficient of the ceramic ($10^{-5}/°\mathrm{C}$) and the copper waveguide ($2\times10^{-5}/°\mathrm{C}$). Differential expansion

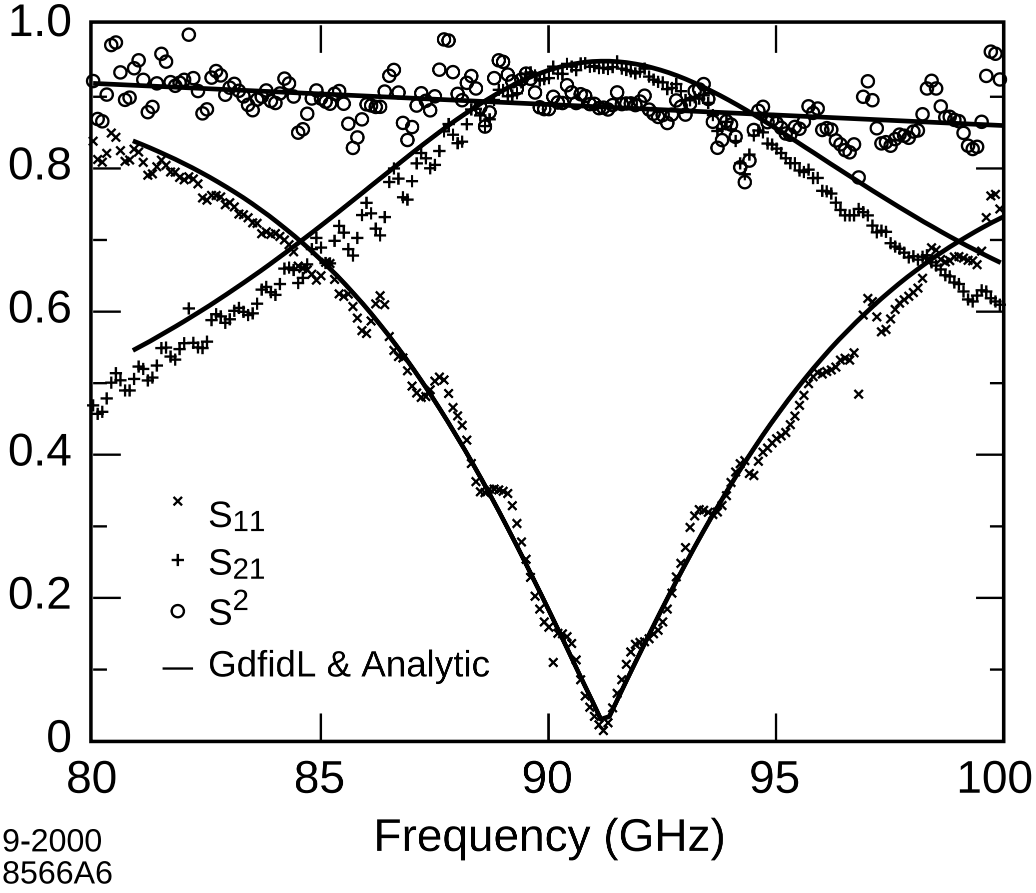

Figure 4.12: Plot of measured scattering parameters, S_{11} and S_{21} along with calculated scattering parameters for a sample window. $S^2 = S_{11}^2 + S_{21}^2$.

during the 1000°C braze cycle may in principle produce a gap as large as 1 mil between the dielectric and copper surfaces. For lower frequency, larger-dimension window assemblies, such differential expansion may be restrained by a molybdenum retaining wire encircling the ceramic window assembly. We opted for the same method for the W-band assembly, producing successful brazes with all passing leak-check.

The completed window-assembly was subjected to transmission and reflection measurements using the VNA. The results seen in Fig. 4.12, were fit with the analytic result of Eq. (4.13), employing ε_r as a fit parameter. We infer $\varepsilon_r \approx 9.485 \pm .03$ at 91.4 GHz. Also seen in Fig. 4.12 is the result of numerical simulation via the finite-difference code, *GdfidL* [29], giving good agreement.

One additional concern in this geometry is the presence of higher modes, "ghost modes", caused by coupling into a mode that is trapped inside the over-moded dielectric guide. One is particularly concerned to avoid a spurious resonance in the operating band and the added insertion loss that would result. Fig. 4.12 shows the power sum $|S_{11}|^2+|S_{21}|^2$, from which we can determine the insertion loss, and inspect the operating band for ghost-modes. The observed attenuation of 0.2 dB seen in Fig. 4.12 is consistent with loss through the 3" copper waveguide. The length of ceramic was too short for results to be sensitive to a loss tangent in the 10^{-4} range.

After bench measurements, this window was employed in a series of tests to be described in Ch. 5. The maximum power handled by the window was 4 kW corresponding to a field level of 1.5 MV/m for a pulse length of 100 ns. The window was an essential component for this test as the solid-state components needed for power detection are not vacuum compatible, and, in any case, are most conveniently situated outside the vacuum envelope.

The design and the process appear to be mechanically sound, and robust; following the first working window, several additional windows have been fabricated, and their RF characteristics are in close agreement with the foregoing, while they have all passed leak check.

In summary, we have developed vacuum-compatible components in WR10, for operation with a miniature accelerator. Alternatives to a window included coaxial feed-through, horn output through a window, taper to oversize guide and window. However, all of these techniques have their own challenges, and even if successful, leave one with a more complicated power calibration. More than that, they are not ideally suited for accelerator component development. With a WR10 window we are able to couple power to other WR10 components in a straightforward way. We expect that development of more sophisticated, *quasi-optical* accelerator components will later benefit from the calibrations and other work facilitated by this simple, yet robust window design.

4.5 Dielectric Structure

The essential component for building a W-band accelerator is the accelerator structure. We have developed a dielectric loaded waveguide structure for this purpose. Revisiting Ch. 3 and Fig. 3.1, two smooth dielectric slabs form a transmission line designed with a cross section to give a phase velocity equal to the speed of light. The ends of the transmission line are coupled to WR10 waveguide through a coupling cavity designed to match to a traveling wave at 91.392 GHz. In practice this match was found empirically by cut and measure. "Measure twice, cut once" was not a viable option because of a lack of measurement equipment (*i.e.* an optical inspection station) for determining the dimensions scales required.

In this section we describe the design considerations, fabrication and bench-test of the planar dielectric accelerator. Our criteria for choice of dielectric were vacuum compatibility, breakdown threshold, moderate permittivity ($\varepsilon_r < 10$) for reasonable group velocity (giving reasonable machining tolerances), and low loss-tangent. We pursued the use of two materials: alumina ceramic and carbon vapor deposition (CVD) diamond, with relative permittivities at W-band of 9.5 and 5.5, respectively. Diamond is of great interest [30] for high-gradient work, where heating and breakdown are concerns.

4.5.1 Design and Tolerances

In general, design of an accelerator structure proceeds from an optimization of

$$\frac{1}{L}\left[\frac{R}{Q}\right] = \frac{G^2 v_g}{\omega P} \tag{4.15}$$

and while the example of Sec. 3.1 is useful as a guide, it is possible to be more precise with the help of a finite difference electromagnetics code *GdfidL* [29]. For illustration, we present two structure designs using alumina ceramic and diamond. Dimensions were chosen compromising between high $[R/Q]$ and adequate beam aperture, subject to synchronism at the design frequency. With the aid of *GdfidL*, we arrived at the geometrical parameters for the structures listed in Table 4.6. This table summarizes design parameters for an alumina structure (column 1); its slab counterpart (column 2) is obtained holding b/a constant. Similarly, diamond and its slab counterpart are listed in columns 3 and 4.

An infinite length structure is modeled numerically by one with finite length having periodic boundary conditions. The numerically computed Q resulting from sidewall copper and dielectric loss in this finite length structure may then be employed to determine the attenuation length in the traveling wave structure by the relation

$$\alpha = \frac{\omega}{2Q v_g}. \tag{4.16}$$

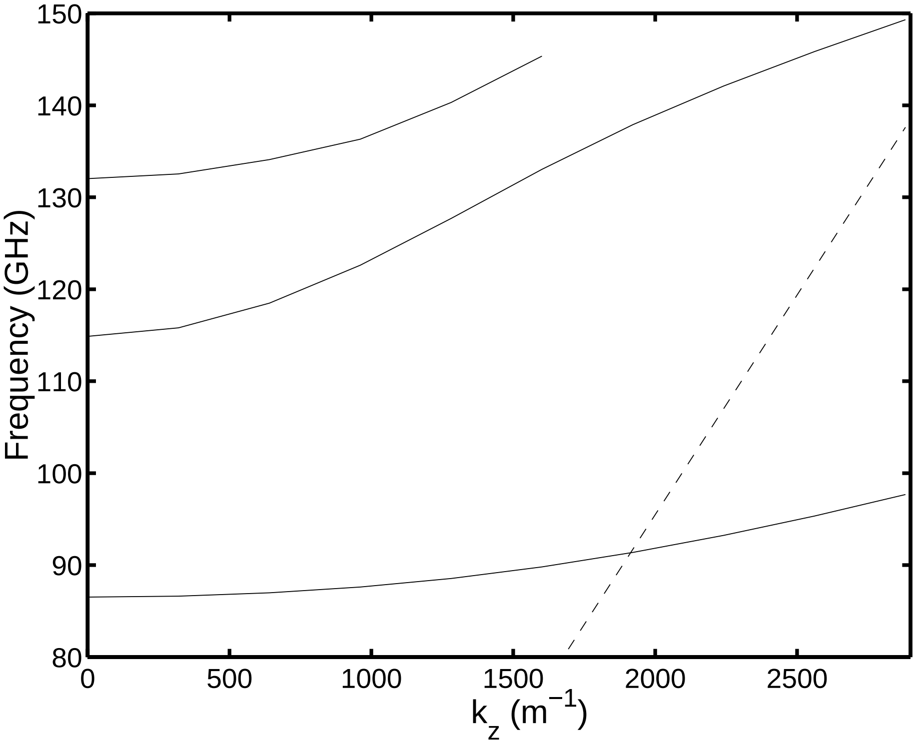

Figure 4.13: The dispersion diagram for the lowest monopole modes for the alumina ceramic structure and the speed of light line $v = c$ (dashed).

The field-solver also provides the dispersion characteristics of the various structure modes. For illustration, dispersion curves for the monopole modes of the alumina structure (column 1, Table 4.6) are illustrated in Fig. 4.13. The accelerating mode corresponds to the curve labelled HEM$_{11}$ in Fig. 4.13, and the operating frequency is indicated by a circle. The wave number at the operating frequency is $k_z = \omega_0/c$.

As in a conventional structure, synchronism imposes tolerances on the geometry. The sensitivities to dielectric thickness ($d = b - a$), width (w), and gap distance ($2a$) are listed in Table 4.7 for two sample structures. Conversely the coefficients of Table 4.7 permit correction of uniform errors of the geometry by adjustment of the gap distance ($2a$), albeit with some compromise in $[R/Q]$ or beam aperture.

Such tuning errors cause a deviation of phase velocity from c that results in particle phase slippage from the RF phase. A *uniform* deviation of Δk_z from the speed of light line will result in a linear phase slip

$$\delta\phi(z) = \Delta k_z z. \tag{4.17}$$

The result is a reduction in the voltage gain experienced by a particle traversing the structure,

$$\frac{V}{V_0} = \frac{1}{l}\left|\int_{-l/2}^{l/2} e^{j\delta\phi(z)}dz\right| = \text{sinc}\left(\frac{\Delta k_z l}{2}\right), \tag{4.18}$$

where V_0 is the voltage gain absent errors. It follows that allowance of 10% voltage reduction in a structure with $l \approx 2.54$ cm requires $|\Delta k_z/k_z| < 3\%$. Presently, we show that we were able to tune the structure well within this limit.

Another kind of error of potential concern, corresponds to a *linear taper* in w or d. This kind of error cannot be tuned away, in contrast to the previous *uniform* error.

Table 4.6: Geometrical parameters for example structures, with resonance at 91.4 GHz.

	GdfidL	Slab	*GdfidL*	Slab
ε_r	9.5	9.5	5.5	5.5
a (μm)	360	300	272	230
b (μm)	650	550	680	575
W (μm)	800	—	1360	—
v_g/c	0.1	0.1	0.2	0.2
$[R/Q]$ $\left(\frac{k\Omega}{m}\right)$	90	—	94	—
α (m^{-1})	6.4	6.8	2.2	3.0
Q	1500	1400	2200	1600
E_y/G	0.6	0.6	0.7	0.5

Considering $w = w_0 + \theta_w z$ where θ_w is the taper angle, the phase velocity corresponds to axial wavenumber

$$k_z(z) = k_z(0) + \frac{\delta k_z}{\delta w}\theta_w z. \tag{4.19}$$

The phase slip $\delta\phi$ is found by integrating the phase velocity along the length

$$\delta\phi(z) = \frac{1}{2}\frac{\delta k_z}{\delta w}\theta_w z^2. \tag{4.20}$$

A calculation like that of Eq. (4.18) gives

$$\frac{V}{V_0} = \frac{|C(\zeta) + iS(\zeta)|}{\zeta}, \tag{4.21}$$

$$\zeta = \frac{l}{2}\sqrt{\frac{\theta_w}{\pi}\frac{\delta k_z}{\delta w}} \tag{4.22}$$

where C and S are the Fresnel functions. For a 10% voltage reduction and $l \approx 2.54$ cm, the thickness (d) variation must be held to 13 μm from one end to the other. The width (w) taper must be less than 72 μm. These numbers represent at least a factor of 3 improvement (increase) in the tolerance over that for a conventional disk-loaded structure.

4.5.2 Fabrication and Cold-Test

The first step of the fabrication process was to machine the dielectric to the cross-section determined using *GdfidL*. The alumina was ground to its final dimension; the diamond was laser cut. The results were essentially 1" long "toothpicks" with cross-sections of 0.3×0.8 mm^2 for the alumina and 1.3×0.4 mm^2 for the diamond with tolerances in the range 5-10 μm.

The dielectric strips were aligned to the center of the flats using a precision machined fixture, and brazed to the copper substrate using an active braze alloy (ABA) from

Table 4.7: Phase sensitivity to dielectric thickness (d), width (w), and gap distance (a) for the structures described in Table 4.6. Units are m^{-1}/μm.

	Alumina	Diamond
$\frac{\delta k_z}{\delta d}$	34	15
$\frac{\delta k_z}{\delta w}$	3.2	1.3
$\frac{\delta k_z}{\delta a}$	2.9	2.5

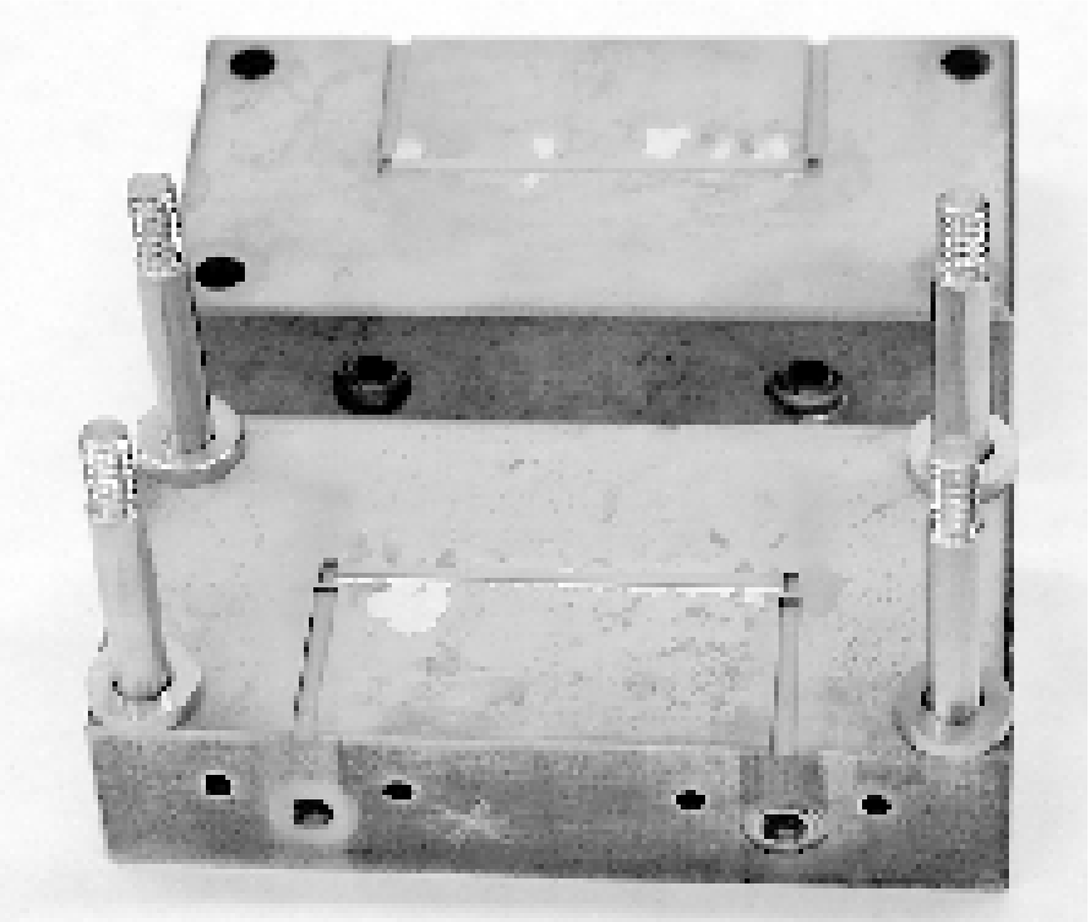

Figure 4.14: Picture of a planar dielectric accelerator structure made from two identical halves. The 1" long alumina strip is brazed to the center and located between the input and output waveguide and coupling cavities.

Wesgo, CuSilABA (78% Cu, 20%Ag, 2%Ti). In principle, differential expansion a concern at the 810°C braze temperature of the copper and alumina (diamond) with the expansion coefficients of $2\times10^{-5}/°C$ and $1\times10^{-5}/°C$ ($2\times10^{-6}/°C$) where at the end of the brazing process the ceramic is under compression. The induced stress in the copper and ceramic could cause a catastrophic failure such as the ceramic breaking or copper warping. Happily, we have not seen such failure.

After the dielectric was brazed, we cut the input and output waveguides and coupler cavities using stub EDM. Location of the cavity and dielectric centers were required to be within 5 μm. After a first cut of the cavities, photo seen in Fig. 4.14, we assessed the state of the structure employing the VNA. In this way we could determine the transmission

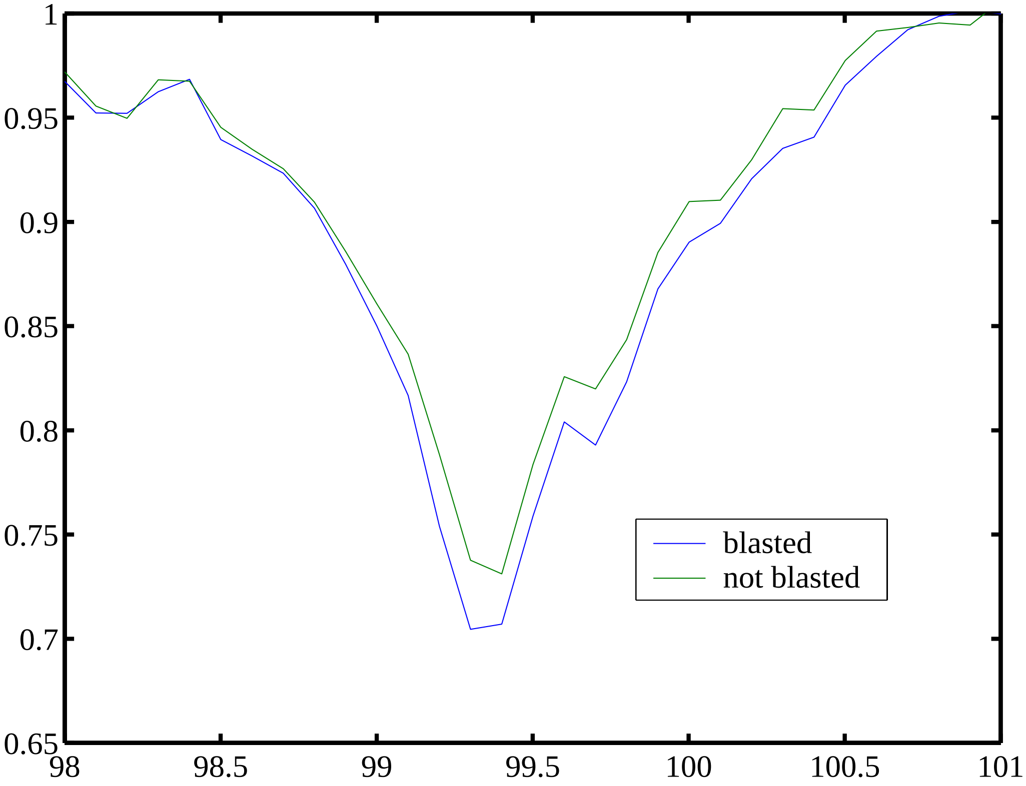

Figure 4.15: VNA data from sand-blasted cavity tests.

and reflection characteristics, and make comparison with Eq. (3.47), employing the external Q's, wall Q's, and the resonance frequencies.

Finding that wall quality factors were rather low in previous EDM cavity studies, we performed a stub EDM test-cut of additional stand-alone coupling cavities to measure the quality of the cut structures. We found that the wall Q of the cavity could be improved by "sand blasting" the tufaceous cavity surface with 10 μm alumina ceramic powder. We saw a 20% improvement in wall Q and no appreciable change in external Q or resonance frequency.

In this way, after three iterations of cutting and measurement, we had cut the coupler cavities to proper frequency and coupling, and arrived at a circuit characterized by the scattering matrix parameters depicted in Fig. 4.17 for the alumina example.

Using the circuit model discussed in Ch. 3, the modeled results shown in Fig. 4.16, and comparing with the data of Fig. 4.17, we inferred the circuit parameters listed in

Table 4.8. Independent measurement of the "sand-blasted" coupling cavities confirmed Q_{w_1} and Q_{e_1}.

4.5.3 Bead Pull

As discussed previously, the phase velocity of the structure must be maintained to within ±3%. The phase velocity was measured by means of a non-resonant bead pull, formalism set down by Steele [31] and with a result similar to Slater: the change in reflection coefficient is proportional to the square of the perturbed field taking the general form

$$\Delta S_{11} = \frac{i\omega}{2P} \left(\epsilon \alpha_e E^2 - \mu \alpha_m H^2 \right) e^{-2\gamma z} \tag{4.23}$$

where $\gamma = (ik_z + \alpha)$, P is the power and the polarizabilities of the needle are described by α_e and α_m. The field perturbation provided by a 100 μm diameter stainless steel hypodermic needle stretched transversely across the structure is soluable, however inference of the complex wave number is independent of α_e and α_m. The wavenumber, k_z, may be inferred from the phase of ΔS_{11}, shown in Fig. 4.18, for the alumina example. This structure was tuned by adjusting the gap distance ($2a$) to yield a phase velocity within 0.1% of the speed of light.

The attenuation length of the ceramic may be inferred from the amplitude of ΔS_{11} shown in Fig. 4.19, well fit by $1/\alpha = 73$ mm. These data may be compared with those listed in Table 4.6. While we cannot distinguish dielectric and copper loss by our measurements, our experience with copper waveguide of similar manufacture corresponds to an effective surface resistance 30% over that of an ideal smooth OFE copper surface. From this and our observed figure for attenuation, we may infer a loss-tangent of 1×10^{-3} for alumina, lying in the range of reported values $0.8 - 1.6 \times 10^{-3}$ at W-band.

In parallel with the alumina structure was a similar study of a diamond dielectric structure including design, fabrication and bench-test. The data for the diamond structure revealed that the diamond samples were of low quality, with a dielectric constant of 5.7 rather than 5.5 and a high loss tangent in the 10^{-2} range.

Table 4.8: Circuit model parameters describing the accelerator as a series of lumped elements for the alumina example with $L = 2.54$ cm.

$\omega_1/2\pi$	Q_{w_1}	Q_{e_1}	Q_{e_2}	$\omega_2/2\pi$	Q_{w_2}	Q_{e_3}	Q_{e_4}	α
91.4 GHz	1000	80	130	91.5 GHz	130	80	1000	14 m^{-1}

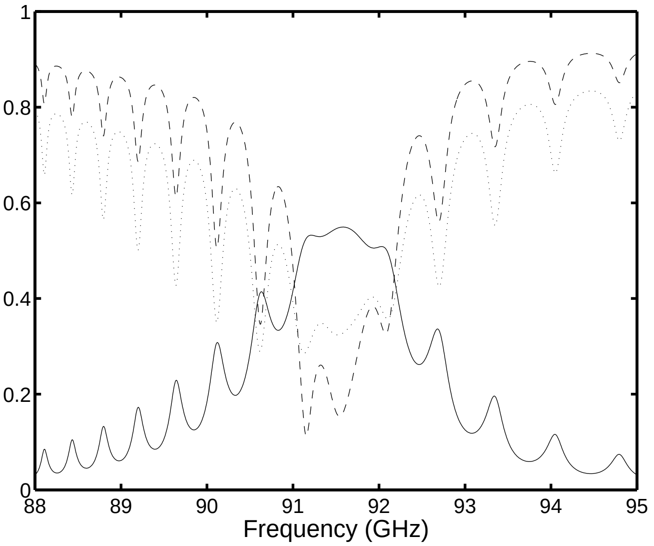

Figure 4.16: Scattering matrix elements S_{11} (dashed), S_{21} (solid) and the power sum $S^2 = S_{11}^2 + S_{21}^2$ (dotted) using the circuit model from Ch. 3 and circuit parameters listed in Table 4.8.

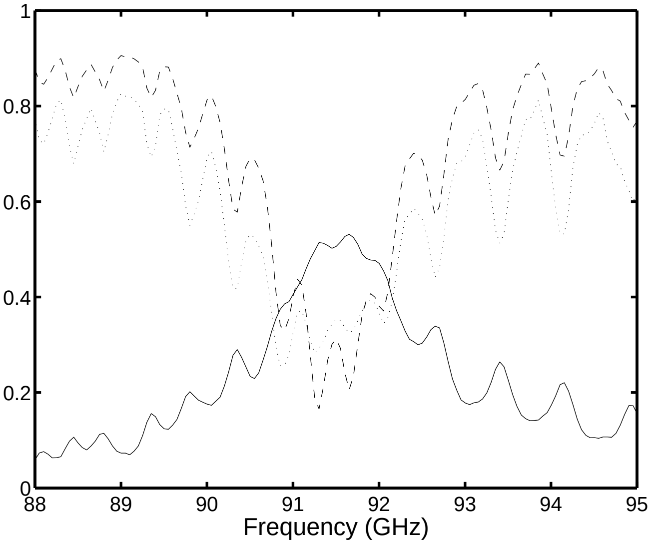

Figure 4.17: Transmission, S_{21} (solid), reflection, S_{22} (dashed), and power sum, $S_{21}^2 + S_{22}^2$ (dotted), measurements from a prototype alumina PDA structure, subsequently installed in the beamline.

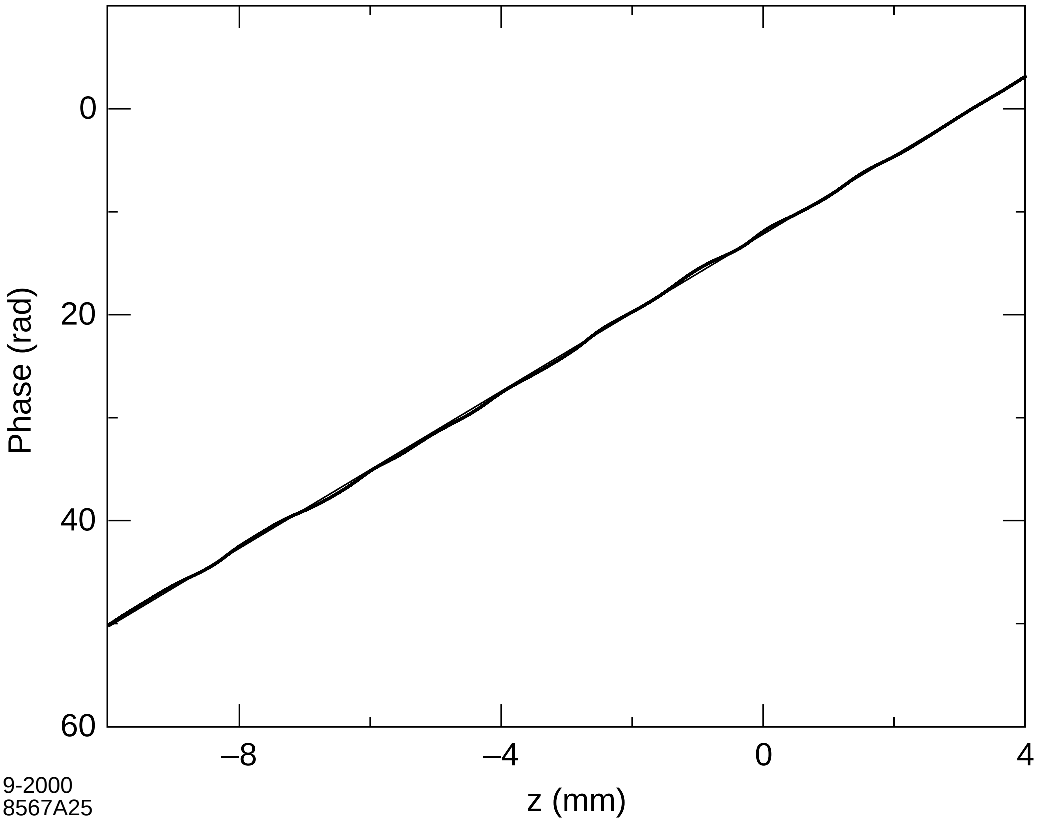

Figure 4.18: Phase of ΔS_{11} as measured from bead pull overlaid with the theoretical result, confirming $k_z = \omega/c$.

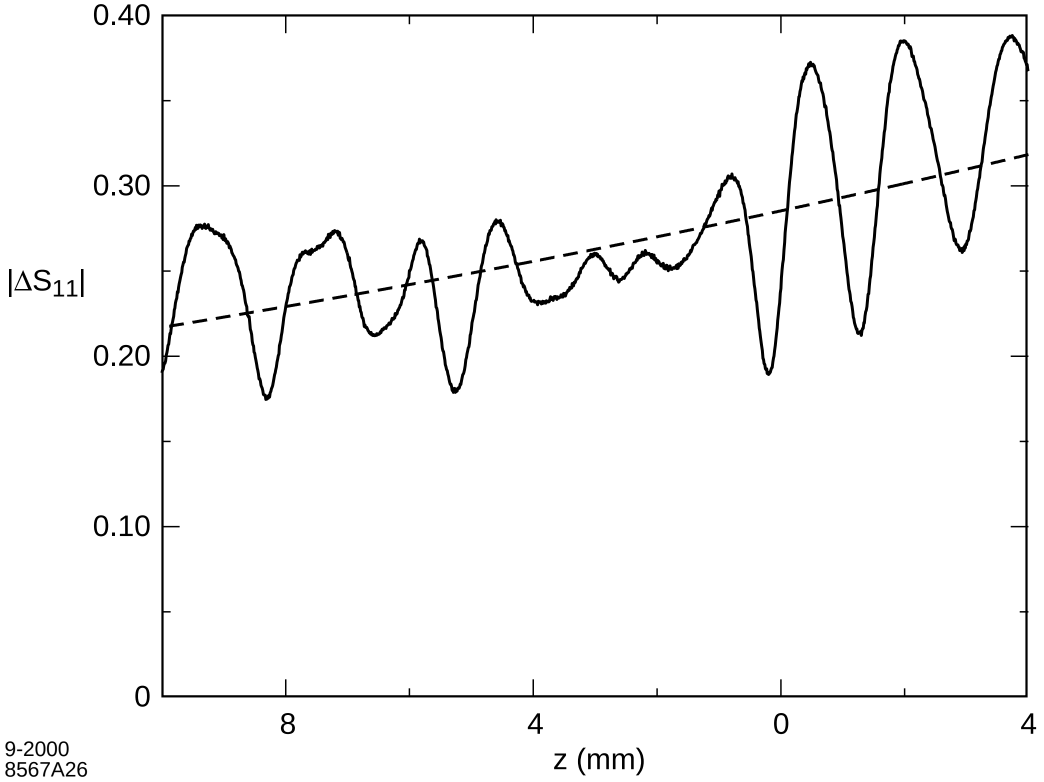

Figure 4.19: Attenuation length as measured from a bead pull, overlaid with the least-squares fit with decay length, $1/\alpha = 73$ mm.

4.5.4 Discussion

We have presented for the first time an assembled and bench-tested W-band dielectric accelerator. For some years discussion of mm-wave accelerator structures has centered on the difficulty of fabrication of miniature disk-loaded guide [32, 33]. Here we have seen that an alternative approach employing a smooth dielectric loaded guide is quite feasible. Clearly, assembly, cleaning, and fine-tuning on the bench are critical in arriving at accurately tuned input and output cavities, and high wall Q's. As for lower frequency accelerator work, fabrication goes hand-in-hand with rf measurements on the bench.

The last component necessary to complete the relativistic klystron circuit is the phase-shifter, described in Sec. 4.6.

4.6 Power Recirculation Phase Shifter

Recirculation in the form of Fig. 4.20 benefits from a phase-shifter, as the power developed in the circuit depends on the phase-length of the recirculator arm. Commercial components are not adequate for such work, where vacuum compatibility and high peak power are concerns. In this section, we describe the design, fabrication and bench test of a squeeze-type phase-shifter suitable for the circuit of Fig. 4.20(b).

When the recirculator is used with the dielectric structure, we should see an enhancement of the field levels according to

$$\frac{E(L)}{E_0(L)} = \frac{1}{1 - Ae^{-\tau}} \tag{4.24}$$

where A is the complex attenuation through the phase shifter. This variable phase "knob" allows for turning on and off beam deceleration, as well as fine tuning of the phase length to maximize power circulation. The calculated deceleration voltage versus phase shift ϕ is plotted in Fig. 4.21.

The squeeze type shifter we envision is that pictured in Fig. 4.22, consisting of a length of WR10 waveguide, with standard WR10 inner and outer dimensions (a=0.10", b=0.05" and A=0.18", B=0.13" outer), and single mode propagation in the range 59-118 GHz. The waveguide can be compressed in the wide (a) dimension to provide a phase-shift. The actual waveguide will be bent to form a U-shape, meanwhile, the phase length may be understood from the scaling for straight WR10. Changing the width of the wave-

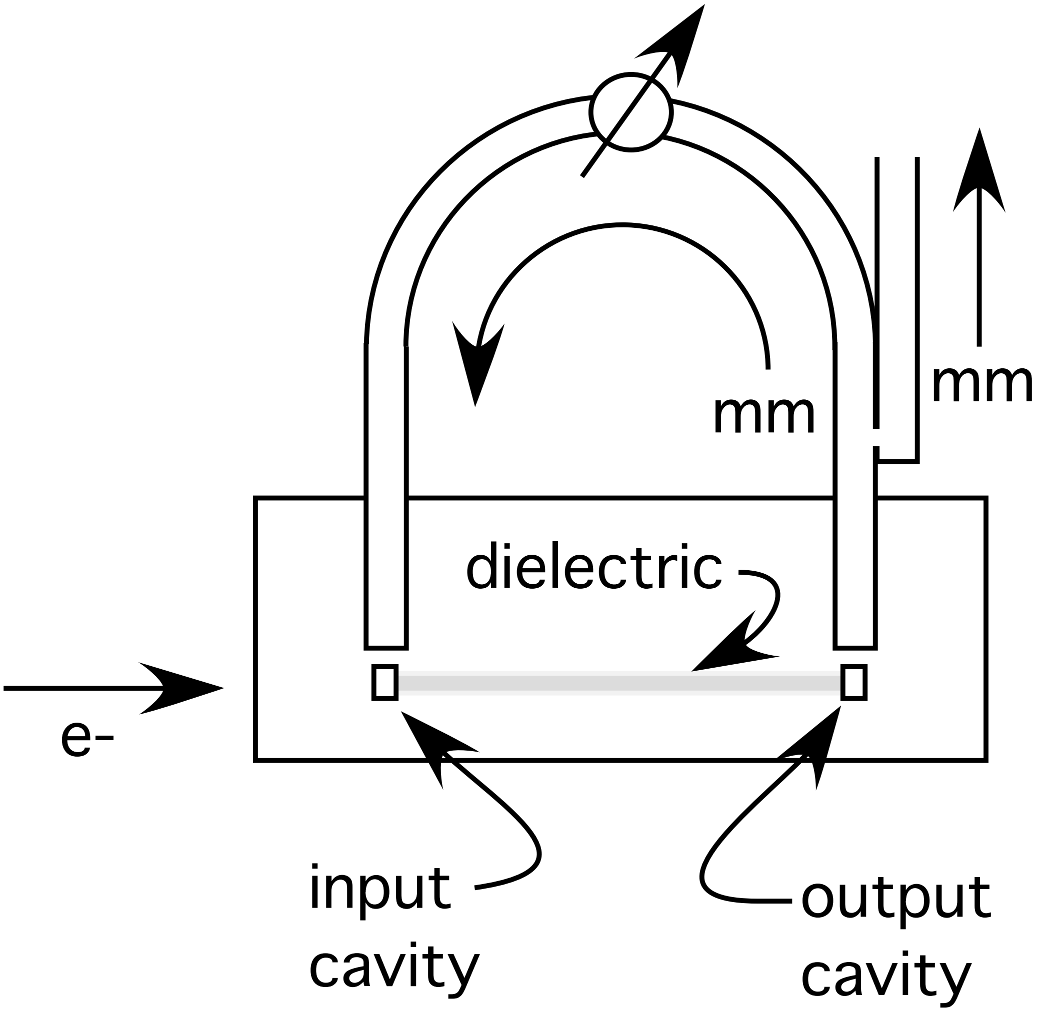

Figure 4.20: Cartoon illustration of field enhancement during mm-wave power generation by means of a recirculation arm transporting output power back to the input. The recirculator has a phase adjustment to maximize power flow through the structure.

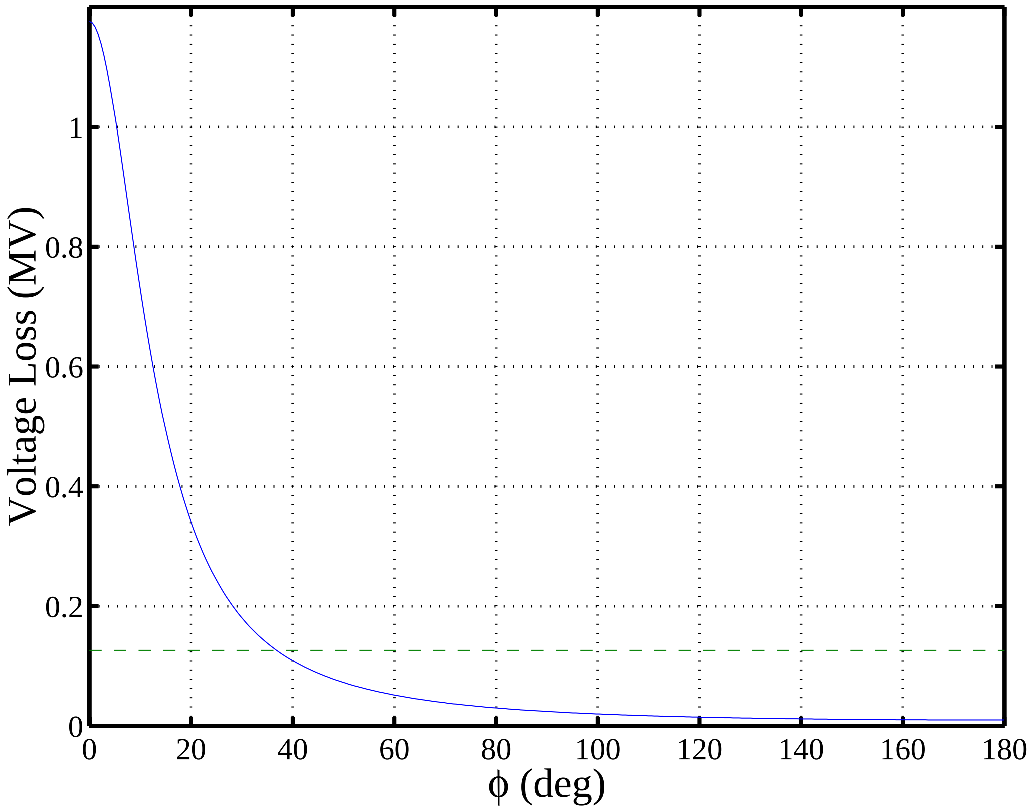

Figure 4.21: Plot of expected voltage build up dependent on the phase length of the recirculator.

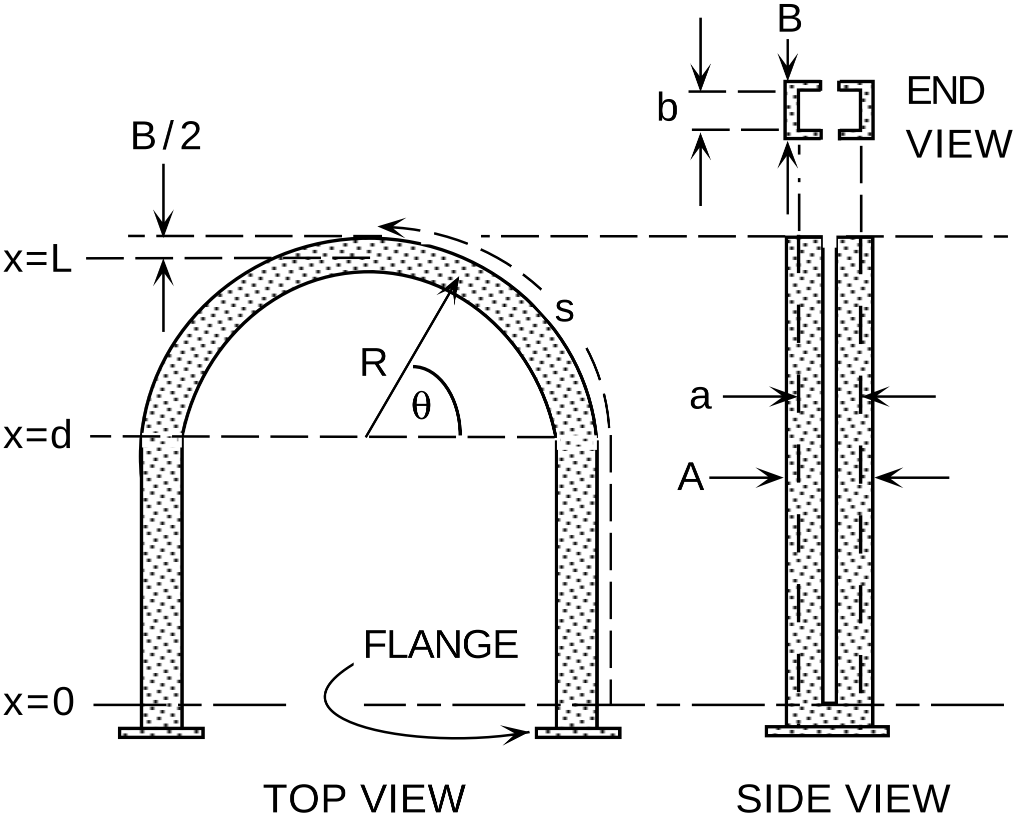

Figure 4.22: Sketches of the squeeze-type phase-shifter, not to scale, showing radius of curvature R, waveguide inner dimensions $a \times b$ and outer dimensions $A \times B$.

guide changes the guide wavenumber, k_z, and therefore the phase length of the guide.

$$\phi = \int_0^L k_z ds \tag{4.25}$$

$$k_z = \frac{2\pi}{\lambda}\sqrt{1 - \left(\frac{\lambda}{2a}\right)^2} \tag{4.26}$$

where a is the broad wall dimension and λ the free space wavelength at the desired frequency.

For small deviations δa in the waveguide width, the change in phase length is

$$\Delta\phi = \frac{\pi^2}{a^3 k_z}\int \delta a(s) ds \tag{4.27}$$

where s is arc length around the phase-shifter as seen in Fig. 4.22. The variation δa is a function of distance from the cut, x, and has an end point deviation of Δa

$$\delta a(x) = \frac{\Delta a}{2}\left[3\left(\frac{x}{L}\right)^2 - \left(\frac{x}{L}\right)^3\right] \tag{4.28}$$

The geometry, coordinates and dimensions are shown in Fig. 4.22. Integrating, we find the phase length deviation of the U-shaped phase shifter as a function of Δa, and guide dimensions

$$\begin{aligned}\Delta\phi &= \frac{2\pi^2}{k_z a^3}\left(\int_{x=0}^{d} \delta a(x)\, dx + R\int_{\theta=0}^{\pi/2} \delta a(d + R\sin\theta)\, d\theta\right) \\ &= \frac{\pi^2 \Delta a}{k_z a^3 L^3}\left(\frac{3}{4}d^4 + (1+\pi)Rd^3 + \left(\frac{3\pi}{2} + 3\right)R^2 d^2 \ldots \right. \\ &\qquad \left. + 6R^3 d + \left(\frac{3\pi}{4} - \frac{2}{3}\right)R^4\right)\end{aligned} \tag{4.29}$$

where $L = d + R$, with $R = 0.5$" and $d = 1.76$". The total phase length through the arm is calculated by integrating the wave number over the length of the arm and adding the perturbation $\Delta\phi$ from Eq. 4.29.

Meanwhile, as for mechanical considerations, the necessary force required for the deflection Δa is

$$F = -\frac{3EI_y}{L^3}\Delta a \tag{4.30}$$

where $E \approx 1.17 \times 10^{11}$ N/m^2 is Young's modulus for OFE Cu, and the moment of inertia of the cross-section is $I_y \approx (AB^3 - ab^3)/12$. With this one may show that the maximum stress on the copper is

$$\sigma_{\max} = -\frac{3EB}{4L^2}\Delta a. \tag{4.31}$$

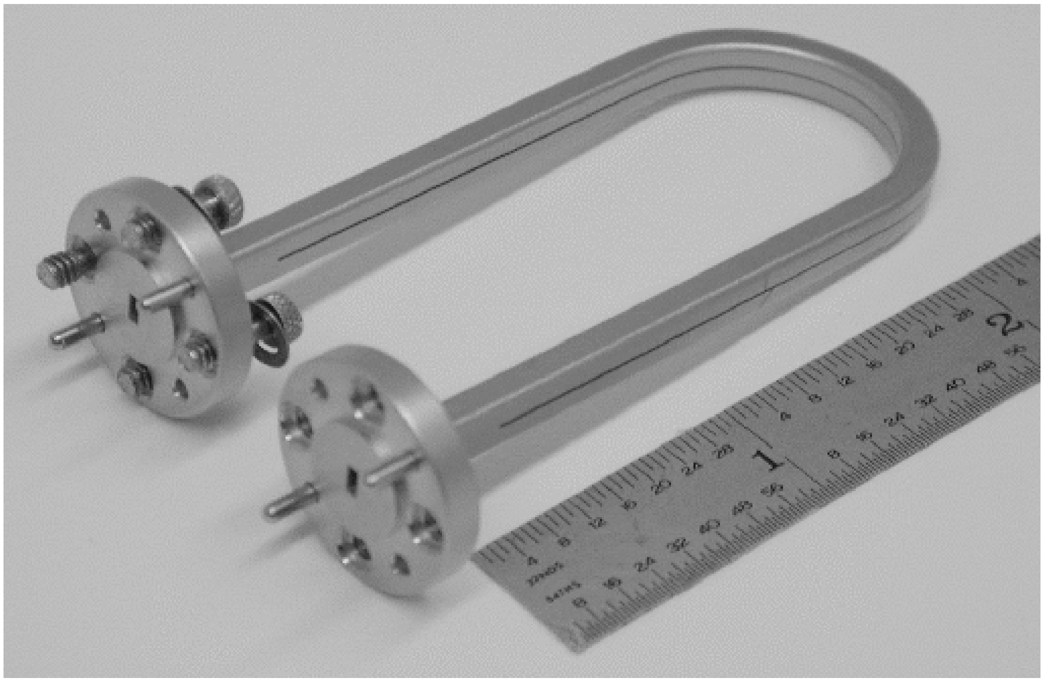

Figure 4.23: Picture of prototype phase shifter (scale in inches).

To prevent plastic deformation of the waveguide and hence maintain repeatability, we avoid stressing the guide more than 5% of its yield strength, $Y \approx 6.9 \times 10^7$ N/m^2.

With these design scalings in hand, we fashioned a phase-shifter using a 8" length of extruded OFE copper, with interior dimensions as for WR10. A slit was cut through the broad wall by EDM to facilitate squeezing, and 304L stainless steel flanges were furnace brazed using CuAu 90/10 alloy. The finished assembly seen in Fig. 4.23 was then chemically cleaned as this has been found in waveguide studies to remove any zinc or other unwanted material from redeposit during the EDM process and substantially reduce attenuation.

We characterized the S-matrix for this device under low power using a W-band vector network analyzer (VNA) [34]. We took VNA measurements for a series of values of Δa with the help of a stack of feeler gauges used to control the slit gap. The data are summarized in Fig. 4.24 showing the phase shift versus Δa at 91.4 GHz. The calculated phase shift from Eq. 4.29 is plotted with the measured data in Fig. 4.24, giving good agreement. The insertion loss seen in Fig. 4.25 is a factor of 2.7 worse than the theoretical

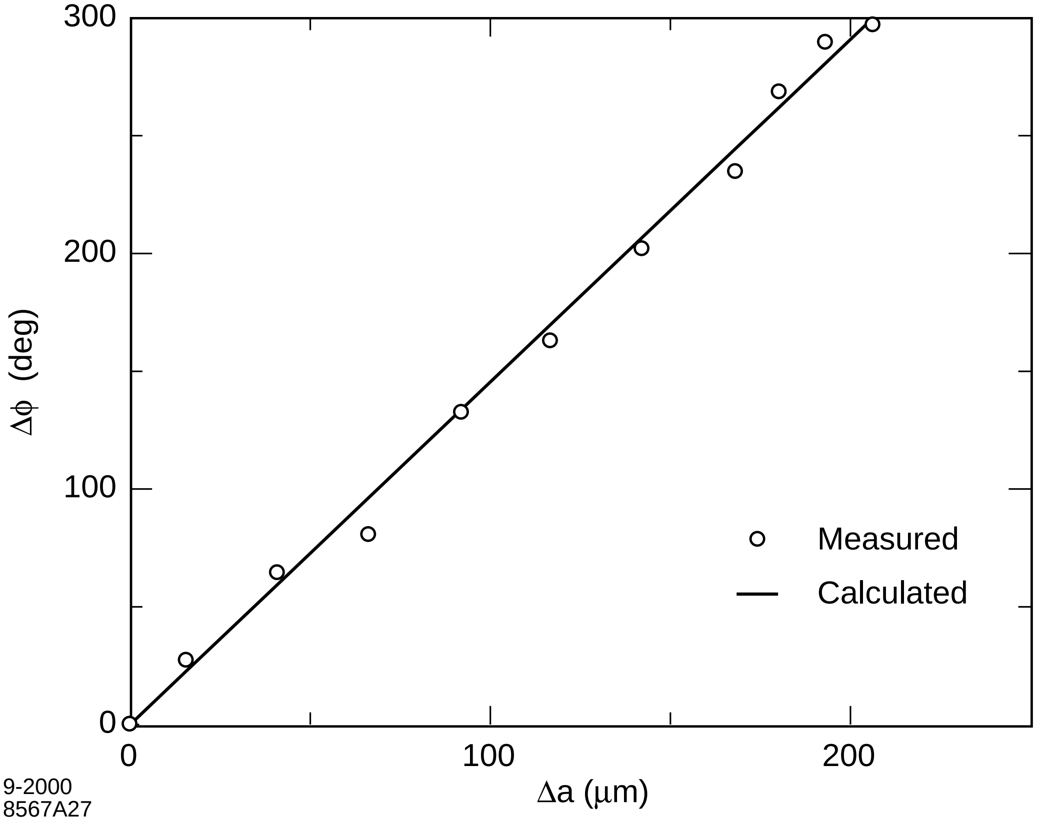

Figure 4.24: Measured points overlayed with analytical calculation.

result for straight TE_{10} mode attenuation in OFE WR10, given by Eq. (4.3),

$$\alpha = \frac{R_s}{Z_0}\left[\frac{\omega^2}{c^2}\frac{1}{b} + \frac{2\pi^2}{a^3}\right]\frac{c}{\omega}\frac{1}{k_z}, \tag{4.32}$$

where $R_s = 0.073\Omega$ at the operating frequency of 91.4 GHz and $Z_0 = 377\Omega$ is the impedance of free space. The disparity between theoretical and measured values are attributed to surface roughness and loss in the waveguide slit.

We will describe the test of this phase-shifter and the other components in the following chapter, but will summarize the results for the phase-shifter here. We employed the phase-shifter in the traveling wave resonator circuit of Fig. 4.20 at power levels above 180 kW giving field levels above 10.5 MV/m for 100 ns for several million pulses at 10 Hz with no sign of breakdown. We revisit Table 4.5, revealing the field levels for different power levels in WR10 and WR90 waveguide to illustrate the power required for testing under high fields at W-band compared with X-band. Tests at X-band producing equivalent fields would

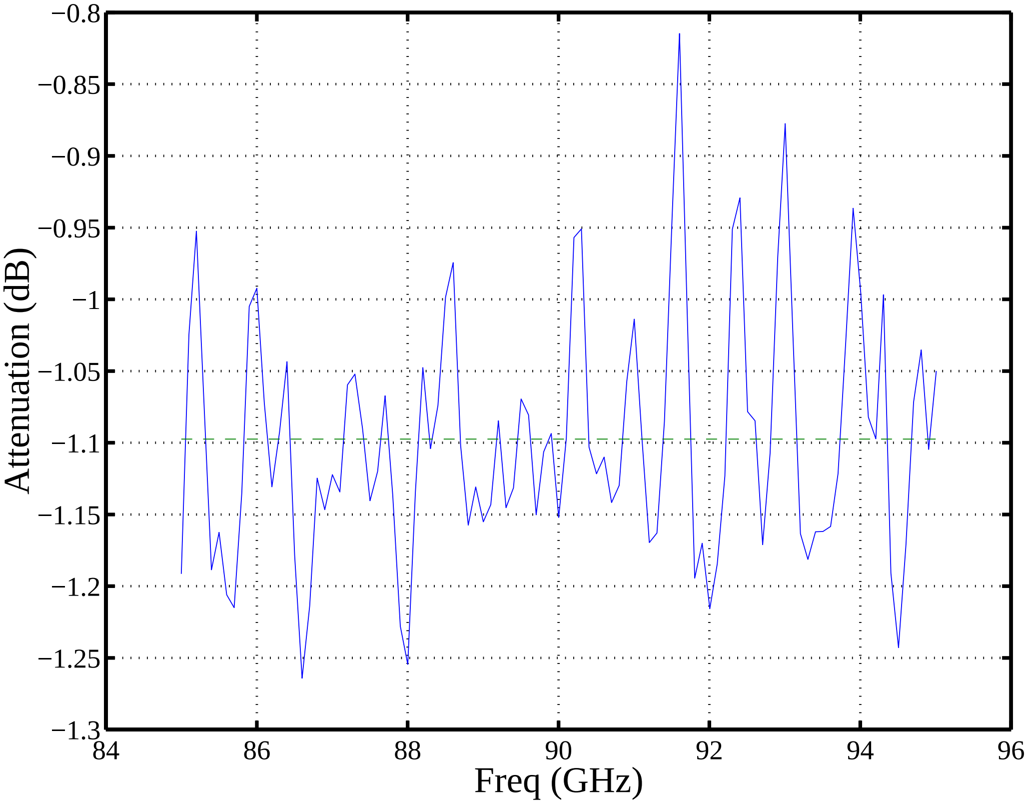

Figure 4.25: Attenuation through the phase shifter/recirculator versus frequency. The average attenuation is -1.1 dB.

require 2 MW of power.

Having described each of the necessary components for high-gradient testing, we go forth to describe the tests of these objects in the relativistic klystron two-beam approach.

Chapter 5

Structure Studies with Beam

To study W-band structures at high fields we proposed driving these structures using an electron beam due to the lack of a high power W-band source. The most appropriate accelerator was the NLCTA. For the purpose of structure studies we have employed the beamline illustrated in Fig. 5.1, a reconfigured portion of the NLCTA. Essential features include an X-band bunched beam that delivers 0.5 A current, 1.2 ps bunch length, focussed to $100\times200\ \mu\text{m}^2$ beam at the structure under test. Beam current, energy, and bunch spacing are all controllable parameters. Basic beamline instrumentation has been described in Ch. 2 and includes fast toroids, BPMs, profile monitors, and a time-resolved spectrometer with an energy resolution of 0.1%. Systematic effects present here include: noise on the toroid caused by the kicker, head and tail of the bunch train not distinguishable on the BPMs, burn spots on the profile screens, and wire scanners requiring very low background radiation for successful measurement.

For these tests we operated the machine using three klystron stations that powered 6 accelerator structures to give an electron energy of 300 MeV. In Fig. 5.2 we show a schematic of the RF network powering the accelerator structures.

5.1 Beamline (NLCTA)

The W-band interaction region is located in a 1-m section of the NLCTA beamline between the last accelerator section and the spectrometer. This spot was chosen to accommodate the test apparatus and an additional quadrupole magnet. The added quad makes a doublet for squeezing the beam down to a nominal $100\times200\ \mu\text{m}^2$ size. The rest

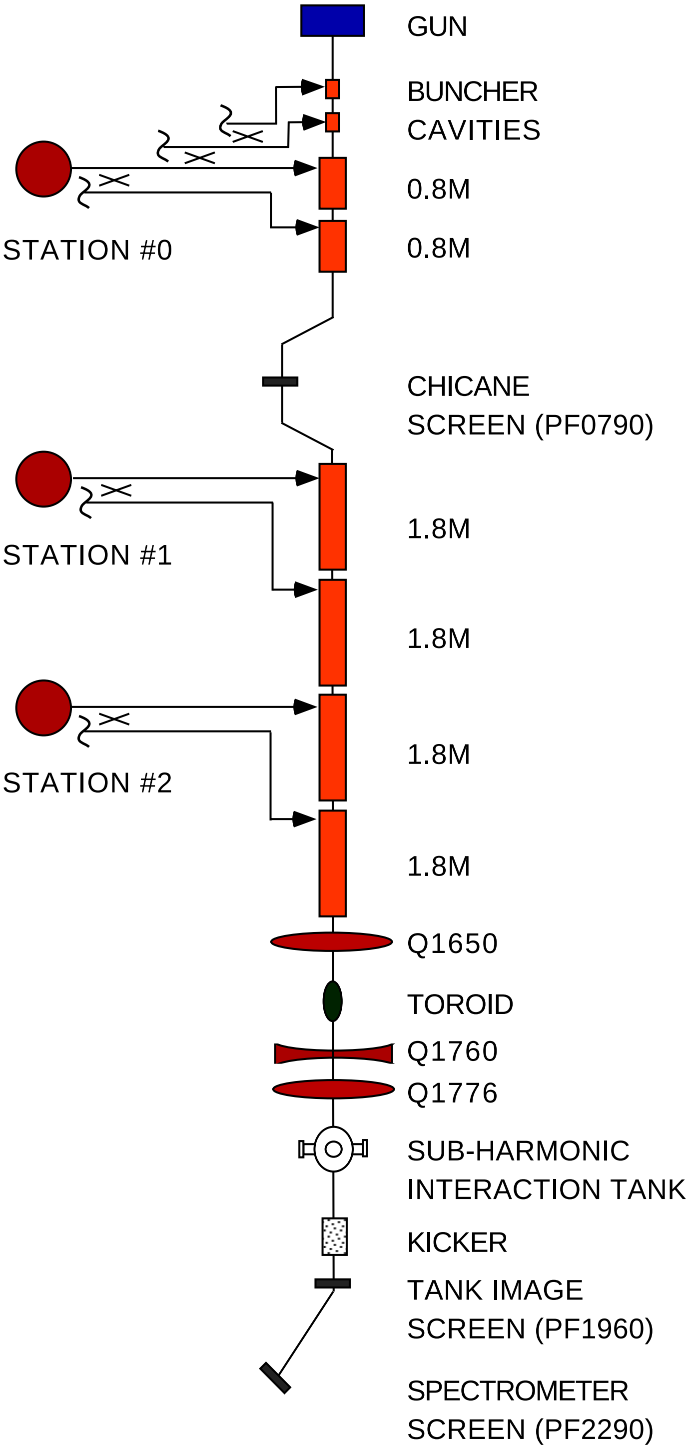

Figure 5.1: Schematic diagram of the NLCTA beamline. Electrons emerge from the DC gun at the top of the page, are bunched at 11.424 GHz in the two buncher cavites, are accelerated to 300 MeV, and finally focused to transmit through the W-band structure under test in the interaction tank.

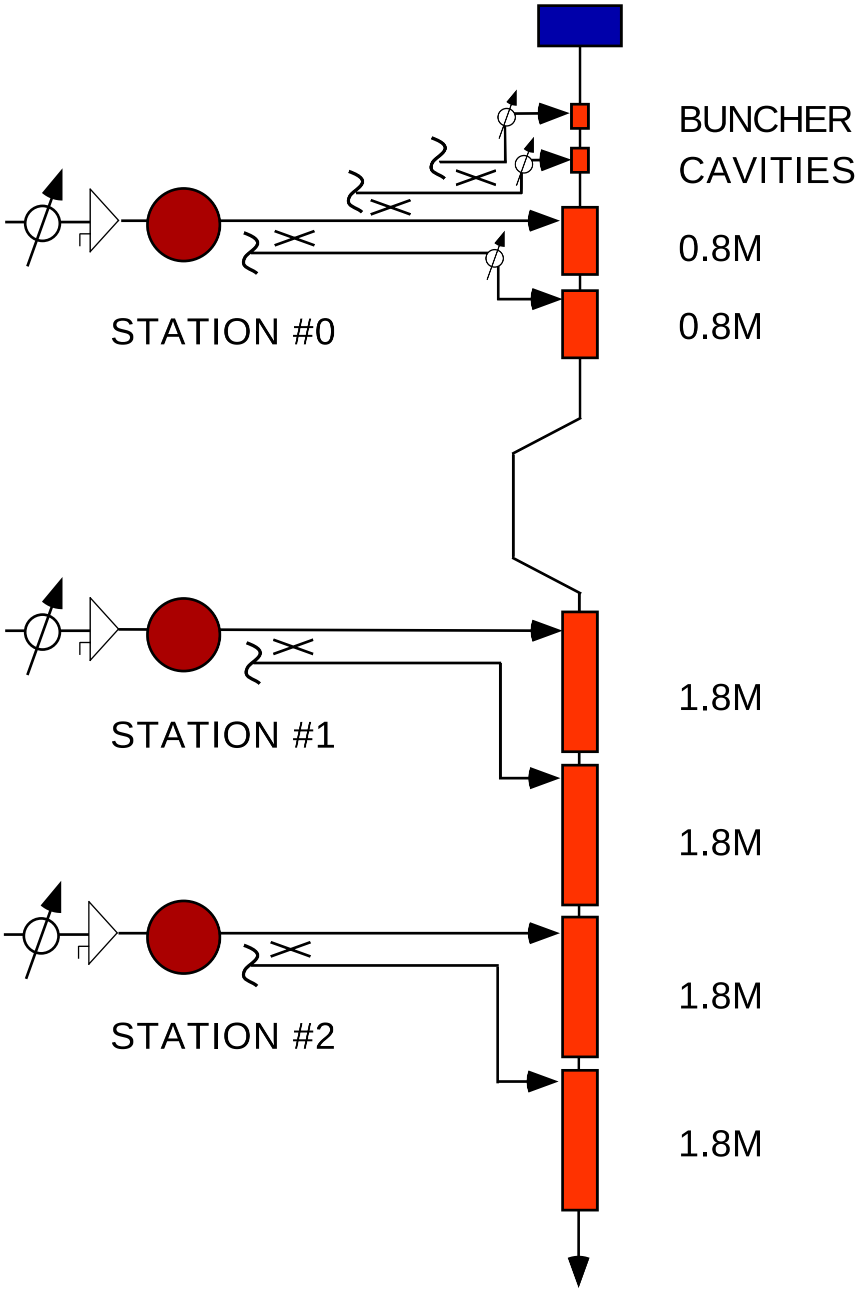

Figure 5.2: Schematic of NLCTA RF system, outlining the power coupling scheme and phase control.

of the NLCTA lattice was also adjusted to recover the squeezed beam for analysis through the spectrometer.

Without modifying the NLCTA lattice upstream of the last accelerator section, we used the program Methodical Accelerator Design (MAD) [35] to adjust the lattice to our given constraints. These constraints were a beam waist of less than 200 μm at the IP, containment of the beam through downstream elements (including a 6 mm kicker opening), another beam waist at the downstream profile monitor and maintenance of the dispersion for energy measurements in the spectrometer. Figs. 5.3 and 5.4 show the lattice in terms of beta functions for the original and modified beamline.

5.1.1 Interaction Region Isolation Considerations

We considered isolating the vacuum between the interaction region and the upstream linac by placement of a thin metal beam window. For a window of this type, we must consider mechanical stresses (e.g. heat and pressure), as well as beam interaction. The worst case NLCTA beam parameters at the vacuum chamber would be: 340 MeV electron beam energy, 1400 bunches $\times$ 5 10^8 e^-/bunch $\times$ 10 Hz, 100 $\times$ 600μm^2 beam area (worst case), and a normalized emittance of 50 mm mrad.

Most values are calculated assuming the use of a 25 μm thick stainless steel foil as a window.

The power dissipated in the window is

$$P_w = \left(-\rho \frac{dE}{dx}\right) N e R \delta$$

where ρ is the density, $\frac{dE}{dx}$ the energy loss in the material, N is the number of electrons, e the electron charge, R the repetition rate and δ is the thickness of the material.

For stainless steel, $\left(-\rho \frac{dE}{dx}\right) = 11.7$ MeV/cm and we will consider a 25 μm thick foil to get

$$P_w = 3.3 \text{ mW}.$$

Assuming a Gaussian distribution (100μm$\times$600μm), we get a pulsed temperature rise of

$$\Delta T = \frac{P_w}{C_h} = 70^o C$$

where C_h includes the volume of material being heated. This pulsed heating is large, but not unreasonable for stainless steel.

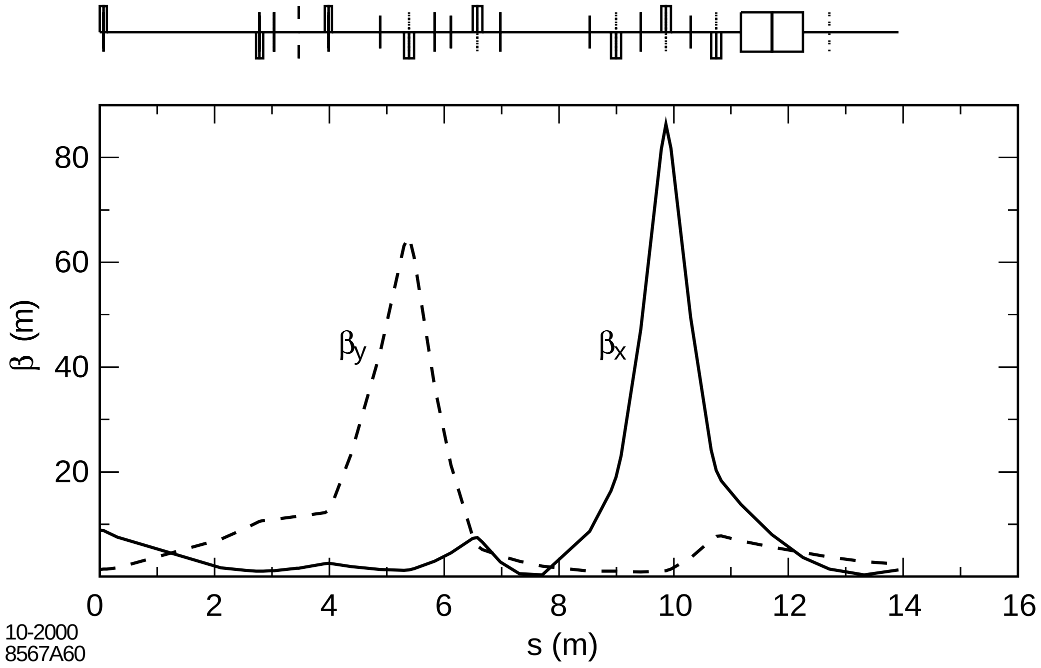

Figure 5.3: Beta functions for nominal NLCTA running.

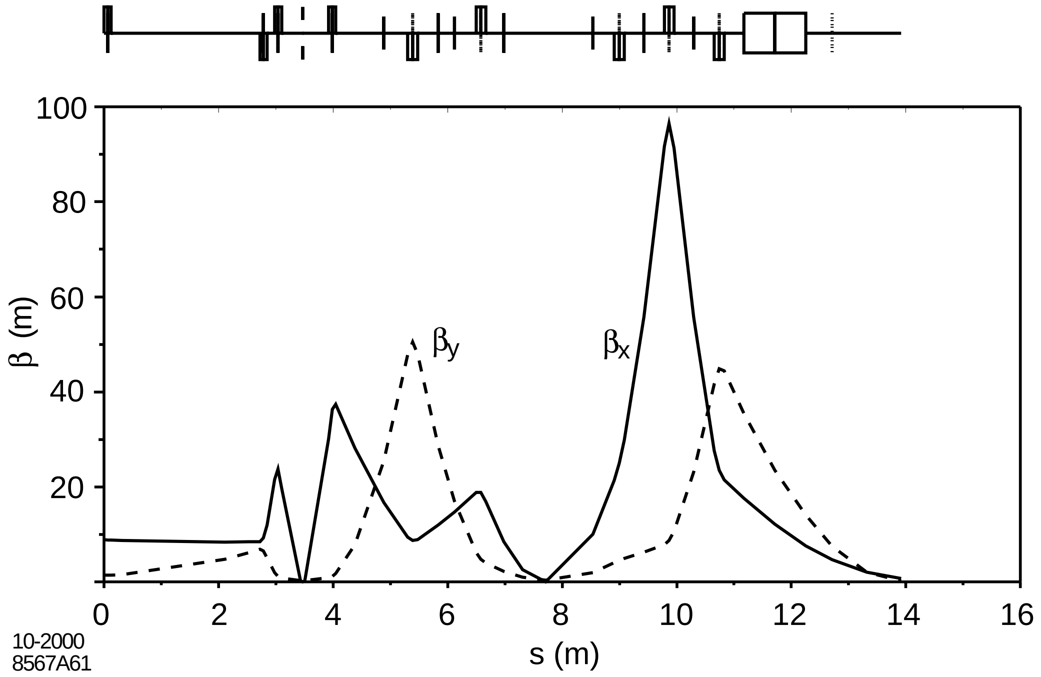

Figure 5.4: New Beta functions for NLCTA powered W-band.

Using a safety factor of 2 on the atmospheric pressure, the mechanical stress is

$$\sigma = \frac{Pr}{2\delta} = 7,400 \text{ psi}$$

where P is the pressure differential, $r = 0.5$ inches, the radius of curvature and $\delta = 25\ \mu$m is the foil thickness. The stress is well under the yield strength for stainless steel at $\approx$30,000 psi.

With $\beta = 5$m, the angular spread of the beam at the window is

$$<\sigma_x'>= \sqrt{\frac{\epsilon_n}{\beta\gamma}} \approx 0.1 \text{ mrad}$$

The multiple scattering due to a 25 μm foil is [36]

$$\theta_o = \frac{13.6 \text{ MeV}}{\beta c p}\sqrt{\frac{\delta}{X_o}}\left[1 + 0.038 \ln \frac{\delta}{X_o}\right] = 1.3 \text{ mrad}$$

$$\rho X_o = \frac{716.4\ A}{Z(Z+1)\ln\left(\frac{287}{\sqrt{Z}}\right)}\frac{\text{g}}{\text{cm}^2}$$

where A is the atomic mass, Z the atomic number and βcp= 300 MeV. For stainless steel $X_o = 1.8$ cm. From Fig. 5.5, one can see that this foil would greatly increase the opening angle of the beam and hence destroy the beam emittance.

Fig. 5.5 shows the scattering angle versus foil thickness for beryllium and stainless steel. From this plot, we see that to reduce the multiple scattering to the level of the natural angular spread of the beam, we could take a maximum foil thickness of 7 μm for beryllium and stainless steel was ruled out. A beryllium window of this thickness would be too fragile to be practical.

5.2 Sub-Harmonic Interaction Tank

Conventional accelerator structures form their own vacuum envelope. To simplify the design, fabrication and assembly of the structures to be tested and to improve throughput for testing on the beamline we opted to simplify the problem by enclosing the entire structure inside an external vacuum enclosure. This sub-harmonic interaction tank as depicted in Fig. 5.6 consists of a 6-port cross mounted on a micro-stage installed on a precision mount fixed to the beamline. There are three ports available for mounting and instrumentation of the test structures. The tank acts as a universal mount for testing of any structure that will fit into the 4" ID port.

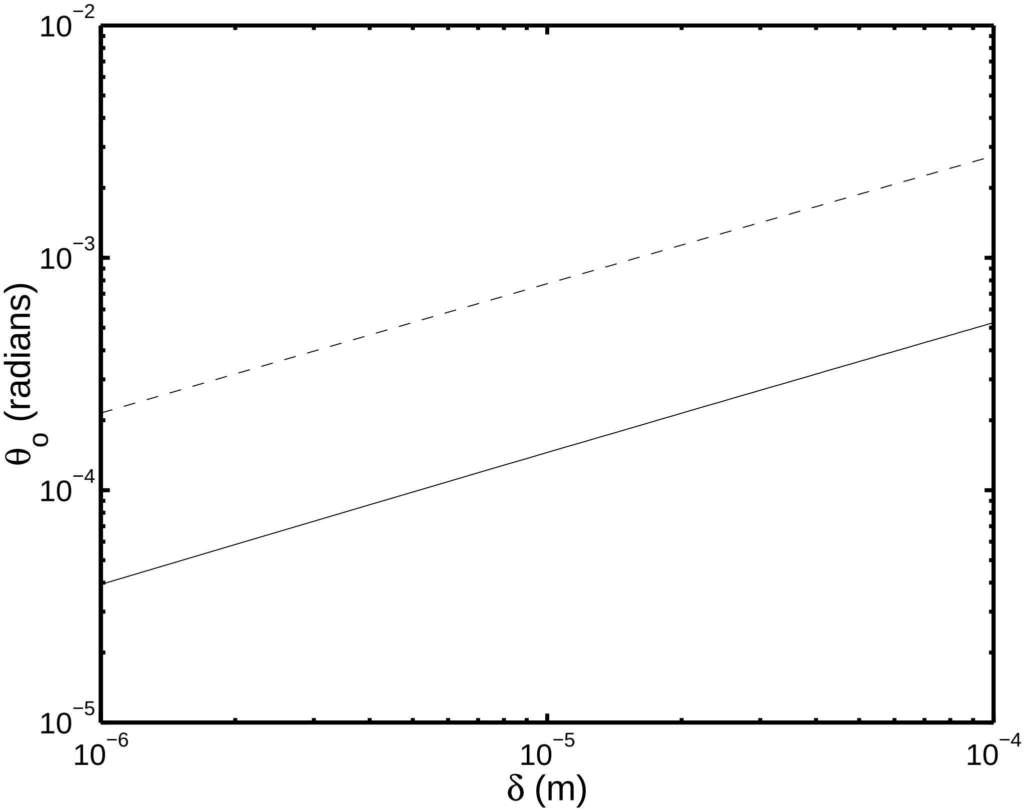

Figure 5.5: Multiple scattering for stainless steel (dashed) and beryllium (solid).

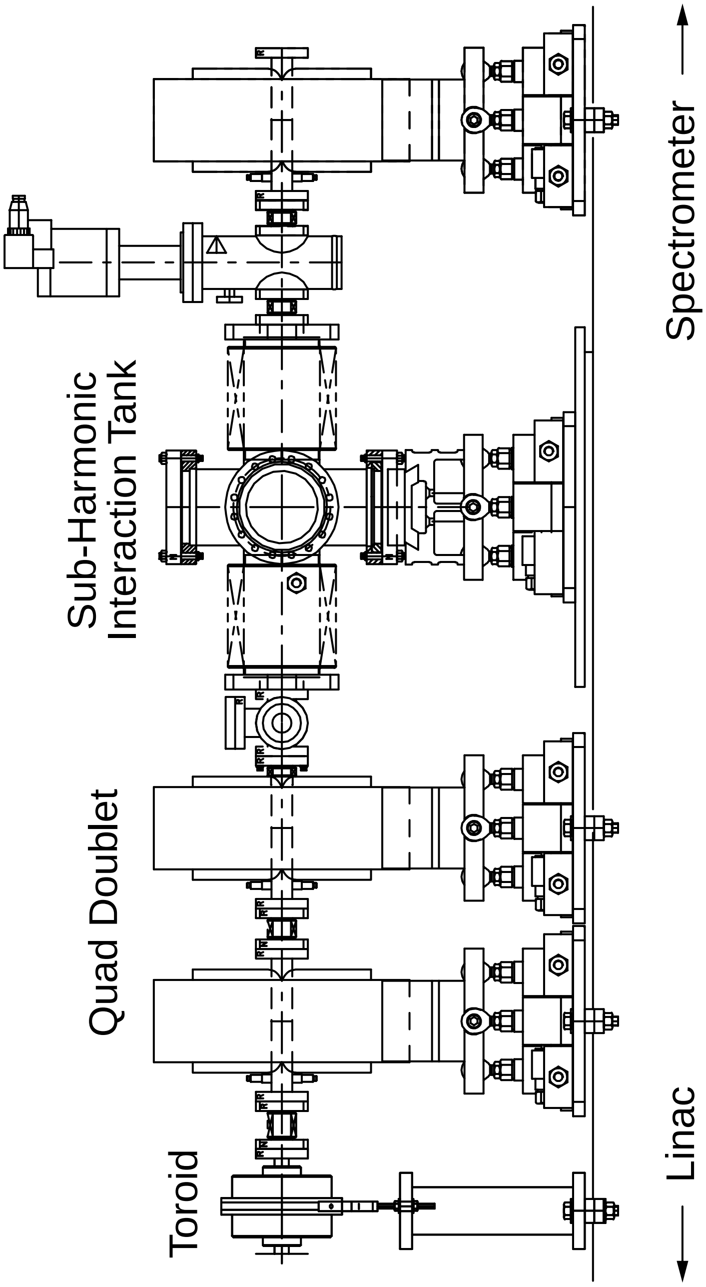

Figure 5.6: Girder view of the interaction region. Electrons travel from the bottom of the page to the top. Total length of the view is about 3 m.

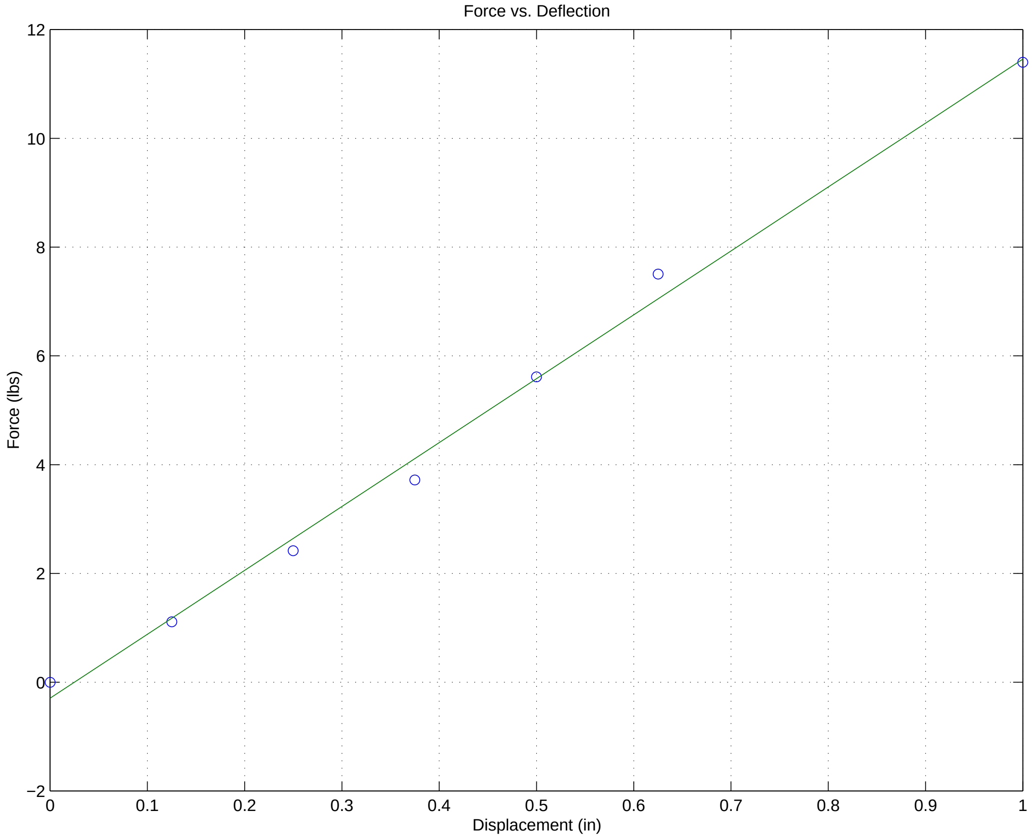

Figure 5.7: Force versus Transverse Displacement for Bellows

We opted to employ welded rather than electro-formed bellows to allow for a broader range of extension necessary for the two inch transverse motion of the tank on the micro-slide.

We settled on a 5.72" OD, 4.03" ID, 3 section bellows of 10 convolutions per section (Standard Bellows P/N 572-403-3-EE). Manufacturer data for these bellows included a longitudinal spring constant of 4.7 lbs/in and a maximum stroke of 5.07". Manufacturer data did not include a transverse spring constant and we determined the constant from bench measurements. To measure the transverse spring constant, we rigged the bellows to a weight system and measured the deflection for different weights, data shown in Fig. 5.7. We inferred a linear spring constant over the entire 1" deflection yielding a spring value of ≈12 lbs/in. The fact that the curve is linear also suggests that the bellows are not being plastically deformed.

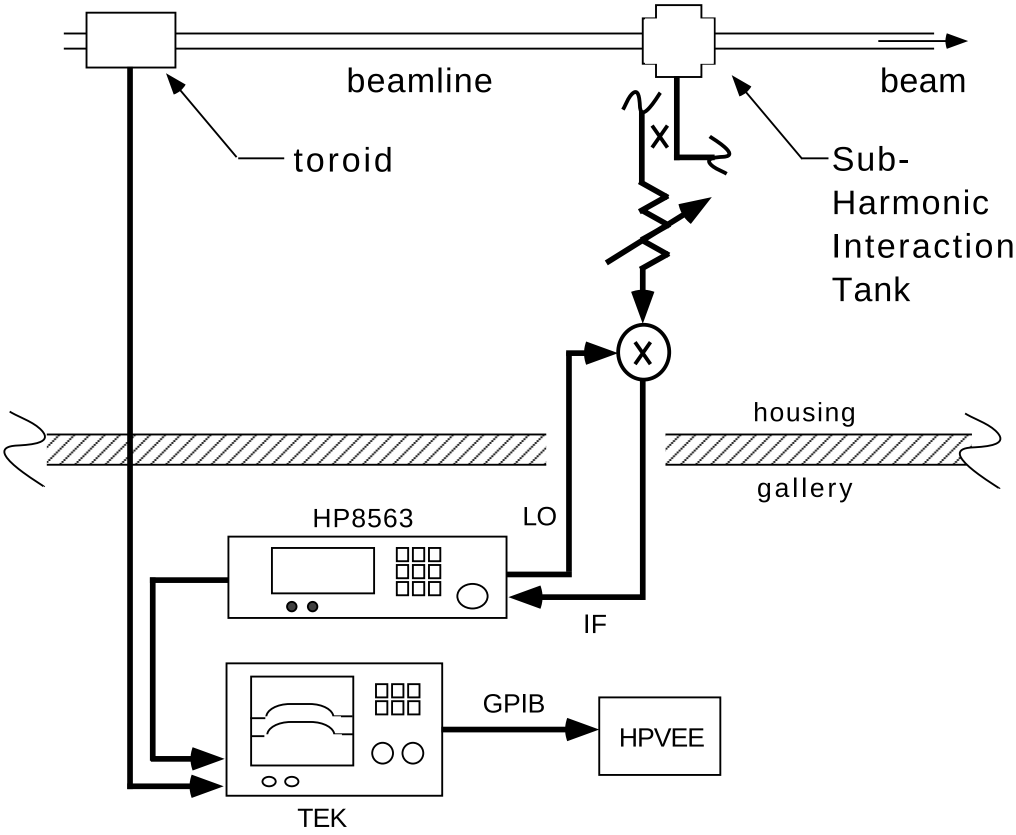

Figure 5.8: Schematic of W-band signal readout system.

5.3 W-Band Signal Processing

Signal processing is shown in Fig. 5.8 depicting the beam driven source, the WR10 waveguide and window (vacuum/air interface) and connecting waveguide through a W-band attenuator into a 18× harmonic mixer. In each of the experiments we used this scheme for the power readout. The very short attenuation length of W-band signals in waveguide (1 dB/foot, or even worse in cable), does not permit transporting the W-band signals out of the linac enclosure. For this reason we placed a W-band harmonic mixer close to the beam line shielded by a lead brick housing. Among the components are an HP 8563 spectrum analyzer running as a tuned receiver for the HP 11970W 18× harmonic mixer that down mixed the W-band signal to 300 MHz to be read by a Tektronics 1 GS/s real time oscilloscope.

The 18× harmonic mixer has a conversion loss of 48 dB and a sensitivity of

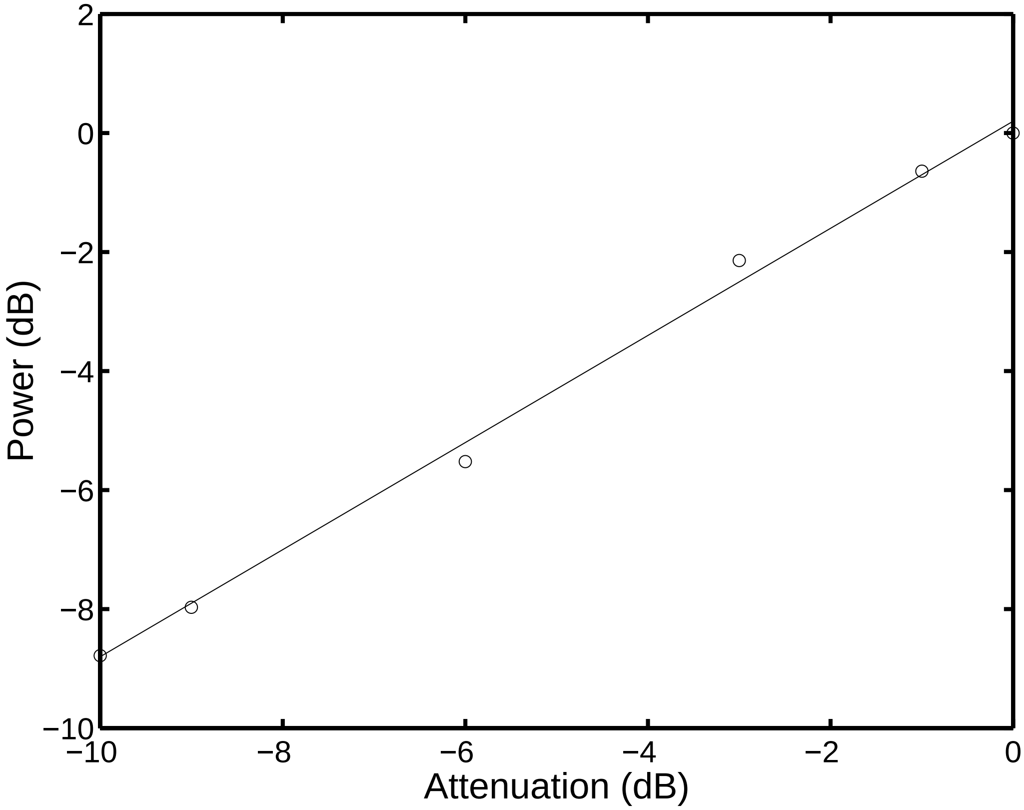

Figure 5.9: Plot of W-band detection circuit calibration overlayed with a fit of slope of 0.9.

1 mV/μW with a dynamic range of 60 dB. A plot confirming the linearity and calibration of the harmonic mixer using a power source and high precision attenuator is seen in Fig. 5.9. To determine the attenuation and match, the S-matrix is measured for the waveguide network that connects the structure on the beamline with the mixer on the floor. This measurement was repeated several times in the course of the studies with beam, confirming repeatability.

5.4 Beam Tune Up

The beam passing aperture of the first structure was a round hole of diameter 680 μm. The nominal beam size for the original NLCTA lattice at this location was 1x2 mm. It was for this reason that the triplet was added prior to the test setup. With the triplet in place, the NLCTA configuration was modified with the help of MAD to match beta functions through the rest of the linac shown in Fig. 6. In practice to achieve the desired beam size and orbit at the structure, a tune up procedure was required that we will now outline.

The tune up look something like this: first the structure was removed from the beam path with the help of the micro-slide. With the structure safely away from the beam's path, we then would tune the injector. The bunch phase and structure phases were adjusted to give minimum beam energy spread as observed in the chicane. The lattice model was confirmed by quad scan. The vertical kicker was turned on to reveal energy spread along the bunch train. The klystron timing and phases were adjusted to give maximum energy and at the same time minimum energy spread along the train. Following that, the triplet was adjusted to give the beam waist as depicted in Fig. 8, as monitored in a profile monitor π betatron phase advance downstream of the interaction point. Next, the beam was momentarily turned off while the structure support was moved into place to align the structure aperture into the beam orbit. The π phase advance was then confirmed by imaging the structure aperture on the downstream profile monitor.

Heat deposited by beam interception was a concern that drove the use of copper as the support structure. Copper has a sufficient heat conduction to remove the heat from the structure to the support flange. The temperature of the flange was monitored with a thermocouple which was read out with the SLAC Control Program (SCP).

We then made small adjustments to the triplet and orbit to maximize the beam transmission as monitored using the BPM stripline summation signal (TMIT). Fig. 5.10 shows transmission after tune up of the electron beam through a 2 mm diameter hole in the support block.

Nominal beam parameters for these measurements are 240 MeV, 0.5 A, bunch length of 1.2 ps, bunch train of 120 ns.

5.5 Test #1 — Single Cavity Resonator

The first of the series of tests is the study of a single RF cavity and an RF window, as described in Secs. 4.3 and 4.4. The corresponding RF circuit is that of Sec. 4.3 consisting of a cavity and a window with a mismatch. At the time we were not entirely confident that we could handle power on the order of 1 kW, in WR10, as it had not been done before to our knowledge. [Power levels of this order were later studied in WR10 at NRL.] This test

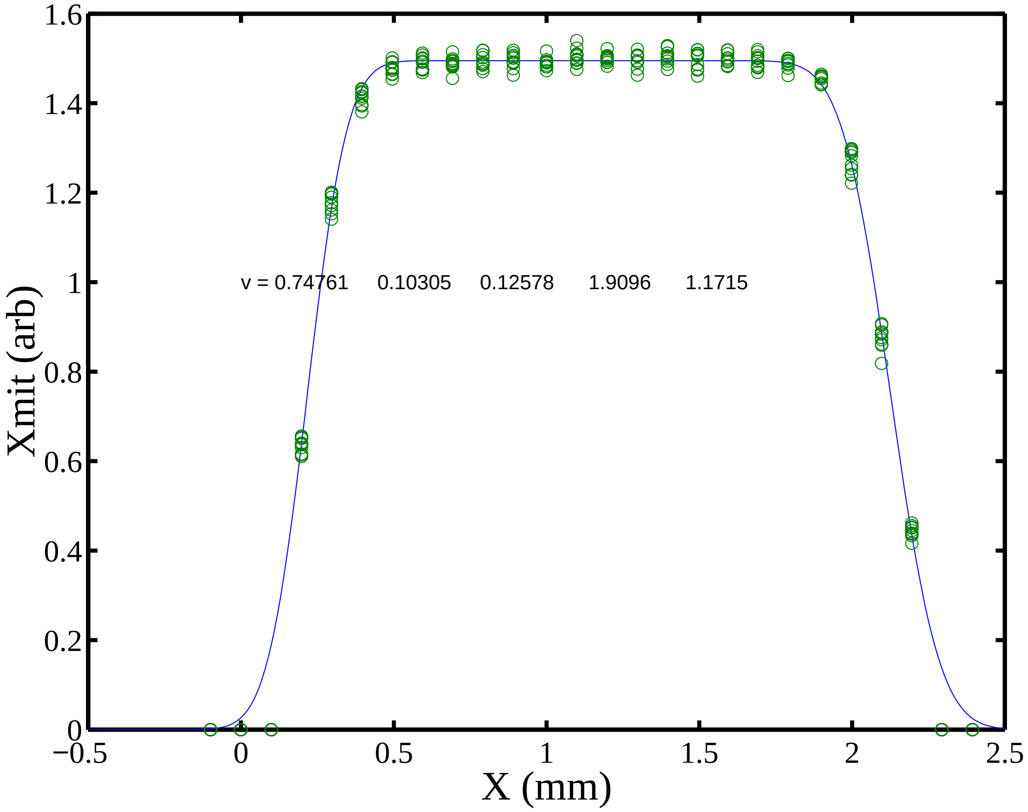

Figure 5.10: Beam transmission through a 2 mm diameter dummy target.

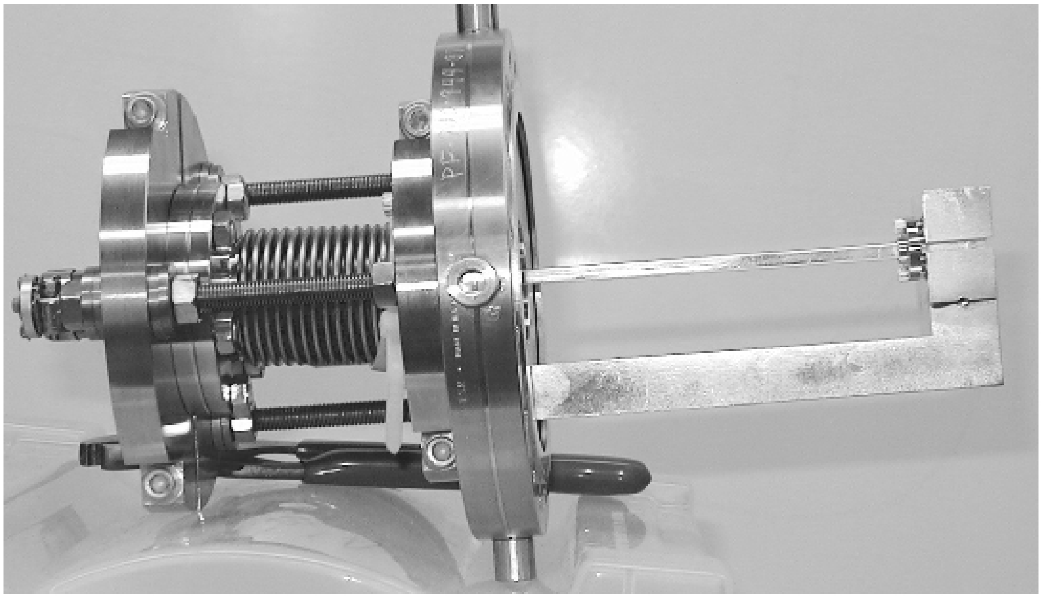

Figure 5.11: Picture of the single cavity and support arm.

gave us significant confidence to handle W-band signals of this magnitude.

The device under test (DUT) is seen in Fig. 5.11 mounted to a copper support arm positioning the cavity on axis in the beamline for testing. The support arms mounts to the 6" OD conflat flange of the six-way cross. The DUT consists of the single cavity and RF window described in Ch. 3. VNA measurements of the cavity-window system are shown in Fig. 5.12. We can infer a new Q_e and f_0 of the system from this measurement. The window has a non-zero reflection at the cavity's resonance frequency which causes a detuning of the cavity dependent on the VSWR of the window and the length of connecting waveguide.

The RF measurements in Test #1 consisted simply of observation of the RF waveforms as mixed down to 300 MHz. One such example of the data are shown in a screen dump in Fig. 5.13 showing the 300 MHz signal and the corresponding toroid current signal. Also seen in the figure is a Fast Fourier Transform (FFT) of the 300 MHz waveform from which we could easily check the output power.

A typical post processed waveform is that shown in Fig. 5.14, corresponding to a power of 800 W with a current of 0.25 A. These results correspond to structure parameters$[R/Q]$ =110Ω, $Q_w = 1305$, $Q_e = 571$, as in Table 4.4. A theoretical waveform is overlayed in this figure taking the beam current and these parameters according to

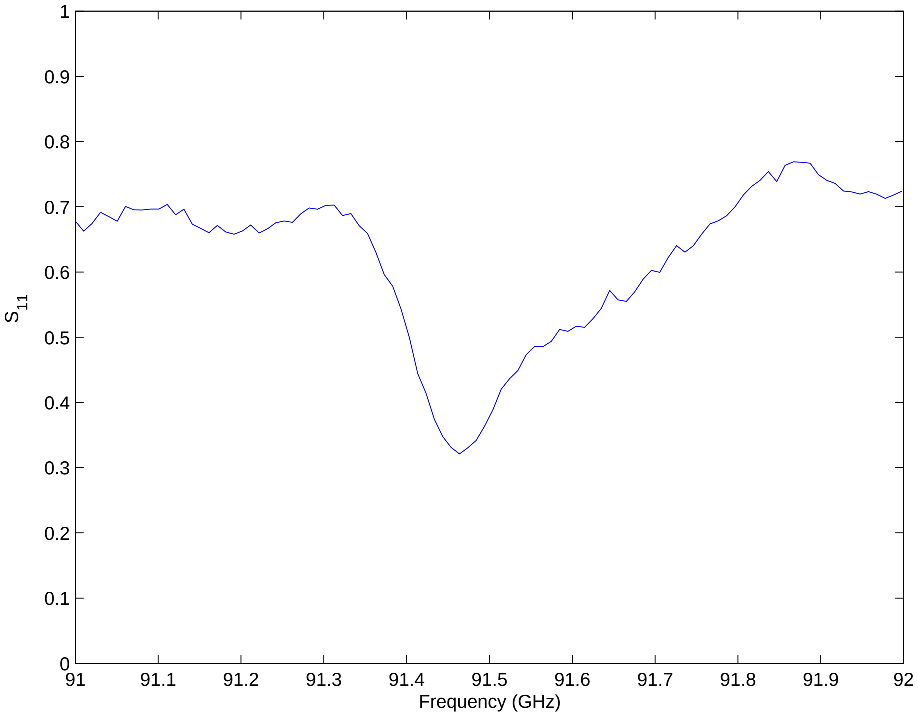

Figure 5.12: Reflection measurements of the cavity-window system under test.

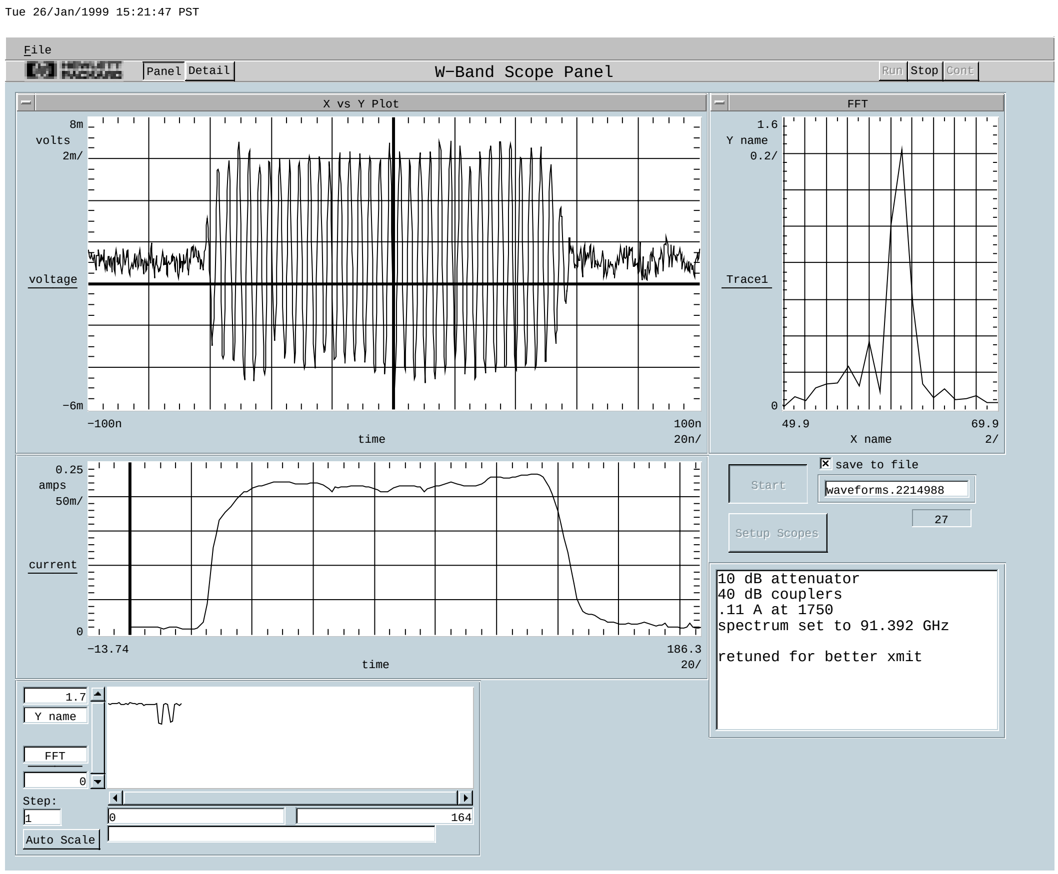

Tue 26/Jan/1999 15:21:47 PST

☒ save to file

waveforms.2214988

27

```
10 dB attenuator
40 dB couplers
.11 A at 1750
spectrum set to 91.392 GHz

retuned for better xmit
```

Figure 5.13: Screen dump of data acquisition system. Pictured are the W-band signal mixed down to 300 MHz, the toroid current signal, and a FFT of the W-band signal.

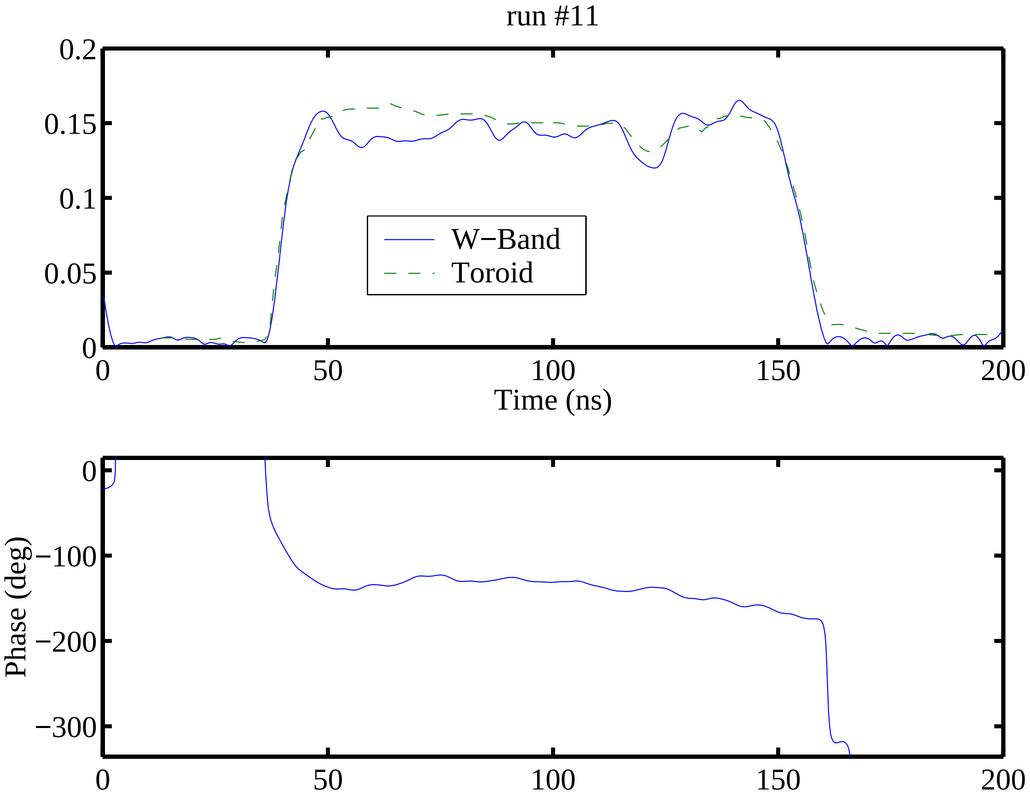

Figure 5.14: Typical post-processed waveform.

Eq. (4.4).

Over the course of several days data sets were collected for RF waveforms and corresponding current waveforms for a number of different current settings, results see in Fig. 5.15. Overlayed in this figure is the theoretical result,

$$P = \frac{\beta}{(1+\beta)^2} R_s \cos^2(\psi) I_8^2 \tag{5.1}$$

using parameters as in Table 4.4 and the detuned $Q_e = 650$ as determined from bench measurement of the cavity-window system in Fig. 5.12. The detuning of the cavity due to the window required us to run the injector off frequency to reach the highest power levels. We were able to run the injector 6 MHz from it nominal 11.424 GHz operating point, to bring us 48 MHz closer to resonance on the cavity.

After these studies the gate valve upstream was closed, the spectrometer was vented to remove the structure and the structure was inspected for damage from beam impinging around the iris. The visual inspection showed no particular damage and S_{11}

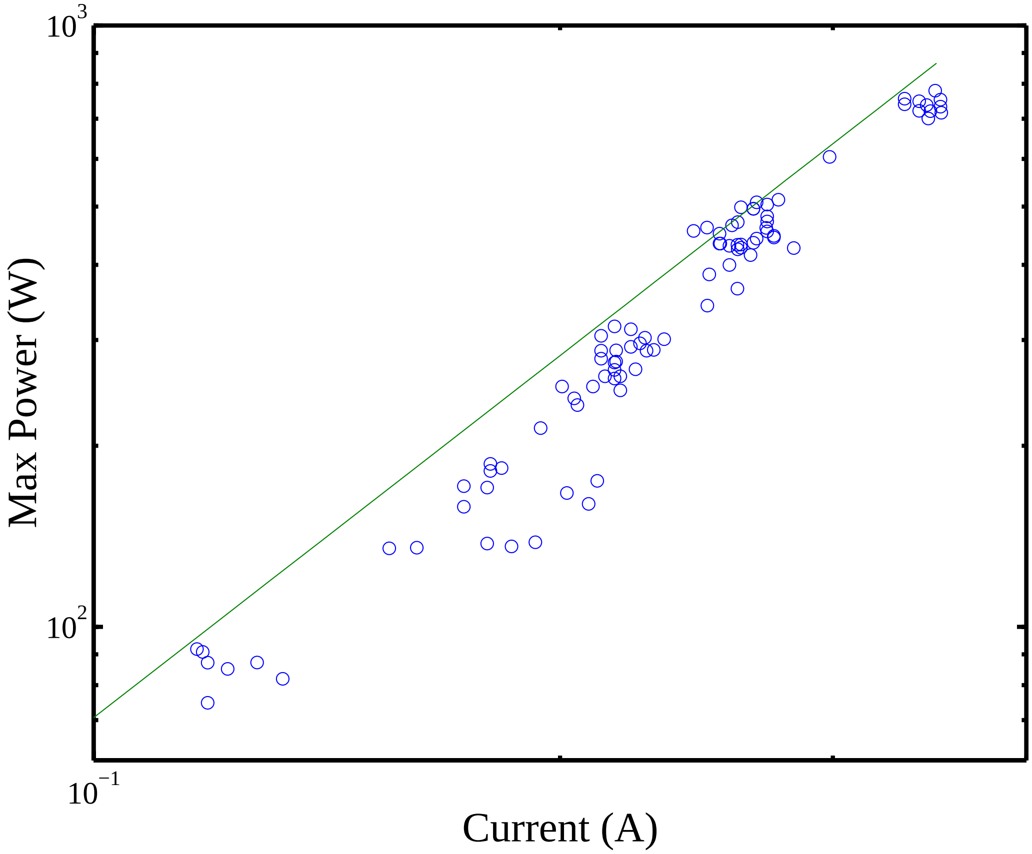

Figure 5.15: Plot of power levels reached versus input current.

measurements before and after beam testing were within the observed repeatability of the VNA. Thus in Test #1, we demonstrated the ability to drive a miniature RF circuit with a beam to produce kilowatt power levels without arcing. We also confirmed to our satisfaction that we could expect to test more elaborate structures with a 0.5 A beam without damaging these new structures.

5.6 Test #2 — Planar Dielectric Accelerator

In Test #2, the device under test consisted of the dielectric structure described in Sec. 4.5, followed by a stainless steel attenuator as described in Sec. 4.2, and a window as described in Sec. 4.4. The 6” conflat flange was modified to accommodate two windows for the signals from the input and output of the structure as seen in Fig. 5.16. As in Test #1, the tune up consisted of first tuning the injector for good transmission and energy spread determined with the chicane. Following injector tuning, employing the spectrometer screen and kicker we adjusted the timing and phase of the downstream accelerator sections to give low energy spread over the entire 120 ns bunch train. We then moved the structure into the beam for measurements.

The sequence of measurements was slightly different because we had only one mixer to measure RF output. Consequently, the signals from the input and output were not measured simultaneously, however they were measured under nearly identical beam conditions.

The sequence of RF measurements for Test #2 consisted of, observation of power signals from the output coupler under low current conditions (≈ 0.1 A), then under high current conditions (≈ 0.4 A). Following studies of power from the output of the structure, we observed input coupler signals under nominally identical beam conditions. The output from the input coupler was consistent with the power generated in the input coupler cavity. We did not observe breakdown from high fields or from dielectric charging at either the input or output.

Typical waveforms from the input and output are shown in Fig. 14. Outgoing voltage from the input arm corresponds to low power levels created only in the input coupling cavity. The outgoing voltage from the output arm corresponds to the power of 17 kW with a beam current of 0.5 A from which one may infer a shunt impedance of 2 MΩ. The beam current waveforms are similar to those shown for Test #1.

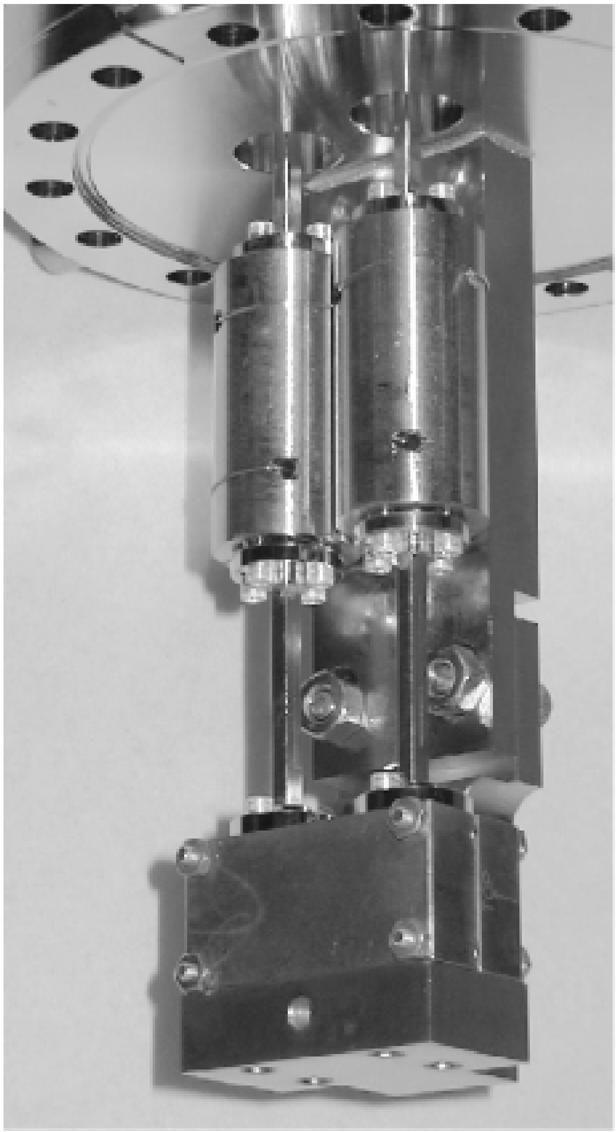

Figure 5.16: Picture of Test #2 structure showing the dielectric structure, high power attenuators and windows.

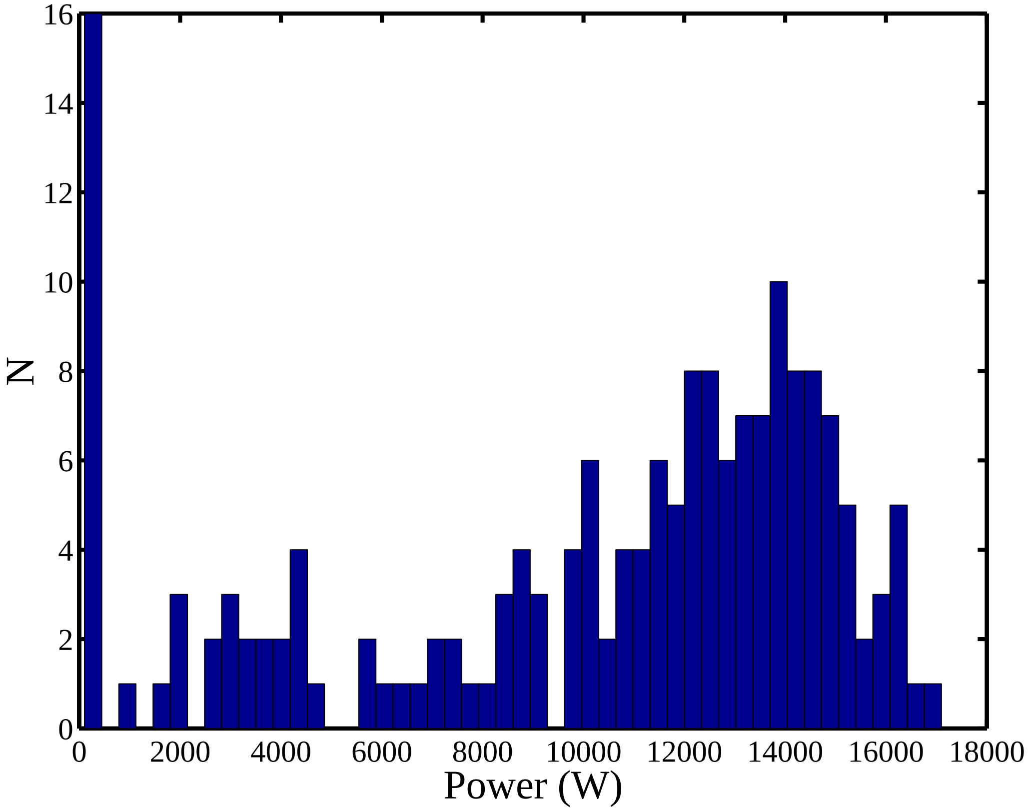

Figure 5.17: Histogram of peak power produced.

Fig. 5.17 shows a histogram of peak power levels for one data run. There are a total of ~100 waveforms. These collected waveforms represent about 1% of the total pulses produced for that run. The circuit model agrees with these measured values of output voltages for given input current.

After tests with the beam, the structure was removed and re-tested on the bench, shown in Fig. 5.18. The S-matrices were indistinguishable for the structure before and after 10^5 beam pulses.

5.7 Test #3 — PDA with Recirculation

For Test #3, we again modified the 6” flange to accommodate the phase shifter from Sec. 4.6. The top view of the setup is shown in Fig. 5.19 depicting the dielectric structure, phase shifter including 60 dB coupler. The squeeze type phase shifter could be

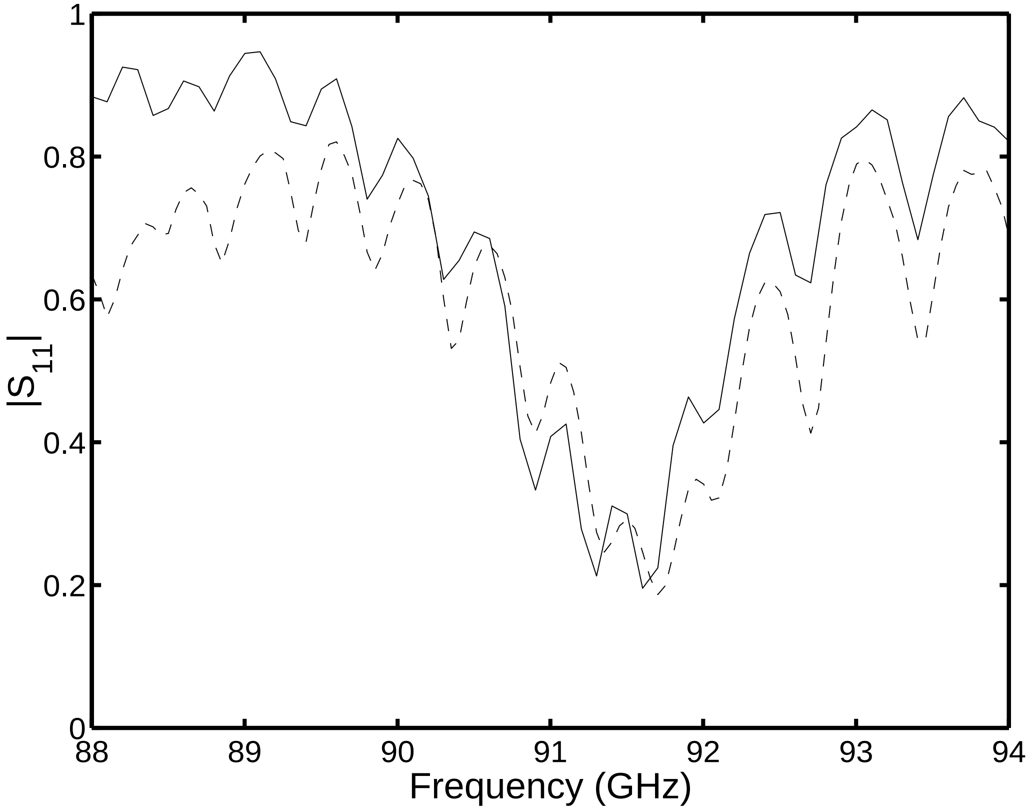

Figure 5.18: Comparison of S parameters before and after testing with beam.

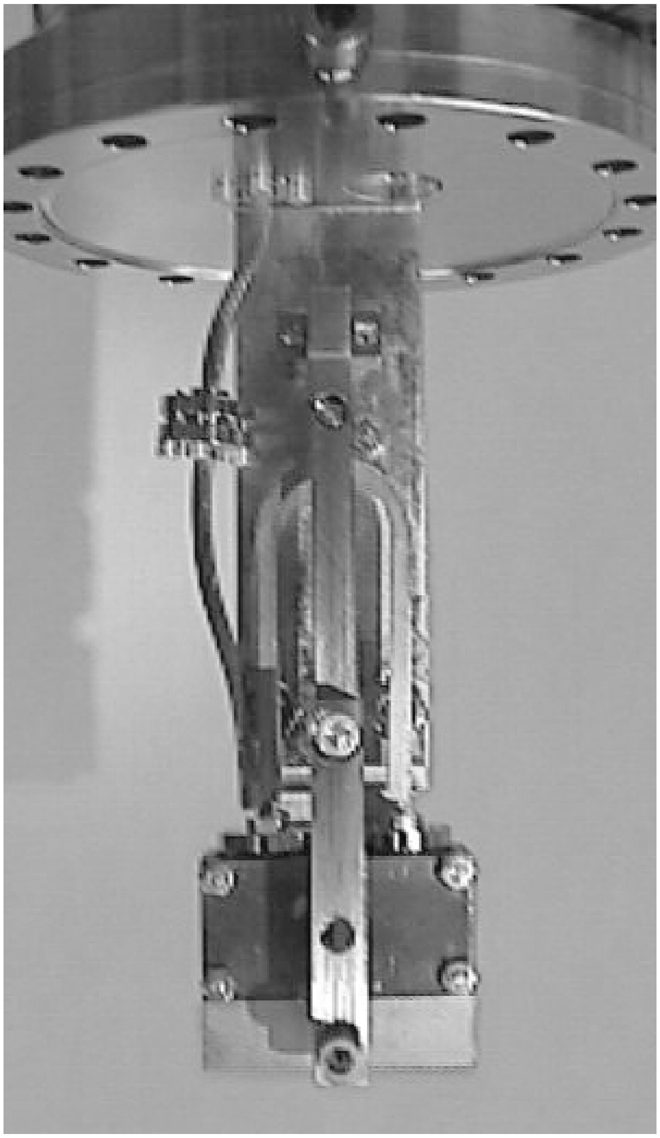

Figure 5.19: Picture of DUT for Test #3.

controlled through an actuator wired into the control system. In this study we monitored the power from the coupler as shown in Fig. 5.20, corresponding to 0.18 MW with a beam current of 0.5 A. The maximum power generated is shown versus phase shifter position in Fig. 5.21. Recall from Sec. 4.6 and Eq. (4.24) that the field enhancement from the power recirculator is 3.5, with a recirculator of attenuation, $A = 0.9$.

The horizontal beam passing aperture was slightly larger than in Test #1, at 760 μm, but the vertical beam passing aperture was 1 cm. This generous aperture allowed

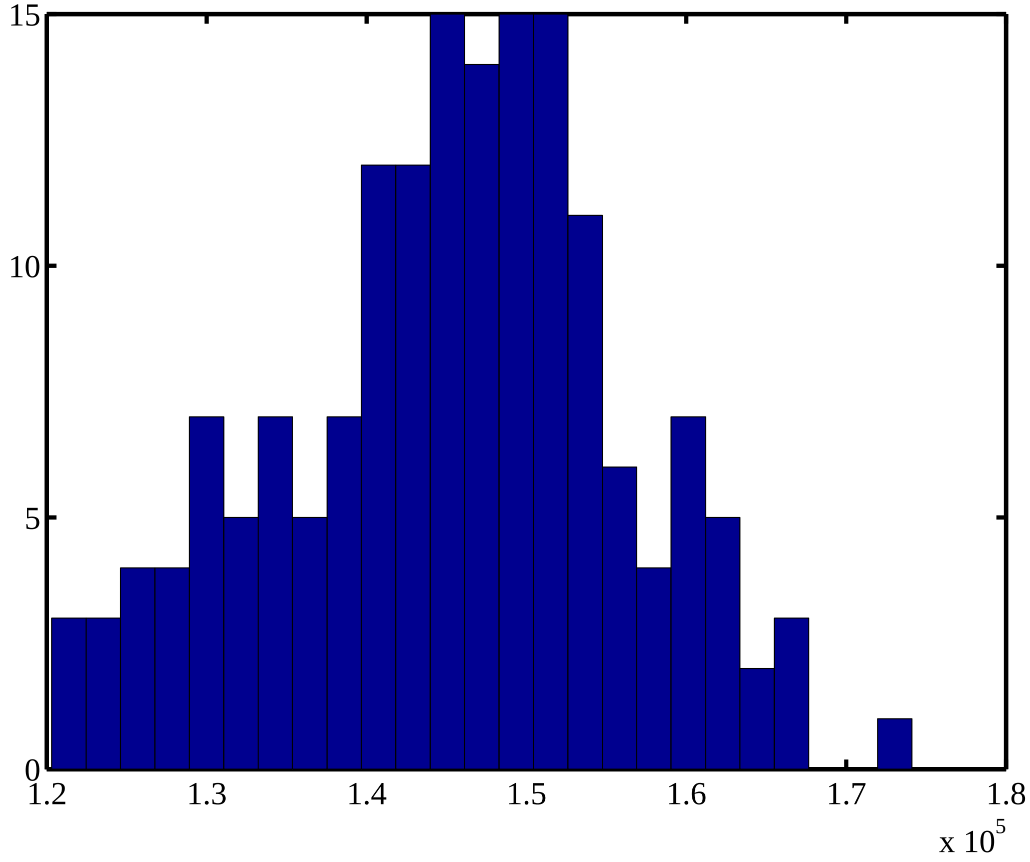

Figure 5.20: Plot of power levels reached.

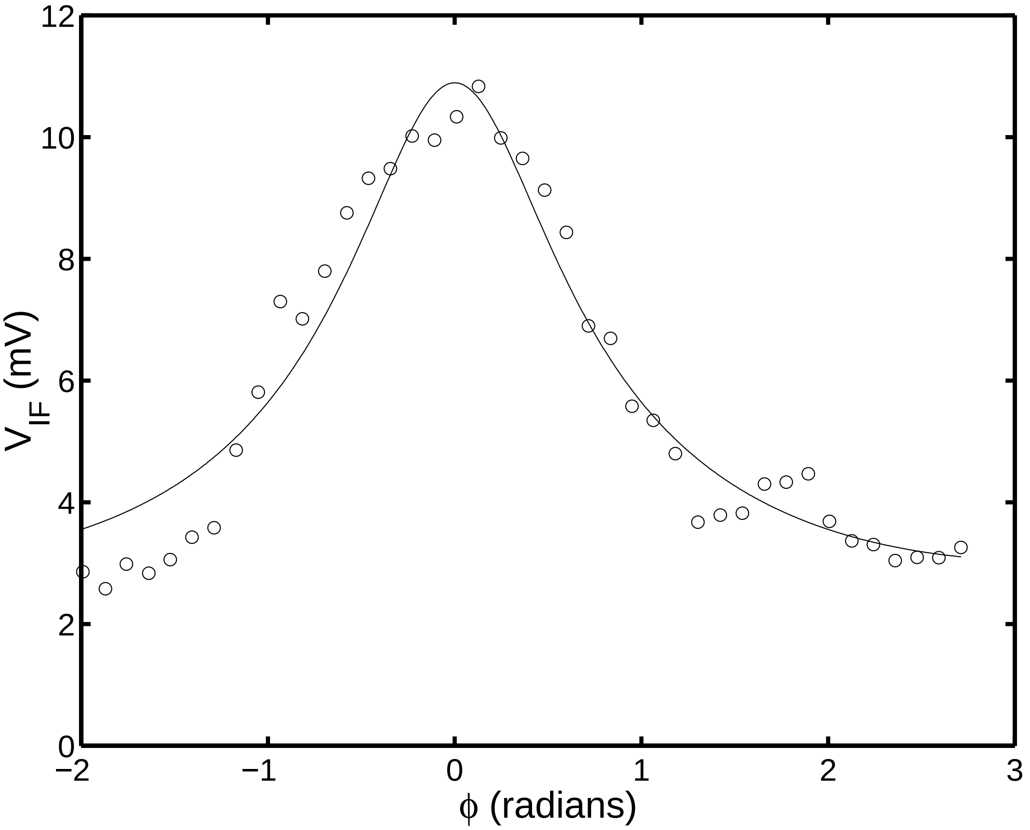

Figure 5.21: Plot of mixer voltage, V_{IF}, versus phase shift ϕ overlayed with a fit on the amplitude.

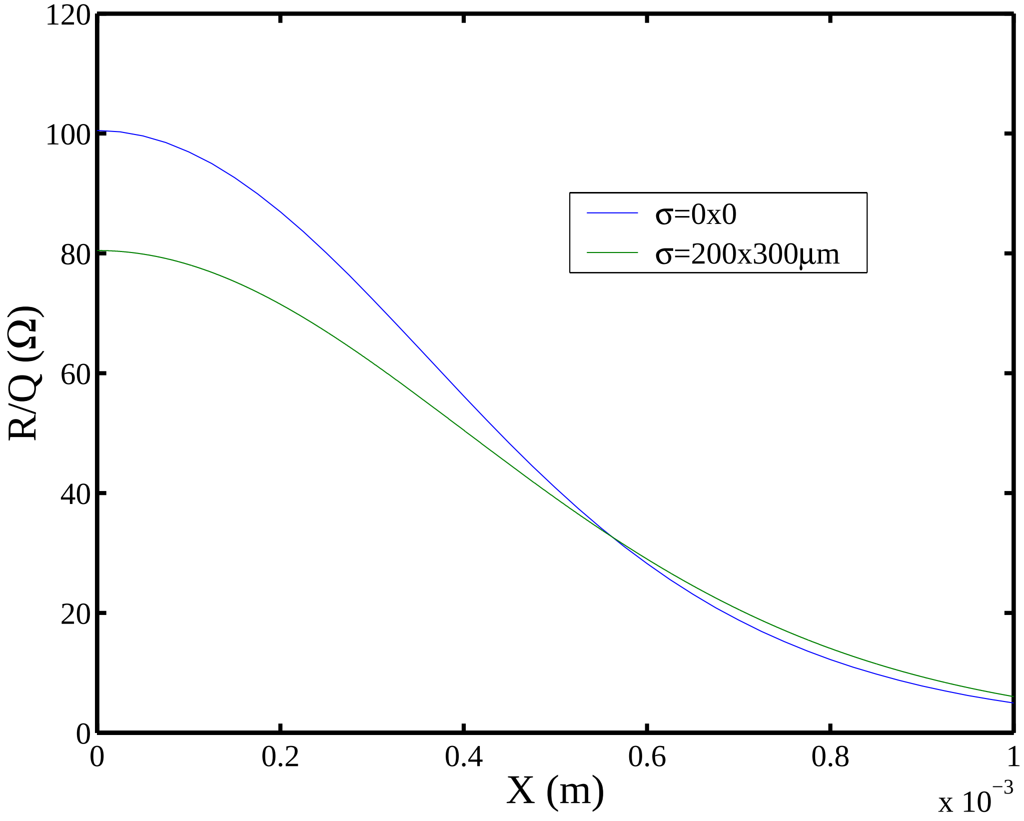

Figure 5.22: Effective $[R/Q]$ shown for a pencil beam and finite beam size.

us to study the transverse dependence of the $[R/Q]$ by using a single corrector in the upstream quad. We were able to monitor output power levels while scanning the beam position across the structure face. From this data we were able to infer $[R/Q]$ and its transverse dependence as shown in Figs. 5.23 and 5.24. A precise comparison requires the convolution of the 100×200 μm^2 beam size with the pencil beam $[R/Q]$ from *GdfidL* as seen in Fig. 5.22. The effective $[R/Q]$ was measured using the electron beam as a probe and the beam is scanned across the face of the structure. Figs. 5.23 and 5.24 show the data overlayed with the GdfidL expected result. Another measure of the effective $[R/Q]$ is shown by varying the beam size at the IP by adjusting the quad strength just upstream of the structure as shown in Fig. 5.25.

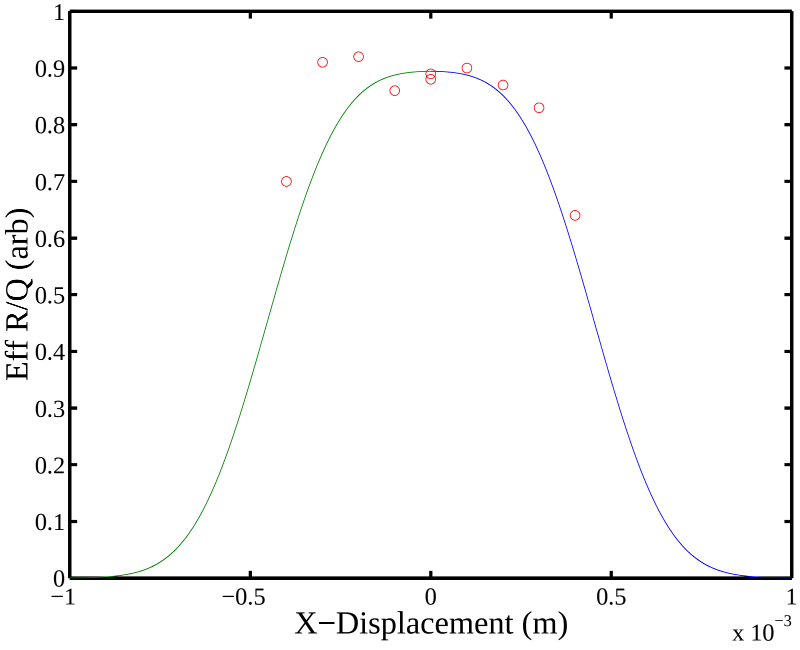

Figure 5.23: Effective $[R/Q]$ shown for a finite beam size.

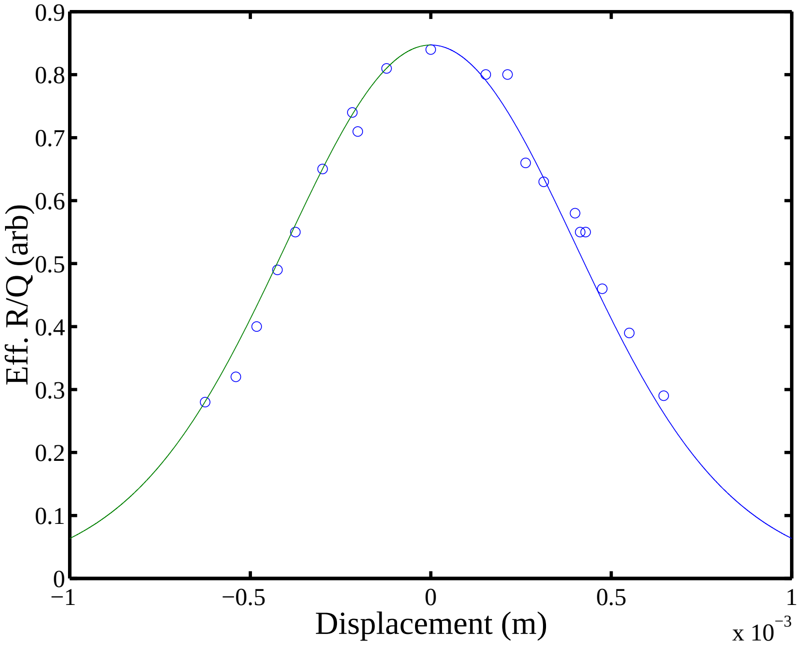

Figure 5.24: Effective $[R/Q]$ shown for a finite beam size.

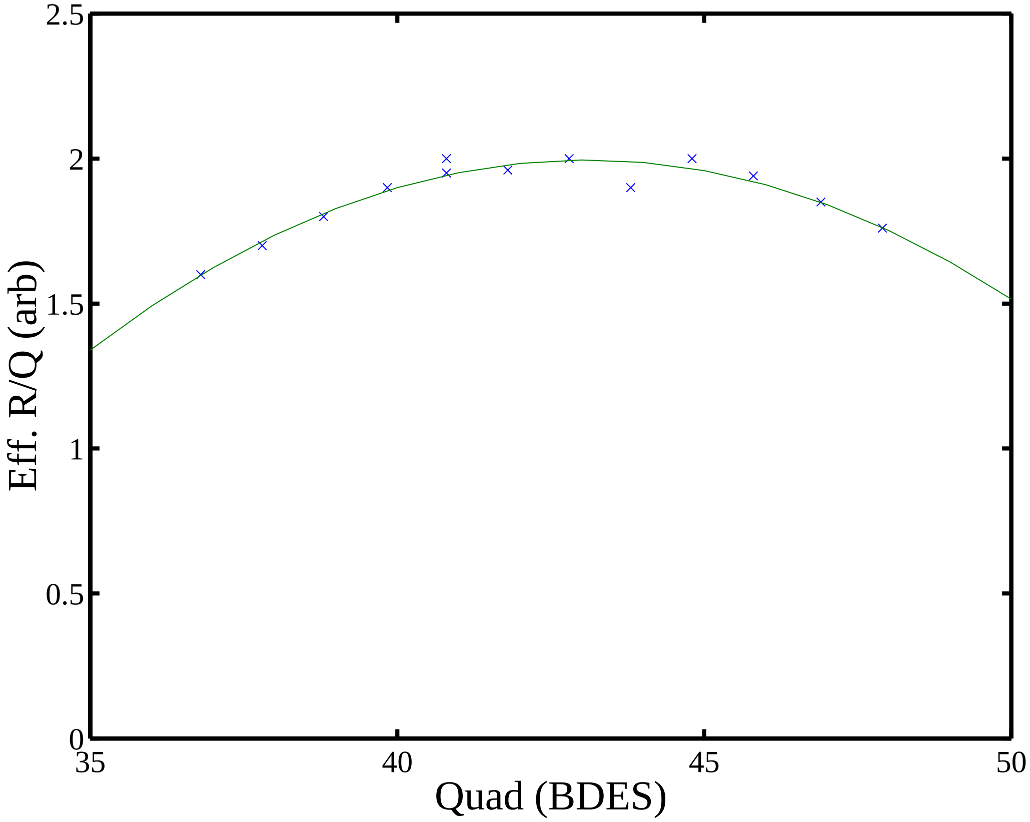

Figure 5.25: Effective $[R/Q]$ shown for a varying beam size.

Chapter 6

Conclusions

In this work we have shown, successful fabrication and test under high power of W-band accelerator structures. The W-band signals remained stable over many W-band cycles, giving no signs of breakdown or ceramic charging. The test chamber is suitable for further work in W-band or more generally, for test of many components of a size less than 4 inches. This work implies that W-band is a possible realm for a future compact collider. This frequency was chosen for a reason not too dissimilar to the reason S-band was chosen for the Two Mile Linac, namely, it is the shortest radio-frequency wavelength thought possible to build using currently available manufacturing techniques. Acceleration at laser wavelengths (0.1 - 10 μm) has been investigated, but the common problem for these very short wavelength is that the stored energy is proportionately small yielding maximal beam loading at low bunch charges.

We propose that the optimal wavelength, trading high-gradient, high-charge and repetition rate, will lie somewhere between 3.3 mm and 10 μm. This investigation of mm-wave devices has led to the novel planar dielectric design and could be scaled to possibly shorter wavelengths. A similar pursuit of Tera-Hertz resonant devices might start with the robust approach of the planar dielectric accelerator.

Bibliography

[1] C. Adolphsen *et al.*, "RF processing of X-band accelerator structures at the NLCTA," in *Proceedings of the 20th International Linac Conference (Linac 2000)*, Monterey, California, 21-25 Aug 2000, SLAC-PUB-8573, *to be published.*

[2] R. B. Palmer, Ann. Rev. Nucl. Part. Sci. **40**, 529 (1990).

[3] M. E. Hill, R. S. Callin and D. H. Whittum, "High-power vacuum window in WR10," *IEEE Trans. MTT*, to be published.

[4] M. E. Hill, R. S. Callin, M. Seidel and D. H. Whittum, "High power squeeze type phase shifter at W-band," sub. to *IEEE Trans. MTT*.

[5] M. E. Hill, W. R. Fowkes, X. E. Lin and D. H. Whittum, "Beam-cavity interaction circuit at W-band," *IEEE Trans. MTT*, to be published.

[6] M. E. Hill, R. S. Callin, X. E. Lin, and D. H. Whittum, "Planar Dielectric Accelerator Structure at W-band," sub. to *Rev. Sci. Inst.*

[7] P.J. Chou, G.B. Bowden, M.R. Copeland, A. Farvid, R.E. Kirby, A. Menegat, C. Pearson, L. Shere, R.H. Siemann, J.E. Spencer, and D.H. Whittum, *Advanced Accelerator Concepts*, AIP Conf. Proc. 398 (AIP, New York, 1997) pp. 501-517.

[8] N.M. Kroll, D. C. Vier, M.E. Hill, X.E. Lin, R.H. Siemann, D.H. Whittum, and D.T. Palmer, "Planar accelerator structures for millimeter wavelengths," *Proceedings of the 1999 Particle Accelerator Conference* (IEEE, New York, 1999) pp. 3612-3614.

[9] D. T. Palmer, M. E. Hill, S. Schwartzkopf, R. H. Siemann and R. Witherspoon, "Materials research related to W band cavity construction," *Proceedings of the 1999 Particle Accelerator Conference*, (IEEE, New York, 1999) pp. 545-547.

[10] J. B. Rosenzweig, P. Schoessow, B. Cole, W. Gai, R. Konecny, J. Norem and J. Simpson, Phys. Rev. **A39**, 1586 (1989).

[11] J. W. Wang, G. A. Loew, J. W. Simpson, E. Chojnacki, W. Gai, R. Konecny and P. Schoessow, "Wake field measurements of SLAC linac structures at the Argonne AATF," in *Procceedings of the 1991 IEEE Particle Accelerator Conf.* (IEEE, New York) pp. 3219-22.

[12] M. A. Allen *et al.*, "High Gradient Electron Accelerator Powered By A Relativistic Klystron," Phys. Rev. Lett. **63**, 2472 (1989).

[13] C. Adolphsen *et al.*, "Measurement of wakefield suppression in a damped and detuned X-band accelerator structure," Phys. Rev. Lett., **74**, (APS,1995), pp. 2475-2478

[14] S. Lidia, *et al.* , "RK-TBA at the RTA Test Facility," *Proceedings 7th Workshop on Advanced Accelerator Concepts* (AIP conference proceedings; 398) Edited by S. Chattopadhyay, J. McCullough, P. Dahl. (AIP, Woodbury, 1997) pp. 842-851.

[15] M. E. Hill, C. Adolphsen, W. Baumgartner, R. S. Callin, X. E. Lin, M. Seidel, T. Slayon and D. H. Whittum, "High-gradient millimeter wave accelerator on a planar dielectric substrate," sub. to *Phys. Rev. Lett.*

[16] W.K.H. Panofsky and W.A. Wenzel, "Transverse Deflection Of Charged Particles In Radiofrequency Fields," *Rev. Sci. Instrum.* 27 (1956) p. 967.

[17] B. Richter, "The Slac Linear Collider," SLAC-PUB-3854 *Presented at 1st Annual Mtg. of Div. of Particles and Fields of the APS, Santa Fe, N. Mex., Oct 31 - Nov 3, 1984.*

[18] A. W. Chao, B. Richter and C. Y. Yao, "Beam Emittance Growth Caused By Transverse Deflecting Fields In A Linear Accelerator," Nucl. Instrum. Meth. **178**, 1 (1980).

[19] J. T. Seeman, F. J. Decker and I. Hsu, "The Introduction of trajectory oscillations to reduce emittance growth in the SLC LINAC," SLAC-PUB-5705 *Presented at 15th International Conference on High Energy Accelerators (HEACC'92), Hamburg, Germany, 20-24 Jul 1992.*

[20] Whittum, personal communication.

[21] F. Zimmermann, D. H. Whittum, M. E. Hill, "New concepts for a compact 5-TeV Collider," *Proceedings of the 6th European Particle Accelerator Conference* (IOP, Philadephia,1998) pp. 865-7.

[22] C. Nantista and C. Adolphsen, "Beam current monitors in the NLCTA", *Proceedings of the 1997 Particle Accelerator Conference* (IEEE, New York, 1997) pp. 2256-2258

[23] C. Nantista, *et al.*, "Beam profile monitors in the NLCTA", *Proceedings of the 1997 Particle Accelerator Conference* (IEEE, New York, 1998) pp. 2186-2188, SLAC-PUB-7523.

[24] P. Zou, W. Gai, R. Konecny and T. Wong, "Construction and testing of an 11.4-GHz dielectric structure based traveling wave accelerator," *Proceedings of the 1999 Particle Accelerator Conference* (IEEE, New York, 1999) pp. 3618-3620

[25] P. Chou, "Measurement of Losses in EDMed Waveguides and in First W-band Structure," ARDB Tech. Note 99, (unpublished).

[26] Norman M. Kroll and X.E. Lin, "Computer Determinations of the Properties of Waveguide Loaded Cavities", *Proceedings of the 1990 Linear Accelerator Conference*, LA-12004-C, Carolyn Beckmann, ed. (LANL, Abuquerque, 1990) pp. 238-240.

[27] L. C. Maier, Jr and J. C. Slater, Journal of Applied Physics **23**, 68 (1952).

[28] J.C. Slater, *Microwave Electronics* (D. Van Nostrand, Boston, 1950).

[29] W. Bruns, "GdfidL: A finite difference program for arbitrarily small perturbations in rectangular geometries", *IEEE Trans. Magn.* **32**, pp. 1453-1456, 1996.

[30] X.E. Lin, "Diamond coating in accelerator structures," *Advanced Accelerator Concepts*, W. Lawson, C. Bellamy, and D.F. Brosius, eds., AIP Conf. Proc. 472 (AIP, New York, 1999) pp. 676-685.

[31] C.W. Steele, "A non-resonant perturbation theory," *IEEE Trans. Magn.* **14** (1966) pp. 70-74

[32] H. Henke, "Planar mm-Wave RF Structures," *Proceedings 7th Workshop on Advanced Accelerator Concepts* (AIP conference proceedings; 398) Edited by S. Chattopadhyay, J. McCullough, P. Dahl. (AIP, Woodbury, 1997) pp. 485-500.

[33] W. Schnell, “High Frequency Linear Colliders,” *Proceedings 4th European Particle Accelerator Conference* (EPAC 94) Edited by V. Suller and Ch. Petit-Jean-Genaz (World Scientific, River Edge, 1994) pp. 368-372

[34] R.H.Siemann, “W-band vector network analyzer based on an audio lock-in amplifier”, SLAC-PUB-7884.

[35] Code developed at CERN, contact information at: http://home.cern.ch/mad

[36] The European Physical Journal C, “Review of Particle Physics,” (1999) p. 166.